Leveraging the Photofunctions of Transition Metal Complexes for the Design of Innovative Phototherapeutics

Lee, Lawrence Cho-Cheung; Lo, Kenneth Kam-Wing

Published in:
Small Methods

Published: 20/11/2024

Document Version:
Final Published version, also known as Publisher's PDF, Publisher's Final version or Version of Record

Published version (DOI):
10.1002/smtd.202400563

Publication details:
Lee, L. C.-C., & Lo, K. K.-W. (2024). Leveraging the Photofunctions of Transition Metal Complexes for the Design of Innovative Phototherapeutics. *Small Methods*, *8*(11), Article 2400563. https://doi.org/10.1002/smtd.202400563

small methods
www.small-methods.com

Leveraging the Photofunctions of Transition Metal Complexes for the Design of Innovative Phototherapeutics

*Lawrence Cho-Cheung Lee and Kenneth Kam-Wing Lo**

Despite the advent of various medical interventions for cancer treatment, the disease continues to pose a formidable global health challenge, necessitating the development of new therapeutic approaches for more effective treatment outcomes. Photodynamic therapy (PDT), which utilizes light to activate a photosensitizer to produce cytotoxic reactive oxygen species (ROS) for eradicating cancer cells, has emerged as a promising approach for cancer treatment due to its high spatiotemporal precision and minimal invasiveness. However, the widespread clinical use of PDT faces several challenges, including the inefficient production of ROS in the hypoxic tumor microenvironment, the limited penetration depth of light in biological tissues, and the inadequate accumulation of photosensitizers at the tumor site. Over the past decade, there has been increasing interest in the utilization of photofunctional transition metal complexes as photosensitizers for PDT applications due to their intriguing photophysical and photochemical properties. This review provides an overview of the current design strategies used in the development of transition metal complexes as innovative phototherapeutics, aiming to address the limitations associated with PDT and achieve more effective treatment outcomes. The current challenges and future perspectives on the clinical translation of transition metal complexes are also discussed.

1. Introduction

Despite the advent of various cancer treatment strategies (e.g., surgery, radiotherapy, chemotherapy, and immunotherapy), cancer remains one of the leading causes of death worldwide, accounting for almost 10 million deaths in 2022.[1] In clinical settings, surgery is the primary treatment approach for most types of cancer and is often used in conjunction with radiotherapy or chemotherapy to enhance therapeutic outcomes. However, surgery can promote the dissemination of cancer cells from the primary tumor, increasing the risk of metastasis after surgical resection;[2] while radiotherapy and chemotherapy can induce resistance in cancer cells, resulting in poor prognosis or even recurrence.[3] Immunotherapy, a personalized treatment that harnesses the host immune system to recognize and eliminate cancer cells,[4] also has its challenges, such as unpredictable patient response and the potential for severe immune-related adverse effects. Thus, there is an urgent need for new therapeutic approaches for effective cancer treatment.

Photodynamic therapy (PDT) has emerged as a promising approach for treating cancer with high spatiotemporal precision and minimal invasiveness.[5] The typical PDT procedure involves the activation of a photosensitizer localized within the tumor using light to produce cytotoxic reactive oxygen species (ROS) such as singlet oxygen ($^1O_2$), superoxide anion radical ($O_2^{\bullet-}$), hydrogen peroxide (H_2O_2), and hydroxyl radical ($HO^{\bullet}$). These ROS trigger cancer cell death through induction of oxidative damage to adjacent biomolecules (e.g., DNA/RNA, proteins, and lipids) and subcellular organelles, and destruction of tumor-associated vasculature that leads to oxygen and nutrient deprivation. Since PDT offers precise control over ROS production at the tumor site, it enables the selective eradication of malignant tumors while minimizing damage to surrounding normal tissues. Furthermore, PDT can invoke protective antitumor immune response to inhibit tumor metastasis and recurrence, improving patient survival rates. Several organic-based photosensitizers, such as porfimer sodium, 5-aminolevulinic acid, and methyl 5-aminolevulinate, have been clinically approved to treat various types of cancer.[6] However, these photosensitizers, primarily based on a tetrapyrrolic scaffold such as porphyrin and chlorin, have limitations including tedious synthesis and purification, poor aqueous solubility, rapid photobleaching or photodegradation, and slow clearance from the body, resulting in photosensitivity in patients after PDT treatment. Thus, it is imperative to develop new photosensitizers for more effective PDT.

L. C.-C. Lee, K. K.-W. Lo
Department of Chemistry
City University of Hong Kong
Tat Chee Avenue, Kowloon, Hong Kong, P. R. China
E-mail: bhkenlo@cityu.edu.hk

K. K.-W. Lo
State Key Laboratory of Terahertz and Millimeter Waves
City University of Hong Kong
Tat Chee Avenue, Kowloon, Hong Kong, P. R. China

The ORCID identification number(s) for the author(s) of this article can be found under https://doi.org/10.1002/smtd.202400563

DOI: 10.1002/smtd.202400563

In recent years, photofunctional transition metal complexes have gained significant attention as photosensitizers for PDT applications.[7] Of particular interest are second- and third-row transition metal complexes such as rhenium(I), ruthenium(II), osmium(II), iridium(III), and platinum(II) complexes. These inorganic and organometallic transition metal complexes offer several advantages over conventional organic photosensitizers. The presence of a heavy metal center in these complexes enhances spin–orbit coupling (SOC) and facilitates intersystem crossing (ISC), resulting in efficient formation of triplet states with quantum yields approaching unity for ROS photosensitization. The heavy metal center also relaxes the spin selection rule, allowing radiative transition from the lowest triplet state (T_1) to the ground state (S_0) (i.e., phosphorescence) to occur. Compared to organic fluorescent probes and photosensitizers, phosphorescent transition metal complexes display longer emission lifetimes (in the timescale of sub-microsecond to microsecond), which allow the elimination of interference from shorter-lived autofluorescence using time-resolved luminescence imaging techniques such as phosphorescence lifetime imaging microscopy (PLIM).[8] Also, the larger Stokes' shifts associated with phosphorescence minimize self-quenching effects that are often observed in organic molecules at high local concentrations. These intriguing luminescence properties enable them to function as theranostic agents, opening up exciting prospects for image-guided therapy. Furthermore, transition metal complexes exhibit high photostability, ensuring efficient ROS generation at low concentrations and reducing the risk of causing systemic toxicity and photosensitivity after PDT treatment. Additionally, the high structural diversity and synthetic versatility of transition metal complexes allow for facile manipulation of their photophysical properties and biological behavior through a judicious choice of metal centers and ligands. These remarkable properties have led to the rapid development of transition metal complexes as PDT agents for cancer treatment. One ruthenium(II)-based photosensitizer, TLD1433, has entered phase II clinical trials (NCT03945162) for treating non-muscle invasive bladder cancer with PDT.[9]

While PDT holds great promise for cancer treatment, the inefficient production of ROS in the hypoxic tumor microenvironment (TME), limited penetration depth of light in biological tissues, and inadequate accumulation of photosensitizers at the tumor site have hampered its clinical applications. Given the pivotal role of photosensitizers in PDT, a strategic design of photosensitizers is imperative to overcome these challenges and improve therapeutic outcomes. In this Review, we provide an overview of the current design strategies used in the development of transition metal complexes as innovative phototherapeutics to improve PDT. Specifically, we focus on the design approaches that enable: efficient photosensitization of ROS or direct photooxidation of biomolecules (Section 2); red or near-infrared (NIR) light excitation (Section 3); selective targeting to subcellular organelles (Section 4) and cancer cells (Section 5); specific activation in cancer cells (Section 6); remodeling of the TME (Section 7); and combination therapy with other therapeutic modalities (Section 8). We also discuss the current challenges and future prospects on the clinical translation of transition metal complexes, aiming to inspire the development of more effective PDT agents for clinical applications.

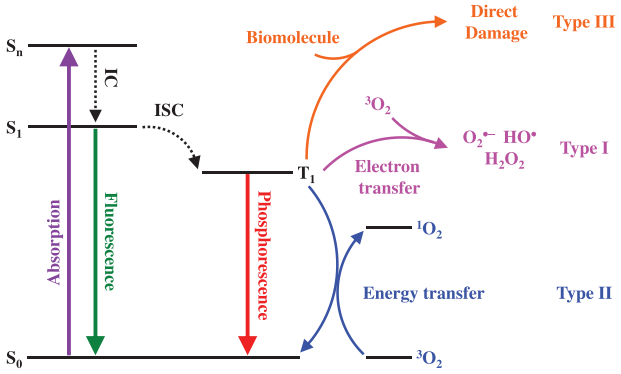

Figure 1. A simplified Jablonski diagram illustrating various important radiative and non-radiative processes and possible photochemical reaction pathways in transition metal complexes. IC, internal conversion; ISC, intersystem crossing.

2. Transition Metal Complexes for ROS Photosensitization and Biomolecule Photooxidation

In a typical PDT procedure, the photoexcitation of a photosensitizer to its triplet excited state leads to the production of ROS such as $O_2^{\bullet-}$, H_2O_2, and HO• via a Type I process that involves electron transfer to surrounding substrates, or $^1O_2$ via a Type II process that involves energy transfer to O_2 (**Figure 1**). These two types of photoreactions have long been recognized for their crucial roles in PDT. Recently, a third mechanism in PDT has been proposed, which involves the direct recognition and targeted damage to specific biomolecules without the involvement of ROS.[10] The strategic manipulation of these photochemical reaction pathways can facilitate the development of more effective PDT agents.

2.1. Type II ROS Photosensitization

Among various ROS, $^1O_2$ is considered the primary cytotoxic species responsible for the therapeutic effects of PDT due to its long lifetime and diffusion distance in cells.[11] To achieve efficient $^1O_2$ generation, it is critical for the triplet excited state of the photosensitizers to possess an appropriate energy level and a long lifetime for efficient energy transfer to O_2 to promote its $^3\Sigma_g \rightarrow {}^1\Delta_g$ transition.

One effective approach for prolonging the triplet excited state lifetimes of transition metal complexes involves the direct conjugation of an organic chromophore with a lower triplet state energy level to the metal coordination framework, which allows facile access to the long-lived triplet excited states of the organic chromophore for ROS photosensitization.[12] A representative example is TLD1433 (**1**) (**Figure 2**), a ruthenium(II) complex appended with an α-terthiophene chromophore. This complex displays very high photocytotoxicity toward cancer cells, resulting in efficient cancer cell elimination in vitro and in vivo.[13] Probing the excited state dynamics of related ruthenium(II) complexes bearing different numbers of thiophene rings reveals that the α-oligothiophene pendant is crucial in imparting a long-lived triplet intraligand charge-transfer (^{3}ILCT) state that determines the $^1O_2$ photosensitization efficiency of the complexes, and the

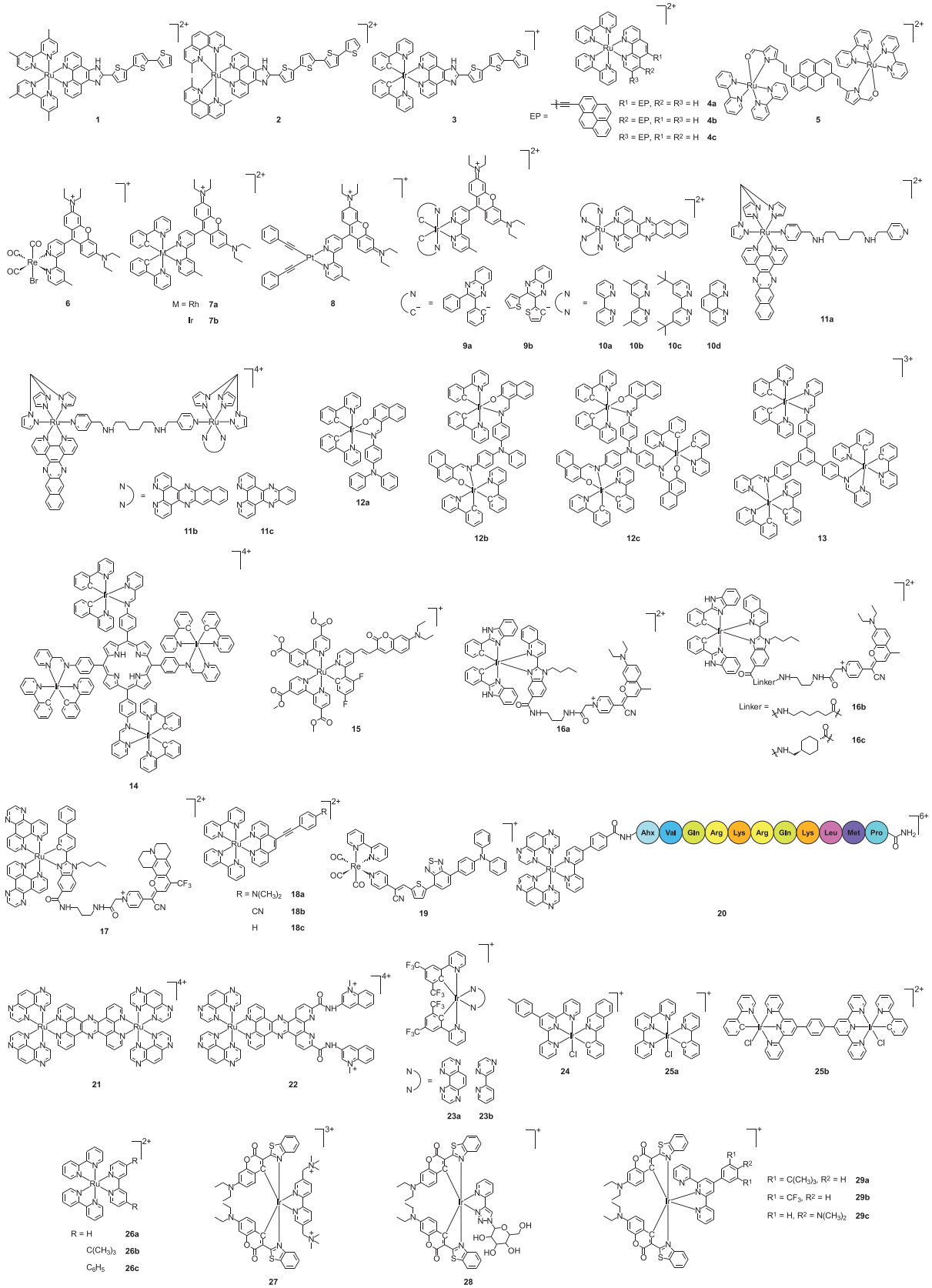

Figure 2. Structures of transition metal complexes for Type II (**1**–**14**) and Type I ROS photosensitization (**15**–**19**) and biomolecule photooxidation (**20**–**29**).

accessibility of this state increases upon increasing the length of the α-oligothiophene chain.[14] Additionally, the lifetime of the ^{3}ILCT state increases upon binding to biomolecules (e.g., DNA) due to conformational restriction, facilitating $^1O_2$ generation.[15] Structure–activity relationship analysis of related ruthenium(II) α-oligothiophene complexes carrying different ancillary ligands further highlights that the low-lying, long-lived ^{3}ILCT state localized on the α-oligothiophene chain underlies the high photocytotoxic activity of the complexes.[16] These studies have also led to the identification of a ruthenium(II) α-tetrathiophene complex (**2**) that exhibits extremely potent photocytotoxicity toward a range of cancer cell lines, particularly human skin melanoma SK-MEL-28 cells with unprecedented photocytotoxicity index (PI) values of up to 10^{12} and 10^6 under normoxia and hypoxia, respectively, making it the most potent transition metal-based photosensitizer reported to date.[16b,c] Considering that the chirality in transition metal complexes plays an important role in their biological activities such as interactions with chiral biomolecules (e.g., DNA and protein) and cellular uptake, Shi, Chen, Li, and co-workers have developed a pair of enantiopure iridium(III)-based TLD1433 analogs (Δ-**3** and Λ-**3**) and examined their enantiomer-dependent behavior.[17] Both isomers show similar photophysical properties including strong visible-light absorption, long triplet excited state lifetimes, and high $^1O_2$ generation efficiencies. Notably, while both enantiomers are equipotent toward human breast adenocarcinoma MCF-7 cells upon irradiation ($IC_{50,light}$ = 2.7 nM), the Λ-isomer displays remarkably higher photocytotoxic activity toward SK-MEL-28, human hepatocellular carcinoma (HCC) HepG2, and human normal liver LO2 cells ($IC_{50,light}$ = 3–40 nM) compared to the Δ-isomer ($IC_{50,light}$ = 9–90 nM), illustrating the influence of chirality on the biological activities of the complexes.

The outstanding performance of TLD1433 and its analogs highlights the promising potential of transition metal–organic chromophore conjugates as photosensitizers for PDT applications. Thummel, McFarland, and co-workers have designed three ruthenium(II)–pyrene dyads (**4**) as photosensitizers for PDT.[18] The introduction of an ethynylpyrene (EP) moiety to the ruthenium(II) complexes imparts an accessible, long-lived triplet intraligand (^{3}IL) state (τ_o = 22–240 μs) for promoting $^1O_2$ generation (Φ_Δ = 0.65–0.87). Thus, the complexes exhibit high photocytotoxic activity toward human leukemia HL-60 cells ($IC_{50,light}$ = 0.15–1.8 μM) upon exposure to white-light irradiation (100 J cm^{-2}) within a short photosensitizer-to-light interval (1 h). Notably, the high photocytotoxicity of the complexes is also observed in malignant human melanoma Malme-3M cells ($IC_{50,light}$ = 0.2–0.7 μM), which are characterized by low O_2 content and resistance to various types of therapy due to active melanin production. Thompson, McFarland, and co-workers have developed a series of dinuclear ruthenium(II) pyrrolide complexes, where the two ruthenium(II) centers are connected using an organic chromophore-derived linker.[19] Among the complexes studied, the triad containing a pyrenyl linker (**5**) shows extremely potent photocytotoxic activity toward HL-60 cells upon visible-light or red-light irradiation ($IC_{50,light}$ = 10 and 140 nM, respectively). Furthermore, the complex has been tested in large 3D multicellular tumor spheroids (MCTSs) characterized by a hypoxic core, which mimic the architecture and features of in vivo solid tumors. Remarkably, the complex is also highly photocytotoxic toward HL-60 MCTSs ($IC_{50,light}$ = 60 nM), highlighting the significance of accessing the long-lived pyrene-based ^{3}IL state in maintaining the photocytotoxicity under hypoxic conditions.

Gong, Wong, and co-workers have designed a series of luminescent transition metal–rhodamine dyads (**6**–**8**) as photosensitizers for PDT.[20] These bichromophoric complexes display intense characteristic rhodamine absorption and fluorescence at ca. 574 and 630 nm, respectively. Importantly, the presence of a heavy metal center facilitates the population of the long-lived rhodamine-centered ^{3}IL state via direct ISC from its singlet manifold, resulting in efficient $^1O_2$ generation. Furthermore, these cationic complexes exhibit high specificity for the mitochondria in cancer cells due to the more hyperpolarized mitochondrial membrane, leading to their preferential accumulation in cancer cells over normal cells. Upon irradiation, the complexes induce mitochondrial depolarization and dysfunction, resulting in significant cancer cell apoptosis. In vivo fluorescence imaging shows that upon intravenous injection, the complexes show efficient tumor accumulation in mice bearing MCF-7 tumor xenografts. Subsequent exposure of the tumors to irradiation leads to effective suppression of tumor growth, increasing the survival rate of the animals. Interestingly, the ROS generation efficiencies of the transition metal–rhodamine dyads can be enhanced through a ligand regulation approach.[21] Changing the cyclometalating ligand in the iridium(III)–rhodamine complex from 2-phenylpyridine (**7b**) to 2,3-diphenylquinoxaline with a lower-lying excited state (**9a**) prolongs the rhodamine triplet state lifetime (τ increases from 0.82 to 9.73 μs), resulting in enhanced $^1O_2$ generation (Φ_Δ increases from 0.24 to 0.726). Additionally, the ligand modification alters the subcellular localization of the complex from the mitochondria to the endoplasmic reticulum (ER), triggering cancer cell apoptosis through the induction of ER stress. These changes lead to more effective tumor growth inhibition in MCF-7 tumor-bearing mice. Further investigations into the correlation between the energy levels of the iridium(III)-based triplet excited states and the ROS generation efficiencies of the complexes reveal that the metal-based triplet excited states can serve as a relay between the rhodamine singlet and triplet excited states, providing an additional pathway for populating the rhodamine triplet state through a cascade energy transfer process.[22] Among the complexes studied, complex **9b** displays the highest ROS generation efficiency due to: 1) the small energy gap between the rhodamine singlet state and iridium(III)-based triplet state, allowing efficient population of the rhodamine triplet state for $^1O_2$ photosensitization (Φ_Δ = 0.718); and 2) the electron-donating thiophene substituents in the cyclometalating ligand that facilitate electron transfer to surrounding substrates, enabling the generation of free radicals such as $O_2^{\bullet-}$ and HO$^\bullet$. Remarkably, treatment of mice bearing syngeneic mammary carcinoma 4T1 tumors with the complex and light irradiation leads to substantial tumor regression, as the photogenerated ROS reprogram tumor-associated macrophages (TAMs) toward the anti-inflammatory M1 phenotype and induces immunogenic cell death (ICD) of tumor cells, enhancing the infiltration of cytotoxic and helper T cells within the TME.

McFarland and co-workers have demonstrated that ruthenium(II) complexes incorporating a π-expansive benzo[*i*]dipyrido[3,2-*a*:2′,3′-*c*]phenazine (dppn) ligand (**10**)

can be developed as photosensitizers for multiwavelength PDT.[23] The introduction of the dppn ligand facilitates the formation of a low-lying, long-lived ^{3}IL state that is crucial for $^1O_2$ photosensitization. Additionally, the dppn ligand strengthens the intercalation of the complexes into DNA, enabling the reactive triplet metal-to-ligand charge-transfer (^{3}MLCT) state to induce DNA photocleavage through direct guanine photooxidation. As a result of this dual mode of action, the complexes exhibit high photocytotoxic activity toward HL-60 cells ($IC_{50,light}$ = 0.4–1.9 μM) even when exposed to red-light irradiation (625 nm, 100 J cm^{-2}), despite their weak absorption at this wavelength ($\varepsilon_{625\ nm}$ = 92.7–401 M^{-1} cm^{-1}). Thomas and co-workers have utilized an achiral ruthenium(II) dppn complex (**11a**) as a building block to prepare dinuclear ruthenium(II) complexes (**11b** and **11c**) for PDT applications.[24] Compared to the mononuclear complex, the dinuclear complexes show more efficient cellular uptake due to their increased formal charge and lipophilicity. Owing to the efficient access to the long-lived ^{3}IL state localized on the dppn ligand, both the mono- and dinuclear dppn complexes **11a** and **11b** display efficient $^1O_2$ generation (Φ_Δ = 0.593 and 0.672, respectively), resulting in high photocytotoxicity toward human ovarian carcinoma A2780 and its cisplatin-resistant counterpart A2780cis cells ($IC_{50,light}$ ≤ 2 and <0.1 μM, respectively) at a low light dose (14 J cm^{-2}). In contrast, the heteroleptic dinuclear complex **11c**, comprising both dppn and dppz (dppz = dipyrido[3,2-*a*:2′,3′-*c*]phenazine) ligands, exhibits lower efficiency in $^1O_2$ generation (Φ_Δ = 0.157) and thereby lower photocytotoxic activity ($IC_{50,light}$ = 20 and 7 μM, respectively). Nevertheless, the characteristic ^{3}MLCT emission of the complex allows for the monitoring of its cellular uptake with fluorescence microscopy, which reveals its primary localization in the lysosomes and partial accumulation in the mitochondria, highlighting its promising potential as a theranostic agent.

Another approach to the development of efficient ROS photosensitizers involves the construction of multinuclear transition metal complexes, where the incorporation of additional metal centers into the same molecule can enhance SOC and promote ISC, facilitating the generation of triplet excited states for ROS photosensitization.[25] Zhu, Xie, Tang, Su, Bryce, and co-workers have developed three red-emitting iridium(III) complexes with a different number of metal centers (**12**) as photosensitizers for PDT.[26] Owing to the high flexibility of the Schiff base ligand and the triphenylamine bridge, these complexes are aggregation-induced emission (AIE)-active, showing increased emission intensities and lifetimes upon aggregation in aqueous solutions. Compared to the mononuclear complex **12a**, the dinuclear and trinuclear complexes **12b** and **12c** display stronger visible-light absorption and higher $^1O_2$ generation efficiencies due to the increased number of iridium(III) centers. To improve their aqueous solubility and biocompatibility while retaining their high luminescence and ROS generation efficiencies in the aggregated state, the complexes have been formulated into nanoparticles through encapsulation into polymeric micelles derived from a poly(ethylene glycol) (PEG)-modified 1,2-distearoyl-*sn*-glycero-3-phosphoethanolamine derivative (DSPE-PEG), followed by modification with the cell-penetrating peptide (CPP) HIV-1 Tat (RKKRRQRRRC). The resultant nanoparticles (**PM-Tat@12**) exhibit enhanced $^1O_2$ generation and increased cellular uptake compared to their monomeric counterparts, leading to more significant photoinduced cell death. Remarkably, the nanoparticles **PM-Tat@12c** rapidly accumulate in the tumor region in mice bearing syngeneic HCC H22 tumors after tail vein injection and induce tumor cell necrosis upon irradiation, resulting in a significant reduction in the tumor volume. Related AIE-active multinuclear iridium(III) complexes **13**[27] and **14**[28] incorporating 1,3,5-triphenylbenzene and tetraphenylporphyrin as a bridging unit, respectively, have also been developed using simple Schiff base reactions. These complexes can self-assemble into nanoparticles featuring strong visible-light absorption, intense NIR emission, high $^1O_2$ generation efficiencies, facile cellular uptake, low dark cytotoxicity, and excellent photocytotoxicity, facilitating their applications in imaging and PDT.

2.2. Type I ROS Photosensitization

Hypoxia is a common feature of solid tumors, which arises due to an imbalance between the rapid O_2 consumption during cancer cell proliferation and inadequate O_2 supply caused by abnormal tumor blood vessels.[29] The hypoxic TME poses a significant challenge for O_2-dependent Type II PDT in the treatment of solid tumors since the generation of $^1O_2$ relies on sufficient O_2 concentration. Additionally, the substantial O_2 consumption during Type II photoreaction can aggravate tumor hypoxia, further hampering the effectiveness of PDT. In contrast, $O_2^{\bullet-}$ generated in Type I photoreaction can undergo a superoxide dismutase (SOD)-mediated disproportionation reaction, leading to the production of H_2O_2 and O_2.[30] The biocatalytic recycling of O_2 enables sustained ROS production even in O_2-depleted environments. Furthermore, $O_2^{\bullet-}$ can react with H_2O_2 through the Fenton and Haber–Weiss reaction, resulting in the generation of the highly cytotoxic HO$^\bullet$. The lower reliance on O_2 in Type I PDT renders it a promising approach for overcoming hypoxia-induced therapeutic resistance.

Zhao, Li, Huang, and co-workers have developed a cyclometalated ruthenium(II) complex conjugated with an electron-rich coumarin moiety (**15**) as a Type I photosensitizer for PDT under hypoxia.[31] The incorporation of a coumarin unit into the cyclometalating ligand not only enhances the absorption of the complex in the visible region of 450–550 nm, but also lowers the oxidation potential of the complex, facilitating photoinduced electron transfer (PET) to surrounding substrates for producing ROS through a Type I process. In particular, the complex generates a substantial amount of HO$^\bullet$ upon photoexcitation, accounting for its high photocytotoxic activity toward human cervical adenocarcinoma HeLa cells under hypoxia. Mechanistic studies reveal that the complex efficiently induces mitochondrial depolarization and triggers apoptosis in hypoxic HeLa cells upon irradiation. Importantly, in vivo experiments show that the complex effectively inhibits tumor growth in mice bearing HeLa tumor xenografts upon irradiation.

Ruiz, Brabec, Marchán, and co-workers have designed a luminescent iridium(III) complex conjugated with a far-red-emitting coumarin-pyridine (COUPY) fluorophore (**16a**) as a theranostic agent.[32] The covalent conjugation of these two luminophores enables efficient population of the long-lived COUPY triplet excited state through either triplet–triplet energy transfer from the iridium(III) core to the COUPY moiety or ISC between

the COUPY singlet and triplet excited states upon selective excitation of the iridium(III) (λ_{ex} = 355 nm) or COUPY unit (λ_{ex} = 532 nm), respectively. Remarkably, the conjugate shows distinct ROS generation capabilities depending on its microenvironment: in non-aqueous environments, it displays efficient generation of $^1O_2$, while in aqueous environments, PET between the iridium(III) and COUPY moieties leads to the formation of a long-lived charge-separated state that promotes the production of $O_2^{\bullet-}$. Additionally, the conjugation of the iridium(III) complex with the COUPY fluorophore enhances its cellular uptake while reducing its dark cytotoxicity. The selective generation of $O_2^{\bullet-}$ over $^1O_2$ in HeLa cells upon visible-light irradiation results in high photocytotoxicity under both normoxia and hypoxia ($IC_{50,light}$ = 1.32–2.51 and 1.43–2.77 μM, respectively). The high phototherapeutic potential of the conjugate has been further demonstrated in DU145 cells, a hormone-refractory and aggressive prostate cancer cell line resistant to conventional antineoplastic drugs.[33] The conjugate effectively penetrates the inner layers of tumorspheres derived from DU145 cells and efficiently eliminates both differentiated prostate cancer cells and prostate cancer stem cells upon irradiation through the induction of apoptosis and autophagy. Structure–activity relationship analysis of related iridium(III)–COUPY conjugates has led to the identification of conjugates **16b** and **16c** exhibiting enhanced photocytotoxic activity relative to conjugate **16a** under hypoxia.[34] The efficient ROS photogeneration in cells under low O_2 concentrations results in irreversible oxidative damage and triggers necrotic cell death, effectively inhibiting the growth of MCTSs. A related ruthenium(II)–COUPY conjugate (**17**) that enables the induction of ROS-mediated cancer cell death under hypoxia upon NIR-light irradiation (740 nm) has also been developed, offering the opportunities to overcome the limitations of hypoxia and light penetration in oncological PDT.[35]

Chen, He, Guo, and co-workers have developed three ruthenium(II) complexes (**18**) as Type I photosensitizers for overcoming hypoxia in PDT.[36] Among them, complex **18a** shows the highest efficiency in generating $O_2^{\bullet-}$, which can be attributed to the presence of an electron-donating *N*,*N*-dimethylamino group that facilitates PET. Additionally, complex **18a** displays more efficient cellular uptake in MCF-7 cells due to its higher lipophilicity. As a result, complex **18a** exhibits very high photocytotoxicity under both normoxic and hypoxic conditions ($IC_{50,light}$ = 0.4 and 1.5 μM, respectively). Mechanistic studies on cell death show that the photogenerated ROS cause rapid glutathione (GSH) consumption, which inhibits the expression of glutathione peroxidase 4 (GPX4) and triggers the accumulation of lipid peroxide (LPO), inducing ferroptotic cell death. Furthermore, treatment of MCF-7 MCTSs with a diameter of ca. 500 μm with the complexes and light irradiation leads to efficient inhibition of MCTSs growth, highlighting that the complexes can overcome tumor hypoxia and inhibit the growth of solid tumors.

Wang, Zhang, Huang, and co-workers have designed a rhenium(I) complex featuring an electron donor–acceptor (D–A) structure (**19**) as a dual Type I and Type II PDT agent.[37] The D–A structure of the complex facilitates PET to H_2O and O_2 upon irradiation, leading to the formation of HO$^\bullet$ and $O_2^{\bullet-}$, respectively. Additionally, the complex shows efficient $^1O_2$ generation (Φ_Δ = 0.86). The efficient production of ROS via both Type I and Type II pathways results in high photocytotoxic activity toward murine melanoma B16 cells under both normoxia and hypoxia ($IC_{50,light}$ = 6.37 and 15.52 μM, respectively). The photogenerated ROS lead to 1,4-dihydronicotinamide adenine dinucleotide (NADH) and GSH depletion as well as GPX4 inhibition, inducing ferroptosis and ICD. The induction of ICD promotes the maturation of dendritic cells (DCs), upregulation of immune-related cytokines, and infiltration of T cells. Notably, the release of interferon (IFN)-γ by cytotoxic T cells downregulates the expression of GPX4, further promoting the occurrence of ferroptosis and reinforcing the therapeutic efficacy. As a result, the complex induces effective tumor growth inhibition in B16 tumor-bearing mice upon irradiation, increasing the survival rate of the mice.

2.3. Direct Biomolecule Photooxidation

While the generation of ROS via a Type I process can reduce its reliance on endogenous O_2 in tumors through partial O_2 circulation based on SOD-mediated disproportionation reactions or Fenton/Haber–Weiss reactions, O_2 remains a critical component for the photosensitization process. The emerging paradigm of a third mechanism, which involves the direct recognition and damage of intracellular biomolecules in an ROS-independent manner, offers a solution to circumvent the challenges posed by O_2 concentration in PDT.[10] In this context, transition metal complexes that enable the direct photooxidation of crucial biomolecules such as DNA/RNA, proteins, and redox-active species hold substantial therapeutic significance.

2.3.1. DNA Photocleavage

Ruthenium(II) complexes bearing electron-deficient polyazaaromatic ligands such as 1,4,5,8-tetraazaphenanthrene (TAP) are known to possess a reactive ^{3}MLCT excited state capable of photooxidizing the guanine moieties of DNA to generate guanine radical cations via a PET process, leading to the photocleavage of DNA or formation of photoadducts.[38] These complexes are also photoreactive toward tryptophan-containing peptides and proteins.[39] Notably, the photoreactions of ruthenium(II) polyazaaromatic complexes with biomolecules can occur under O_2-free conditions, paving new ways for the exploration and development of novel phototherapeutic strategies.

Keyes and co-workers have conjugated a ruthenium(II) TAP complex with a peptide sequence VQRKRQKLMP that functions as a nucleus localization signal (NLS) for directing the photoinduced damage to nuclear DNA.[40] Similar to other TAP complexes, the resultant peptide conjugate (**20**) can induce direct DNA photooxidation in a $^1O_2$-independent manner. Thus, the conjugate can interact with and cause photodamage to DNA upon irradiation, resulting in an increase in its cytotoxicity. Haycock, MacNeil, Thomas, and co-workers have developed a dinuclear ruthenium(II) TAP complex (**21**) that targets both duplex and quadruplex DNA as a phototherapeutic agent against malignant melanoma.[41] This complex binds to duplex and G-quadruplex DNA with high affinity (K_b = 2 and 0.51 × 10^6 M^{-1}, respectively) and photooxidizes the guanine moieties in these structures upon irradiation without the involvement of ROS. Laser-scanning confocal microscopy (LSCM) reveals that the

complex displays efficient uptake in recalcitrant human skin cancer C8161 cells and localizes in both the nucleus and mitochondria. The complex also exhibits efficient tissue penetration in C8161 MCTSs including the hypoxic region. Thus, upon two-photon excitation, the complex induces acute and rapid photoinduced cell death in both C8161 cells and MCTSs. Keyes and co-workers have designed a ruthenium(II) TAP complex integrated with a G-quadruplex DNA-binding motif Phen-DC3 (**22**) as a phototherapeutic agent that targets G-quadruplexes located in the mitochondrial genome.[42] This complex shows higher affinity toward G-quadruplex DNA over duplex DNA due to the Phen-DC3 motif, with a higher preference for those found in the mitochondria (KSS, PMPS, and HRCC) than in the nucleus (22AG). Upon cellular internalization, the complex preferentially accumulates in the mitochondria of HeLa cells and binds to the mitochondrial DNA (mtDNA) G-quadruplex. Thus, irradiation of the treated cells induces depletion of mtDNA, loss of mitochondrial membrane potential (MMP), and apoptosis, resulting in high photocytotoxic activity under both normoxic and hypoxic conditions ($IC_{50,light}$ = 1.24 and 16 μM, respectively). However, the complex displays limited photocytotoxicity toward 3D HeLa MCTSs due to its poor penetration into the spheroid core, suggesting that new approaches are needed to enhance the tissue penetration of the complex.

Feron, Elias, and co-workers have examined the photocytotoxic activity of an iridium(III) TAP complex (**23a**) and its 2-(pyridin-2-yl)pyrazine (pzpy) counterpart (**23b**) in 3D MCTSs.[43] Both complexes are efficiently taken up by human squamous cell carcinoma FaDu cells and specifically enriched in the mitochondria. However, complex **23a** exhibits higher photocytotoxicity ($IC_{50,light}$ = 12.8 μM) under hypoxia compared to complex **23b** ($IC_{50,light}$ = 18.1 μM), making it more effective in inhibiting the growth of FaDu MCTSs. The difference in the photocytotoxic activity between the two complexes is attributed to their distinct excited state reactivities. The TAP complex **23a** shows very weak $^1O_2$ photosensitization (Φ_Δ = 0.08) but can photooxidize surrounding biomolecules (e.g., DNA) under O_2-free conditions, enabling the complete destruction of MCTSs upon irradiation. In contrast, while the pzpy complex **23b** is an efficient photosensitizer for $^1O_2$ (Φ_Δ = 0.68), its strong O_2 dependence confines its photocytotoxicity to the cancer cells located on the surface of MCTSs. Nevertheless, the effectiveness of complex **23b** in inhibiting the growth of MCTSs can be enhanced through fractional PDT, which provides sufficient time for intracellular O_2 replenishment.

2.3.2. NAD(P)H Photooxidation

Photoactive transition metal complexes play an important role in visible-light-driven photoredox catalysis for a wide range of organic transformations.[44] These complexes have been utilized to develop photocatalytic proximity labeling platforms for precise mapping of protein local microenvironments in live cells, which has enabled the elucidation of protein–protein interactions,[45] quantification of tumor-specific immune interactions,[46] and identification of small-molecule drug binding sites[47] within the complex biological milieu. Notably, targeted photoredox catalysis in cancer cells has recently emerged as a novel therapeutic approach to combat tumor hypoxia in cancer phototherapy.[48] A primary target of this approach is NADH, a crucial molecule that acts as an electron source in the mitochondrial electron transport chain and functions as a coenzyme in various biochemical reactions.[49] The induction of NADH/NAD^+ imbalance can lead to cancer cell death by disrupting cellular redox homeostasis and metabolic regulation.

Gasser, Chao, Sadler, and co-workers have developed an iridium(III)-based photocatalyst (**24**) for photocatalytic NADH oxidation in cancer cells.[48] This complex possesses a long excited state lifetime (τ_o = 1.3903 μs) and a high excited state reduction potential ($E_{1/2}Ir^{III*/II}$ = + 1.22 V vs SCE), which enable efficient oxidation of NADH to $NAD^\bullet$ in biological media with a turnover frequency (TOF) of up to 100.4 h^{-1}. After cellular uptake, the complex specifically localizes in the mitochonidra of human lung adenocarcinoma A549 cells and displays a long emission lifetime (**Figure 3a,b**). Upon continuous irradiation, intracellular NADH is oxidized to $NAD^\bullet$, which is converted to NAD^+ via electron transfer to $O_2^{\bullet-}$ or cytochrome *c* under normoxia and hypoxia, respectively, disrupting the electron transport chain through causing NADH depletion, adenosine triphosphate (ATP) reduction, and H_2O_2 production (Figure 3c–g). Thus, the complex exhibits similarly high photocytotoxic activity toward cancer cells under both normoxic and hypoxic conditions ($IC_{50,light}$ = 1.0–1.9 and 2.3–8.7 μM, respectively), demonstrating that photoredox catalysis in cells offers an alternative mechanism of action for combating tumor hypoxia. Based on this interesting scaffold, Banerjee, Huang, and co-workers have developed two iridium(III) complexes (**25**) for photocatalytic cancer therapy.[50] Owing to the presence of a second metal center, the dinuclear complex **25b** shows stronger visible-light absorption ($\varepsilon_{525\ nm}$ = 6129 $M^{-1}\ cm^{-1}$), a longer triplet excited state lifetime (τ_o = 2.48 μs), and a higher excited state reduction potential ($E_{1/2}Ir^{III*/II}$ = + 1.42 V vs SCE) than its mononuclear counterpart **25a**, enabling more efficient oxidation of NAD(P)H (TOF = up to 448.6 h^{-1}) and amino acids upon irradiation at 525 nm. Furthermore, quantification of the metal content in individual cancer cells using single-cell inductively coupled plasma-mass spectrometry (SC-ICP-MS) indicates that the dicationic complex **25b** displays more efficient cellular uptake and retention than its mononuclear counterpart. Thus, complex **25b** induces more efficient ROS generation and NAD(P)H oxidation in cancer cells upon irradiation. The disruption of cellular redox homeostasis leads to efficient apoptosis and necrosis and thus significant inhibition of tumor growth in vivo. Ruthenium(II) complexes such as $[Ru(bpy)_3]^{2+}$ (**26a**) (bpy = 2,2′-bipyridine) and its derivatives (**26b** and **26c**) can also function as both a photosensitizer and a photooxidant to induce cancer cell death.[51] Among these complexes, complex **26c** exhibits the most efficient ROS photosensitization and NAD(P)H photooxidation as well as the highest cellular uptake and retention, resulting in very high photocytotoxicity toward cancer cells ($IC_{50,light}$ = 0.05–0.3 μM) including cisplatin-resistant A549/DDP cells ($IC_{50,light}$ = 0.1 μM) and effective inhibition of tumor growth in tumor-bearing mice upon irradiation.

To enable more efficient visible-light harvesting, Huang and co-workers have designed an iridium(III) complex featuring two coumarin 6 ligands (**27**) for photoredox catalysis in cells.[52] The incorporation of coumarin 6 as ligands enhances the visible-light absorption of the complex between 400–550 nm, while the

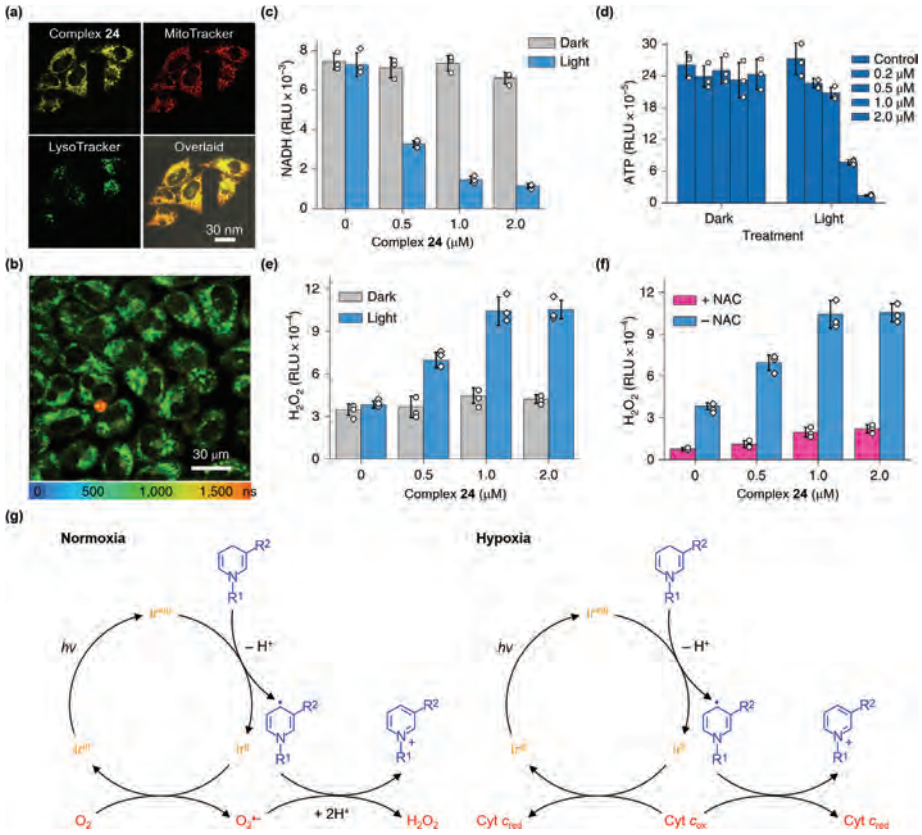

Figure 3. a) LSCM images of live A549 cells incubated with complex **24** (5 μM, 1 h) and costained with MitoTracker Red and LysoTracker Green. Complex **24**: λ_{ex} = 405 nm, λ_{em} = 562 nm; MitoTracker Red: λ_{ex} = 633 nm, λ_{em} = 660 nm; LysoTracker Green: λ_{ex} = 488 nm, λ_{em} = 520 nm. Scale bar = 30 μm. b) PLIM image of live A549 cells incubated with complex **24** (5 μM, 1 h). λ_{ex} = 760 nm, λ_{em} = 562 nm. Scale bar = 30 μm. c) NADH, d) ATP, and e) H_2O_2 concentration in A549 cells treated with various doses of complex **24** (2 h) in the dark or upon irradiation (465 nm, 8.9 J cm^{-2}). f) H_2O_2 concentration in A549 cells treated with various doses of complex **24** (2 h) and irradiated (465 nm, 8.9 J cm^{-2}) in the presence or absence of *N*-acetyl-L-cysteine (NAC; 5 mM, 2 h). RLU = relative luminescence unit. *$p < 0.05$, **$p < 0.01$, and ***$p < 0.001$. (g) The proposed catalytic cycle for NADH photooxidation under normoxia and hypoxia. Adapted with permission.[48] Copyright 2019, Springer Nature.

introduction of quaternary ammonium groups increases the water solubility of the complex. In contrast to the aforementioned iridium(III) complexes that act as photooxidants, this complex functions as a strong reductant at the excited state, reducing O_2 to $O_2^{\bullet-}$ and H_2O_2. The transient iridium(IV) species formed during the reduction of O_2 can oxidize NAD(P)H (TOF = up to 308.0 h^{-1}) and amino acids, causing intracellular redox imbalance and MMP alternation to induce cell death. Thus, the complex shows very high photocytotoxic activity ($IC_{50,light}$ = 0.37–5.4 μM) toward a range of cancer cell lines, including cisplatin-resistant A549/DDP and Sorafenib-resistant HepG2-SR cells, enabling the effective inhibition of tumor growth in vivo. A related iridium(III) complex (**28**) featuring a D-glucose pendent to enhance the aqueous solubility has also been developed.[53] Banerjee, Huang, and co-workers have also developed coumarin-functionalized iridium(III) terpyridine complexes (**29**) for cancer phototherapy.[54] The strong visible-light absorption of the complexes enables efficient $^1O_2$ photosensitization and NAD(P)H photooxidation (TOF = up to 1357.2 h^{-1}) upon irradiation at 456 or 525 nm. Thus, the complexes display very high photocytotoxicity toward human epidermoid carcinoma A431 cells upon irradiation with blue (465 nm, 11.7 J cm^{-2}; $IC_{50,light}$ = 3–20 nM) or green light (525 nm, 29.56 J cm^{-2}; $IC_{50,light}$ = 10–100 nM), leading to a substantial reduction in the tumor volume in mice bearing A431 tumor xenografts.

2.4. Discussion

Among various ROS, $^1O_2$ is considered as the primary cytotoxic species responsible for cell death in PDT. Thus, most of the transition metal-based PDT agents developed to date are efficient $^1O_2$ photosensitizers. However, the effectiveness of Type II PDT is often limited under hypoxic conditions. Several strategies have been utilized to enhance the effectiveness of Type II PDT; for example, using O_2 nanocarriers (e.g., hemoglobin, perfluorocarbons, and micro/nanobubbles) to deliver exogenous O_2 to the tumor tissue, or using (photo)catalysts for catalyzing H_2O_2 decomposition (e.g., manganese dioxide-based nanomaterials and catalase-mimicking nanozymes) or water splitting (e.g., carbon nitride and titanium oxide nanocomposites) to generate O_2 in situ to alleviate hypoxia.[55] Another approach is to shift the paradigm of PDT from an O_2-dependent Type II mechanism toward a less O_2-dependent Type I photoreaction and

O_2-independent photoredox catalysis. While there has been a significant increase in the development of organic-based Type I photosensitizers,[56] the progress in transition metal complexes has lagged due to the lack of a universal design rule guiding their development. The introduction of electron donors/acceptors to transition metal complexes has emerged as an effective means to promote electron transfer to adjacent substrates for ROS production. However, this approach necessitates in-depth investigations to optimize the design of such complexes. Notably, transition metal complexes have demonstrated significant potential in photocatalyic oxidation of vital biomolecules such as DNA and NAD(P)H in cells. Recent studies have revealed that common photosensitizers such as Rose Bengal, BODIPY, phenoselenazinium, phthalocyanine, and porphyrin derivatives can catalyze the conversion of NADH to NAD^+,[57] indicating the potential of photoredox catalysis in cells as a general mechanism underlying PDT. The advancement of photoredox catalysis in cells relies on the optimization of three main parameters of the photocatalysts, namely light absorption, excited state redox potentials, and excited state lifetimes.[58] The development of transition metal complexes with higher excited state redox potentials can expand the scope of biological substrates that can be targeted, while their strong light absorption and long excited state lifetimes can facilitate these light-driven chemical transformations to occur within the cellular environment.

3. Transition Metal Complexes for Red/NIR Light-Mediated PDT

The selection of light with an appropriate wavelength is crucial in PDT as the photosensitizer should be activated at a wavelength whose tissue penetration matches the desired depth of the treatment. In clinical settings, visible light such as blue and green light is often utilized for treating superficial cancers, while red to NIR light offers advantages for the treatment of deep-seated or large solid tumors with PDT due to its enhanced tissue penetration.

3.1. One-Photon-Induced PDT

The spectral range spanning from ca. 650 to 900 nm has been recognized as the optical window for PDT, where the absorption of light by water and endogenous chromophores in biological tissues is minimal. However, transition metal complexes typically display relatively weak absorption in this region, posing a significant challenge for their clinical use in PDT, particularly when treating deep-seated or large solid tumors.

Spingler, Ciofini, Gasser, and co-workers have utilized density functional theory (DFT) calculations to guide the design of efficient transition metal complexes exhibiting strong absorption in the phototherapeutic window.[59] This combined theoretical and experimental approach has unveiled a ruthenium(II) complex (**30**) (**Figure 4**) with absorption tailing to ca. 595 nm. Additionally, the complex shows efficient $^1O_2$ photosensitization (Φ_Δ = 0.61) while retaining high photostability upon irradiation. These remarkable properties enable the complex to display high photocytotoxic activity toward a range of cancer and normal cell lines in both 2D monolayer cell and 3D multicellular spheroid models upon irradiation at 595 nm. Studies on the mechanism of action indicate that upon photoexcitation, the complex disturbs mitochondrial respiration and inhibits glycolysis, perturbing cellular metabolism. Nevertheless, the high dark cytotoxicity of the complex ($IC_{50,dark}$ = 3.09–28.77 μM) poses a challenge to its applications as a PDT agent in vivo. To circumvent this problem, complex **30** has been encapsulated into micelles derived from DSPE-PEG-folate.[60] Compared to the free complex that exhibits high cytotoxic activity toward both cancer (A2780; $IC_{50,dark}$ = 8.39 μM) and normal cells (human embryonic lung fibroblast MRC-5; $IC_{50,dark}$ = 4.17 μM) in the dark, the resultant nanoparticles (**PM-FA@30**) are essentially non-cytotoxic ($IC_{50,dark}$ > 100 μM), indicating that the nanoparticle formulation substantially reduces the dark cytotoxicity of the complex. Furthermore, owing to the folic acid moieties present on the surface, the nanoparticles show a higher level of cellular accumulation in A2780 cells and its cisplatin-resistant (A2780cis) and doxorubicin-resistant derivatives (A2780ADR) that overexpress folate receptors (FRs). As a result, the nanoparticles display selective photocytotoxicity toward these cancer cell lines ($IC_{50,light}$ = 3.51–3.92 μM) over non-cancerous MRC-5 cells ($IC_{50,light}$ = 63.83 μM) upon irradiation (595 nm, 11.3 J cm^{-2}). Related osmium(II) complexes (**31**) have also been developed for NIR light-mediated PDT.[61] Compared to the ruthenium(II) analogs, the osmium(II) complexes exhibit stronger MLCT absorption at 650–750 nm due to the higher-lying dπ orbital of the osmium(II) center, enabling photoexcitation with NIR light of up to 740 nm. This remarkable feature allows complex **31a** to induce significant tumor eradication in mice bearing syngeneic colorectal carcinoma CT26 tumors upon exposure to a single dose of NIR light at a short photosensitizer-to-light interval (1 h).

However, the development of efficient photosensitizers displaying both strong NIR absorption and high ROS generation efficiencies is a challenging task due to the large vibronic coupling between the T_1 and S_0 states, which reduces the triplet excited state lifetimes and thus the ROS photosensitization efficiencies of the photosensitizers. Xu, Xia, Gou, and co-workers have designed two iridium(III) complexes (**32**) as efficient NIR light-excitable photosensitizers using a self-assembly-induced vibronic decoupling approach.[62] These complexes feature a rigid and planar diquinoxalino[2,3-*a*:2′,3′-*c*]phenazine ligand, which can: 1) lower the π^* orbital due to extended π-conjugation, shifting the MLCT absorption bands of the complexes to longer wavelengths; and 2) facilitate the self-assembly of the complexes into larger aggregates, reducing exciton–vibration coupling and prolonging the triplet excited state lifetimes of the complexes via inhibiting vibrational relaxations. As a result, complexes **32a** and **32b** exhibit strong absorption in the deep-red and NIR region (λ_{abs} = ca. 649 and 762 nm), and show high $^1O_2$ generation efficiencies in their aggregated state (Φ_Δ = 0.722 and 0.549) upon photoexcitation at 635 and 808 nm, respectively. These complexes have been encapsulated into Pluronic F-127 (PF127) to improve their bioavailability and biocompatibility. The resultant nanoparticles (**PM@32a** and **PM@32b**) display efficient tumor accumulation after tail vein injection and induce significant tumor regression (up to 92.9% reduction in tumor volume) upon irradiation with a 635- or 808-nm laser. A related dinuclear iridium(III) complex (**33**) has also been developed as an NIR light-excitable

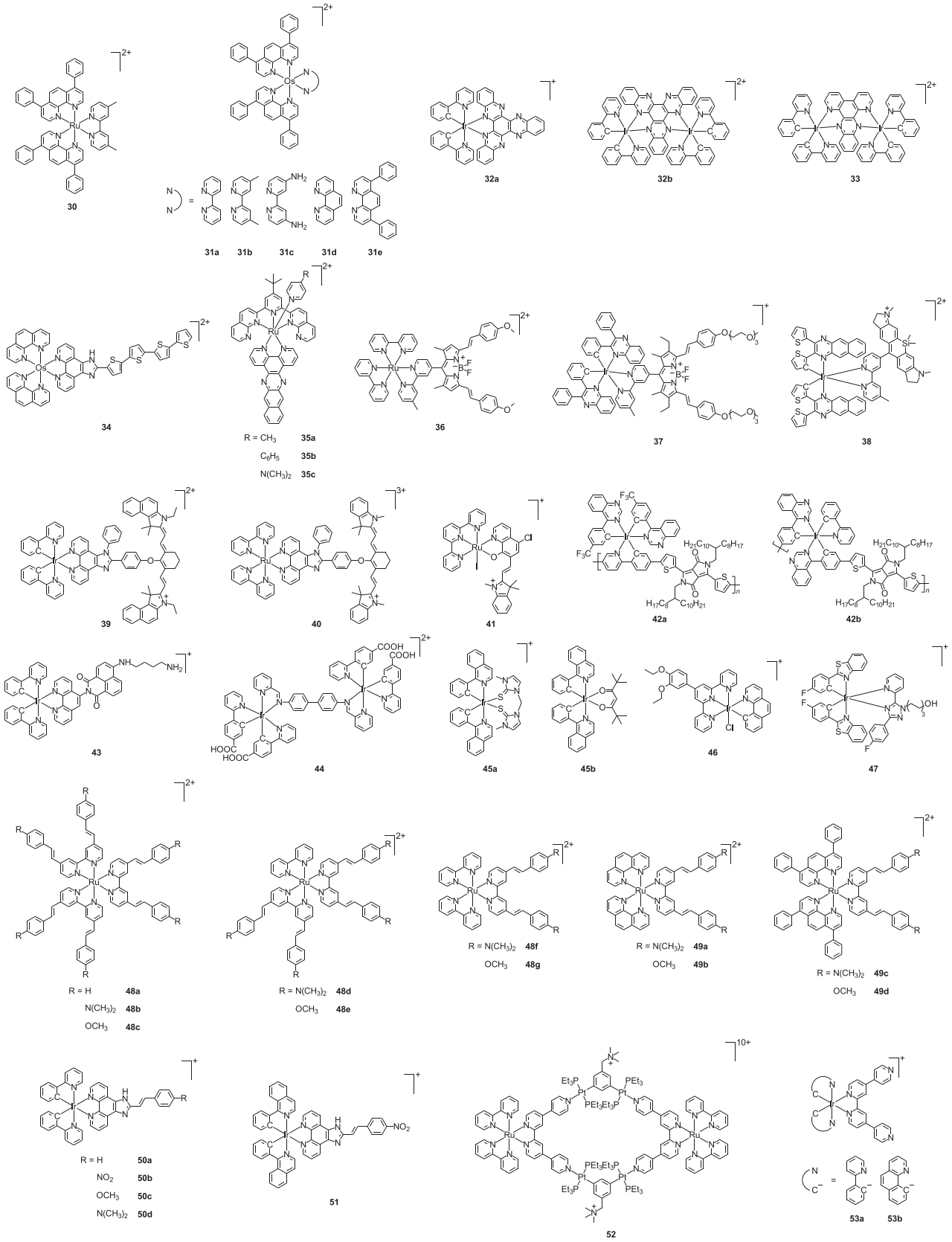

Figure 4. Structures of transition metal complexes for one-photon (**30**–**44**) and two-photon-induced PDT (**45**–**53**).

photosensitizer for PDT.[63] As suggested by DFT calculations, the high rigidity of the acceptor ligand can suppress the ring-stretching vibrations of the complex, while the introduction of a second iridium(III) center increases the exciton delocalization over the molecule, reducing vibronic coupling-induced non-radiative relaxations. These observations suggest that the construction of polynuclear complexes with a planar and π-conjugated acceptor ligand could be useful in the development of efficient NIR light-activatable photosensitizers.

Cameron, Alberto, McFarland, and co-workers have leveraged the attractive features of osmium(II) complexes and α-oligothiophene chromophores to develop an osmium(II) complex (**34**) as an NIR light-excitable photosensitizer with potent photocytotoxicity.[64] The α-oligothiophene pendant imparts a low-lying, long-lived ^{3}ILCT state (τ_o = 3–4 µs) that not only allows efficient photosensitization of $^1O_2$ (Φ_Δ = 0.95) but also promotes the generation of $O_2^{\bullet-}$ through autoionization reactions, resulting in extremely potent photocytotoxic activity toward SK-MEL-28 cells ($IC_{50,light}$ = 17.8 pM and 651 nM) with PI values of 3660000 and 91 under normoxia and hypoxia, respectively, upon visible-light irradiation. Remarkably, the complex remains highly photocytotoxic ($IC_{50,light}$ = 803 nM) upon irradiation with NIR light at low irradiance (733 nm, 100 J cm^{-2}). However, the complex is prone to aggregation in aqueous solutions due to the long α-oligothiophene chain, which leads to aggregation-induced quenching. To circumvent this problem, the complex has been encapsulated into liposomes and micelles.[65] Notably, the lipid nanoformulation not only enhances the luminescence properties of the complex in aqueous solutions but also increases the ^{3}ILCT state lifetimes, enhancing ROS production. In vivo luminescence imaging of the complex in an orthotopic murine head and neck AT-84 tumor model shows that the complex exhibits more efficient and selective tumor uptake when encapsulated in lipid-based vehicles, offering opportunities for image-guided PDT.

Cameron, Gujar, McFarland, and co-workers have developed an NIR light-absorbing ruthenium(II) complex (**35a**), featuring a chromophoric tridentate 2,2′-(4-(*tert*-butyl)pyridine-2,6-diyl)bis(1,8-naphthyridine) (tpbn) ligand and a π-expansive dppn ligand, as an immunoprotective PDT agent against aggressive melanoma.[66] The complex shows panchromatic absorption across the UV-visible to the NIR region, with absorption wavelengths reaching up to 800 nm. The NIR absorption can be tuned to longer wavelengths by modulating the ligand-field strength of the monodentate ligand and the degree of π-conjugation in the tridentate ligand. The strong NIR absorption enables effective population of the long-lived dppn-based ^{3}IL state upon photoexcitation with NIR light, resulting in highly efficient $^1O_2$ generation (Φ_Δ = 0.86) and thus high photocytotoxicity toward melanoma cells (A375, SK-MEL-28, and B16-F10; $IC_{50,light}$ = 1.56–2.57 µM). Notably, the PDT treatment elicits pro-inflammatory response and ICD in B16-F10 cells. Thus, vaccination of immunocompetent C57BL/6NCrl mice with the PDT-induced dying B16-F10 cells evokes protective immune response against tumor growth upon challenge with live B16-F10 cells (55 and 80% protection in male and female mice, respectively), significantly increasing tumor-free survival. Modification of the axial monodentate ligand affords complexes **35b** and **35c**, which display panchromatic absorption similar to their parent complex **35a**.[67] The MLCT absorption of complex **35c** is red-shifted relative to complex **35a**, attributed to the electron-donating *N*,*N*-dimethylamino group on the monodentate ligand that enhances the energy of the dπ orbital of the ruthenium(II) center. Notably, complexes **35b** and **35c** exhibit distinct immunomodulatory capabilities in vivo. Complex **35b** induces the surface exposure of heat shock proteins (Hsp70 and Hsp90) and calreticulin, while complex **35c** produces a higher amount of pro-inflammatory cytokines such as interleukin 6 (IL-6), tumor necrosis factor-α (TNF-α), and chemokine XC ligand 10 (CXCL10).

The incorporation of transition metal complexes with an NIR-absorbing organic chromophore represents a straightforward approach to encompass their absorption to the NIR region for overcoming depth-related challenges in clinical PDT applications.[68] Liu, Chao, and co-workers have developed a ruthenium(II) complex conjugated with an NIR-absorbing distyryl-BODIPY scaffold (**36**) for NIR light-mediated PDT.[69] The complex shows intense absorption in the NIR region ($\varepsilon_{652\,nm}$ = 1.2 × 10^5 M^{-1} cm^{-1}) due to the direct π-conjugated coupling to the BODIPY unit, enabling efficient $^1O_2$ generation (Φ_Δ = 0.77) upon irradiation with NIR light (660 nm). Notably, the complex displays higher photocytotoxic activity toward A375 cells than other cancerous and normal cells, which is attributed to its more efficient cellular uptake. Mechanistic studies indicate that after cellular internalization, the complex accumulates in the lysosomes and triggers lysosomal damage upon irradiation, leading to the release of lysosomal proteases like cathepsin B into the cytosol and ultimately initiating apoptosis. The selective photocytotoxicity of the complex toward A375 cells enables effective inhibition of tumor growth in A375 tumor-bearing mice upon irradiation without causing systemic toxicity. Liu, Wong, Gong, and co-workers have encapsulated an iridium(III) BODIPY complex (**37**) into human serum albumin (HSA) to afford an NIR light-activatable nanophotosensitizer for PDT.[70] The resultant nanoparticles (**HSA@37**) exhibit intense absorption at 740 nm (ε = 5.8 × 10^4 M^{-1} cm^{-1}), which enables efficient $^1O_2$ generation in cells upon NIR-light excitation, resulting in effective cancer cell death in vitro and in vivo. Additionally, the nanoparticles have been utilized for photoacoustic imaging (PAI) due to their intense NIR absorption, offering opportunities for PAI-guided PDT.

Gong, Zhang, Wong, and co-workers have developed an iridium(III) complex decorated with a Si-rhodamine moiety (**38**) as an NIR light-activatable photosensitizer for PDT against deep-seated tumors.[71] The presence of a Si-rhodamine unit leads to strong absorption in the NIR region ($\varepsilon_{713\,nm}$ = 8.9 × 10^4 M^{-1} cm^{-1}), while the increased π-conjugation of the cyclometalating ligand lowers the energy levels of the iridium(III)-based triplet excited states for populating the long-lived Si-rhodamine triplet state via energy transfer. As a result, the complex shows efficient $^1O_2$ photosensitization (Φ_Δ = 0.64) upon NIR-light irradiation. Additionally, the NIR fluorescence properties of the complex (λ_{em} = 744 nm) allow in vivo imaging with negligible autofluorescence background interference, enabling the clear visualization of the lesions in mice bearing 4T1 tumor xenografts. Importantly, exposure of the tumor region to continuous NIR-light irradiation results in effective suppression of tumor growth even when the tumors are located at a depth of 8.4 mm beneath a mimic epidermis.

Lin, Yang, Yang, and co-workers have developed an iridium(III) complex conjugated with a heptamethine cyanine

fluorophore (**39**) for PAI-guided NIR light-mediated PDT.[72] The complex has been encapsulated into PF127 using a solvent evaporation-induced self-assembly approach to afford water-soluble and photostable nanoparticles (**PM@39**) with intense absorption in the NIR region (λ_{abs} = 815 nm). Real-time monitoring of the pharmacokinetics and biodistribution of the nanoparticles in 4T1 tumor-bearing mice via PAI indicates that the nanoparticles have a long blood circulation half-life (ca. 18 h), and their tumor accumulation reaches the maximum at 24 h post-injection. Exposure of the tumor area to continuous NIR-light irradiation (808 nm, 90 J cm^{-2}) leads to significant suppression of tumor growth. Gandioso, Marchán, Gasser, and co-workers have also developed a ruthenium(II) cyanine complex (**40**) as an NIR light-activatable photosensitizer for the treatment of hypoxic tumors.[73] Notably, the incorporation of a heptamethine cyanine scaffold to the diimine ligand not only enhances the absorption (λ_{abs} = 766 nm) and emission (λ_{em} = 796 nm) of the complex in the phototherapeutic window but also promotes the cellular uptake and accumulation of the complex in the mitochondria. The efficient generation of ROS in the mitochondria upon irradiation via both Type I and Type II pathways results in high photocytotoxicity toward CT26 cells under both normoxic and hypoxic conditions ($IC_{50,light}$ = 0.33 and 0.62 μM, respectively). Sun and co-workers have developed a ruthenium(II) complex coordinated with a merocyanine-derived ligand (**41**) as a red light-responsive photosensitizer for PDT.[74] This complex displays strong absorption at 660 nm, arising from a metal–ligand-to-ligand charge-transfer (MLLCT) transition. Upon excitation at 450 nm, the complex exhibits ligand-based green fluorescence, allowing the tracking of its cellular uptake and localization. As revealed by LSCM, the complex specifically localizes in the lysosomes of MCF-7 cells after cellular internalization. Irradiation of the treated cells with red light triggers the production of $^1O_2$ and damages the lysosomes, inducing efficient cancer cell apoptosis. In vivo studies show that the complex is enriched in the tumor region of 4T1 tumor-bearing mice within 2 h after intratumoral injection, and subsequent exposure to red-light irradiation (671 nm, 120 J cm^{-2}) leads to significant tumor growth inhibition without causing systemic toxicity.

Low-bandgap semiconducting polymers are a class of π-conjugated polymers that show strong NIR absorption due to their small bandgap typically below 1.6 eV.[75] Zhang and co-workers have developed a metallopolymerization strategy to prepare narrow-bandgap iridium(III)-based metallopolymers (**42**) for PDT against hypoxic tumors.[76] In contrast to the monomeric complexes that display very weak absorption beyond 600 nm and the metal-free semiconducting polymers that exhibit very low ROS photosensitization efficiencies, the metallopolymers show both strong absorption in the deep-red region (for **42a**, ε_{669nm} = 11.93 × 10^4 M^{-1} cm^{-1}; for **42b**, ε_{660nm} = 9.00 × 10^4 M^{-1} cm^{-1}) and efficient production of ROS, particularly $O_2^{\bullet-}$, upon irradiation with a 680-nm laser. Owing to their amphiphilic structures, the metallopolymers self-assemble into polymer dots (Pdots) in aqueous solutions. These Pdots have been coated with a cell-penetrating octaarginine peptide R_8 via electrostatic interaction to promote their cellular uptake. The efficient production of $O_2^{\bullet-}$ inside cells upon irradiation results in high photocytotoxic activity even under hypoxic conditions. Furthermore, the metallopolymers have been coprecipitated with poly(styrene-*co*-maleic anhydride) (PSMA) for conjugation with the c(RGDyK) peptide to enhance their tumor-targeting capabilities. Compared to the unmodified Pdots, the c(RGDyK)-functionalized Pdots display more efficient tumor accumulation in vivo, inducing almost complete tumor ablation in 4T1 tumor-bearing mice upon irradiation with a 680-nm laser.

Upconversion nanoparticles (UCNPs) are a class of anti-Stokes' shift luminescent materials that can convert NIR light to light of shorter wavelengths such as UV and visible light, which have been exploited as a versatile light nanotransducer for photoactivation of various therapeutic agents.[77] Zhang, Gou, and co-workers have utilized lanthanide-doped UCNPs as a platform to develop an NIR light-activatable nanophotosensitizer (**UCNP-43@PF127@YC-1**) with hypoxia-inducible factor (HIF)-1α inhibition capabilities for PDT.[78] The nanophotosensitizer is constructed through the modification of oleic acid-capped $NaYF_4$:Yb/Tm@$NaYF_4$ UCNPs with an iridium(III) naphthalimide complex (**43**), followed by the encapsulation into PF127 and the physical adsorption of the HIF-1α inhibitor YC-1 into the hydrophobic layer at the surface of UCNPs. The direction conjugation of the iridium(III) complex with a naphthalimide moiety plays two important roles: 1) enhancing the visible-light absorption of the complex for harvesting the upconversion luminescence from the UCNPs; and 2) imparting a long-lived ^{3}IL state for $^1O_2$ photosensitization. These properties allow efficient $^1O_2$ generation upon NIR light irradiation through a sequential process of photon upconversion and Förster resonance energy transfer (FRET), leading to high photocytotoxicity toward human breast adenocarcinoma MDA-MB-231 cells. Notably, the photocytotoxic activity is further enhanced under hypoxia due to effective HIF-1α inhibition, which enables efficient $^1O_2$ generation even at low O_2 concentrations. In vivo studies show that the nanophotosensitizer exhibits efficient tumor accumulation in live mice bearing MDA-MB-231 tumor xenografts after tail vein injection and induces significant suppression of tumor growth upon NIR-light irradiation. Zhu, Bryce, Tang, Chang, and co-workers have coupled an AIE-active iridium(III) complex (**44**) and the carbonic anhydrase (CA)-IX inhibitor 4-(2-aminoethyl)benzenesulfonamide (ABS) to lanthanide-doped UCNPs to afford a mitochondria-targeting nanophotosensitizer (**UCNP-44@PAA-ABS**) for PDT against hypoxic tumors.[79] The conjugation of the iridium(III) complex to the UCNPs enables efficient ROS photosensitization upon NIR-light irradiation (980 nm), while the introduction of a CA-IX inhibitor assists in hypoxia alleviation to promote ROS generation in hypoxic cells. Thus, the nanophotosensitizer shows high photocytotoxicity toward MDA-MB-231 and 4T1 cells even under hypoxia ($IC_{50,light}$ = 2.6 and 5.8 μM, respectively) through the induction of apoptosis and ferroptosis. Furthermore, the nanophotosensitizer efficiently accumulates in the tumor tissue in 4T1 tumor-bearing mice after tail vein injection, and significantly inhibits tumor growth upon irradiation with a single dose of NIR light.

3.2. Two-Photon-Induced PDT

Two-photon absorption (TPA) is a second-order non-linear optical process, referring to the simultaneous absorption of two lower-energy photons instead of one to access the excited state

of a molecule.[80] Since two-photon excitation with NIR light offers the advantage of enhanced spatial precision, deeper penetration, and lower phototoxicity, it has found widespread biomedical applications including bioimaging, phototherapy, and drug delivery.[81]

Compared to traditional porphyrin-based photosensitizers such as porfimer sodium that possesses a small TPA cross-section in the NIR region ($\delta_{850\,nm}$ = 7.4 GM; 1 GM = 10^{-50} cm^4 s $photon^{-1}$),[82] transition metal complexes typically display stronger TPA properties due to the large changes in dipole moment involved in their charge-transfer transitions, which have facilitated their applications in two-photon-induced luminescence imaging and PDT.[83] Connor, Chao, Sadler, and co-workers have developed two luminescent iridium(III) complexes (**45**) as photosensitizers and examined their oxidative attack on proteins in live cells.[84] These complexes exhibit good TPA ($\delta_{750\,nm}$ = 115 and 70 GM), long emission lifetimes (τ_o = 389 and 109 ns), and high $^1O_2$ generation efficiencies (Φ_Δ = 0.70 and 0.82). The emission lifetimes of the complexes are further increased in live A549 cells due to the hydrophobic and hypoxic local environments, facilitating $^1O_2$ production. Thus, the complexes show high photocytotoxic activity toward A549 cells and MCTSs ($IC_{50,light}$ = 0.12–0.30 and 0.20–1.0 μM, respectively). Notably, the complexes display low or negligible cytotoxic activity toward MRC-5 cells and spheroids under both dark and light conditions (IC_{50} ≥ 40.7 μM). Proteomic studies indicate that the photogenerated $^1O_2$ oxidizes specific histidine residues in Hsp70 (His332) and aldose reductase (His188) in A549 cells to 2-oxohistidine. Furthermore, the PDT treatment upregulates the expression of nine unique enzymes involved in glycolysis, suggesting that the photoinduced oxidative stress triggers the malfunction of the mitochondria and increases the use of glucose to generate energy, resulting in a loop of ROS-stimulated glucose uptake and glucose-stimulated ROS production. Monitoring of the cellular and organelle morphological changes in human prostate cancer PC-3 cells using cryo-soft X-ray tomography (cryo-SXT) further indicates that the PDT treatment causes extensive and specific alterations to mitochondria.[85]

The TPA properties of transition metal complexes can be improved through a ligand regulation approach. Ma, Tian, and co-workers have developed an iridium(III) terpyridine complex (**46**) for two-photon-induced PDT.[86] This complex features a 3,4-diethoxyphenyl group as an electron donor and a terpyridine ring as an electron acceptor. The high coplanarity between the donor and acceptor units allows for efficient intramolecular electron transfer to occur, leading to large two-photon ($\delta_{780\,nm}$ = 138.2 GM) and three-photon absorption cross-sections ($\sigma_{1450\,nm}$ = 25.1 × 10^{-92} cm^6 s^2 $photon^{-2}$) in the NIR region. Additionally, the large conjugation in the benzo[*h*]quinoline ligand reduces the singlet–triplet energy gap and facilitates ISC, resulting in long-lived emission (τ_o = 1.107 μs) and efficient $^1O_2$ generation (Φ_Δ = 0.92). The complex has been used for in vivo tumor imaging, showing that it is enriched in the tumors of MCF-7 tumor-bearing mice for 12 h with negligible distribution to other organs after intratumoral injection. Selective irradiation of the tumor region with a 780-nm laser induces efficient cancer cell death through apoptosis and thus significant inhibition of tumor growth. Tian and co-workers have developed an AIE-active iridium(III) complex (**47**) for image-guided PDT.[87] The emission intensity and lifetime of the complex are sensitive to the viscosity of its local environment. Additionally, the complex displays strong two-photon ($\delta_{725\,nm}$ = 369 GM) and three-photon absorption ($\sigma_{1200\,nm}$ = 90 × 10^{-82} cm^6 s^2 $photon^{-2}$), offering the possibilities for imaging and PDT with multiphoton excitation. Real-time monitoring of changes in mitochondrial viscosity via lifetime imaging indicates the rapid induction of apoptotic cell death upon irradiation. Thus, treatment of HepG2 tumor-bearing mice with the complex and NIR light (730 nm, 10 min) leads to significant tumor regression.

Chao, Gasser, and co-workers have designed a series of ruthenium(II) complexes functionalized with styryl moieties (**48**) for two-photon-induced PDT.[88] Compared to $[Ru(bpy)_3]^{2+}$, these complexes exhibit red-shifted absorption and exceptionally strong TPA ($\delta_{750\,nm}$ up to ca. 6800 GM; **Figure 5a,b**). Among these complexes, complex **48g** shows the highest $^1O_2$ photosensitization efficiency (Φ_Δ = 0.75). The efficient generation of $^1O_2$ in cells triggers cell death through a combination of apoptosis and paraptosis pathways, resulting in almost complete eradication of a doxorubicin-resistant human colon adenocarcinoma SW620/AD300 tumor in vivo upon two-photon excitation (Figure 5c–e). Encapsulation of the complex into polymeric micelles with terminal biotin groups enhances it selectivity toward cancer cells over normal cells.[89] The resultant nanoparticles (**PM-Biotin@48g**) selectively accumulate in cancer cells, demonstrating over 20-fold more efficient cellular uptake in A549 cells compared to human lung fibroblast (HLF) cells. Importantly, the nanoparticles are essentially non-cytotoxic toward both cancerous (A549, A549/DDP, and HeLa) and non-cancerous cells (HLF) in the dark ($IC_{50,dark}$ > 494.7 μM). However, upon two-photon excitation, the cytotoxicity of the nanoparticles toward cancer cells significantly increases ($IC_{50,light}$ = 3.2–3.5 μM). In contrast, the photocytotoxic activity of the nanoparticles toward non-cancerous HLF cells is substantially lower ($IC_{50,light}$ = 48.2 μM) due to its lower cellular uptake. Remarkably, compared to the free complex, the nanoparticle formulation leads to a ca. 8.7-fold higher level of tumor accumulation in A549 tumor-bearing mice upon intravenous injection, enabling almost complete tumor eradication upon irradiation with an 808-nm laser. Related ruthenium(II) complexes (**49**) with large TPA cross-sections (up to 1600 GM) have also been developed.[90] These complexes display high photocytotoxicity toward exceptionally large MCTSs with a diameter of ca. 800 μm upon two-photon excitation (800 nm), inducing the complete destruction of the hypoxic center. The strong inhibition of tumor growth is also observed in vivo, resulting in almost complete tumor ablation in A549 tumor-bearing mice. Structure–activity relationship analysis of related ruthenium(II) complexes indicates that structural modifications of the distyryl ligand have a significant impact on the lipophilicity, cellular uptake efficiencies, and photocytotoxic activity of the complexes.[91] Liu, Gao, and co-workers have also developed a series of styryl-modified iridium(III) complexes (**50**) as two-photon-active luminescent probes and photosensitizers.[92] All the complexes specifically localize in the mitochondria after cellular uptake due to their cationic and lipophilic character. Notably, the complexes are essentially non-cytotoxic in the dark ($IC_{50,dark}$ ≥ 164 μM) but become highly photocytotoxic toward cancer cells upon two-photon excitation

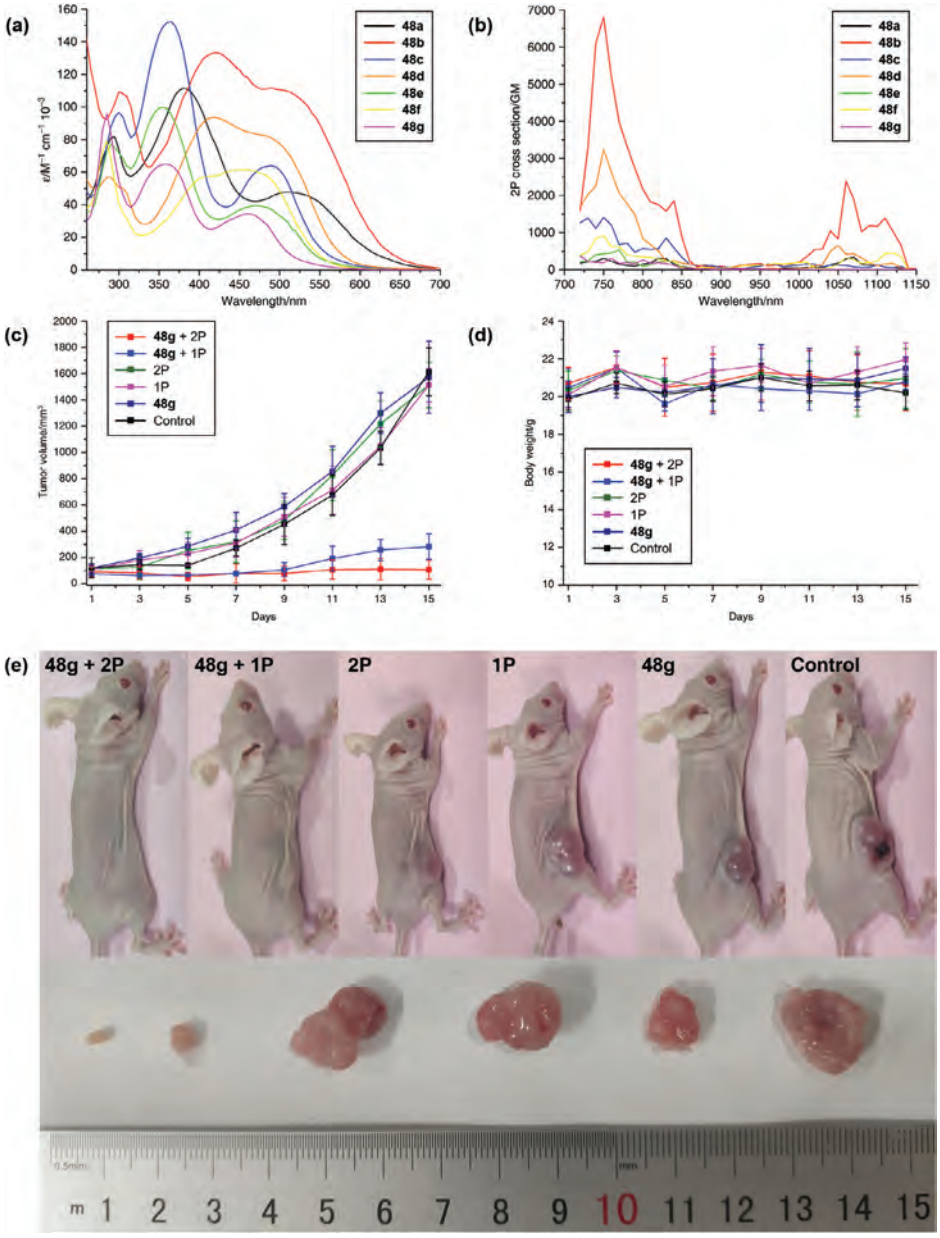

Figure 5. a) One-photon absorption spectra of complexes **48** in CH_3CN. b) Two-photon absorption spectra of complexes **48** in CH_2Cl_2. c) Tumor growth curves and d) body weight of SW620/AD300 tumor-bearing mice under different treatments ($n = 5$). e) Representative photographs of SW620/AD300 tumor-bearing mice and the dissected tumors after different treatments. Control: saline; complex **48g**: 2 mg kg^{-1}; 1P: 500 nm, 10.0 mW cm^{-2}, 1 h, 36 J cm^{-2}; 2P: 800 nm, 50 mW, 1 kHz, pulse width 35 fs, 5 s mm^{-1}. Adapted with permission.[88] Copyright 2020, Springer Nature.

(22Rv1, A549, and MCF-7; $IC_{50,light}$ = 0.96–11.7 μM) due to their strong TPA ($\delta_{800\,nm}$ = 113–168 GM) and efficient $^1O_2$ generation (Φ_Δ = 0.37–0.95). Systemic regulation of the cyclometalating ligands and the substituents on the styryl-functionalized diimine ligand has led to the identification of a nitro-substituted iridium(III) complex (**51**) as an efficient two-photon-excitable photosensitizer.[93] This complex exhibits efficient two-photon-induced $^1O_2$ generation (Φ_Δ = 0.12) due to its large TPA cross-section ($\delta_{808\,nm}$ = 391 GM), resulting in potent photocytotoxicity toward A375 cells ($IC_{50,light}$ = 0.113 μM) and effective suppression of A375 tumor growth in vivo with a tumor inhibition rate (TIR) of 85% upon irradiation with a low-power 808-nm laser (30 J cm^{-2}).

Chao, Stang, and co-workers have designed a heterometallic ruthenium(II)–platinum(II) metallacycle (**52**) as a two-photon-active PDT agent.[94] The [2+2] metallacycle is formed upon the coordination-driven self-assembly of the ruthenium(II)-based photosensitizer $[Ru(bpy)_2(qpy)]^{2+}$ (qpy = 4,4′:2′,2″:4″,4‴-quaterpyridine) with a platinum(II) bisphosphine complex. The incorporation of the ruthenium(II) complex into a rigid metallacyclic structure extends its molecular orbital onto the platinum(II) center and enhances its polarization, resulting in a large

TPA cross-section in the NIR region ($\delta_{800\,nm}$ = 1371 GM). Furthermore, platination of the ruthenium(II) complex leads to red-shifted emission (λ_{em} = 696 nm) due to stabilization of the π^* orbital of the qpy ligand, and increased $^1O_2$ generation (Φ_Δ = 0.89) due to enhanced ISC. The metallacycle shows efficient cellular uptake in A549 cells and dual localization in both the mitochondria and nucleus. Upon two-photon excitation (820 nm), it induces significant cancer cell apoptosis due to efficient $^1O_2$ generation that leads to MMP reduction and nuclear DNA fragmentation. As a result, the metallacycle efficiently inhibits the growth of solid tumors with minimal side effects in A549 tumor-bearing mice. A higher-order 3D octahedral [6+4] metallacage has been prepared through the coordination-driven self-assembly of $[Ru(bpy)_2(qpy)]^{2+}$ with a triangular platinum(II)-based building block.[95] The metallacage displays strong TPA ($\delta_{820\,nm}$ = 5468 GM), deep-red luminescence (λ_{em} = 673 nm), and efficient $^1O_2$ generation (Φ_Δ = 0.85). The metallacage has been formulated into nanoparticles through encapsulation into DSPE-PEG to promote its cellular uptake. The resultant nanoparticles specifically accumulate in the lysosomes after cellular internalization, and efficiently induce lysosomal disruption through $^1O_2$ generation upon two-photon excitation, resulting in high photocytotoxicity. In vivo studies show that exposure of the tumor region to NIR light (820 nm) after intratumoral injection of the nanoparticles into A549 tumor-bearing mice leads to significant tumor growth inhibition with low systemic toxicity. Pan, Su, and co-workers have also utilized iridium(III) quaterpyridine complexes (**53**) as a bridging unit to assemble with Pd^{2+}, forming luminescent cubic [8+4] metallacages for bioimaging and PDT applications.[96] Compared to the precursor complexes, the metallacages exhibit larger TPA cross-sections due to the enlarged π-conjugation plane across the molecules. Furthermore, the metallacages show higher cellular uptake and localize in the mitochondria. Thus, upon irradiation, the metallacages produce $^1O_2$ that damages the mitochondria and induce caspase-3/7-mediated apoptosis, resulting in efficient cancer cell death in vitro and in vivo.

3.3. Discussion

As a critical component in PDT, light provides both spatial and temporal control over ROS production, enabling a level of tumor targeting that is unattainable with traditional anticancer therapies. Since long-wavelength light (ca. 650–900 nm) allows for deeper tissue penetration, the development of transition metal complexes compatible with red or NIR light excitation will broaden their medical applications. Various ligand engineering strategies have been used to extend the absorption of transition metal complexes into the NIR region, such as manipulating the electronic properties or extending the π-conjugation of the ligands to modulate the highest occupied molecular orbital (HOMO) and lowest unoccupied molecular orbital (LUMO) of the complexes, and conjugating the complexes with an NIR light-absorbing organic chromophore. A judicious selection of metal centers can also shift the absorption and emission profiles of the complexes into the NIR region. The use of UCNPs to convert NIR light into UV or visible light represents another promising avenue. The advancement of two-photon-active transition metal complexes for two-photon-induced PDT offers an alternative solution. The TPA cross-sections of transition metal complexes can be enhanced through the introduction of electron donors and acceptors via a π-conjugated linker to extend the π-conjugation plane and enhance the push–pull electronic effect across the molecules,[80] or the incorporation of two-photon light-absorbing chromophores (e.g., squaraine)[80] or nanomaterials (e.g., quantum dots, gold nanorods, semiconducting polymer nanoparticles)[97] as two-photon light-harvesting units. Although NIR light can extend the penetration depth to about 1 cm, this is still insufficient for treating deep-seated tumors. One solution is the direct implantation of a wireless photonic device near the tumor site, enabling low-dose, long-term PDT in deep tissues.[98] Another promising approach is developing self-illuminating systems that use chemiluminescent agents as internal light sources, overcoming the penetration depth limitations of external light sources in traditional PDT.[99] Advances in 1,2-dioxetane derivatives have led to chemiluminescent agents with various emission wavelengths and stimuli-responsiveness,[100] offering new opportunities for treating deep-seated diseases.

4. Transition Metal Complexes for Organelle-Targeted PDT

Since most ROS have a short lifetime (ca. 30–180 µs) and a limited range of action (ca. 10–20 nm) in biological environments, the subcellular localization of photosensitizers is crucial for the effectiveness of PDT.[101] Subcellular organelles such as the nucleus, mitochondria, lysosomes, and ER are integral to regulating cell metabolism and maintaining a balance between cell proliferation and death. Thus, targeting photosensitizers to these organelles, which are hypersensitive to ROS, is a promising approach to enhance therapeutic outcomes.

4.1. Nucleus-Targeted PDT

The nucleus is the most important organelle of eukaryotic cells, hosting most genetic materials of the cells and regulating gene expression to control cellular behavior.[102] Since the nucleus plays an important role in cell survival and death and cellular metabolism, it has emerged as a major target of various therapeutic agents used in cancer therapy.[103]

Tian, Tian, and co-workers have developed an iridium(III) complex (**54**) (**Figure 6**) that specifically targets the nucleus for two-photon-induced PDT.[104] The terminal ester group on the terpyridine ligand plays a key role in facilitating the cellular internalization and nuclear accumulation of the complex via microtubule-dependent endocytosis. Upon irradiation, the complex is released from the nucleus to the mitochondria, inducing significant cancer cell death by causing sequential photodamage to these organelles. Furthermore, the complex can inhibit tumor growth by 41.58% in vivo upon irradiation with a two-photon laser (808 nm), a rate similar to the clinical PDT agent chlorin e6 (40.76%).

Huang, Sadler, and co-workers have developed an iridium(III) complex appended with two thiol-reactive maleimide moieties (**55**) for conjugation to HSA to afford a photofunctional protein conjugate (**HSA-55**) for PDT.[105] The protein conjugation

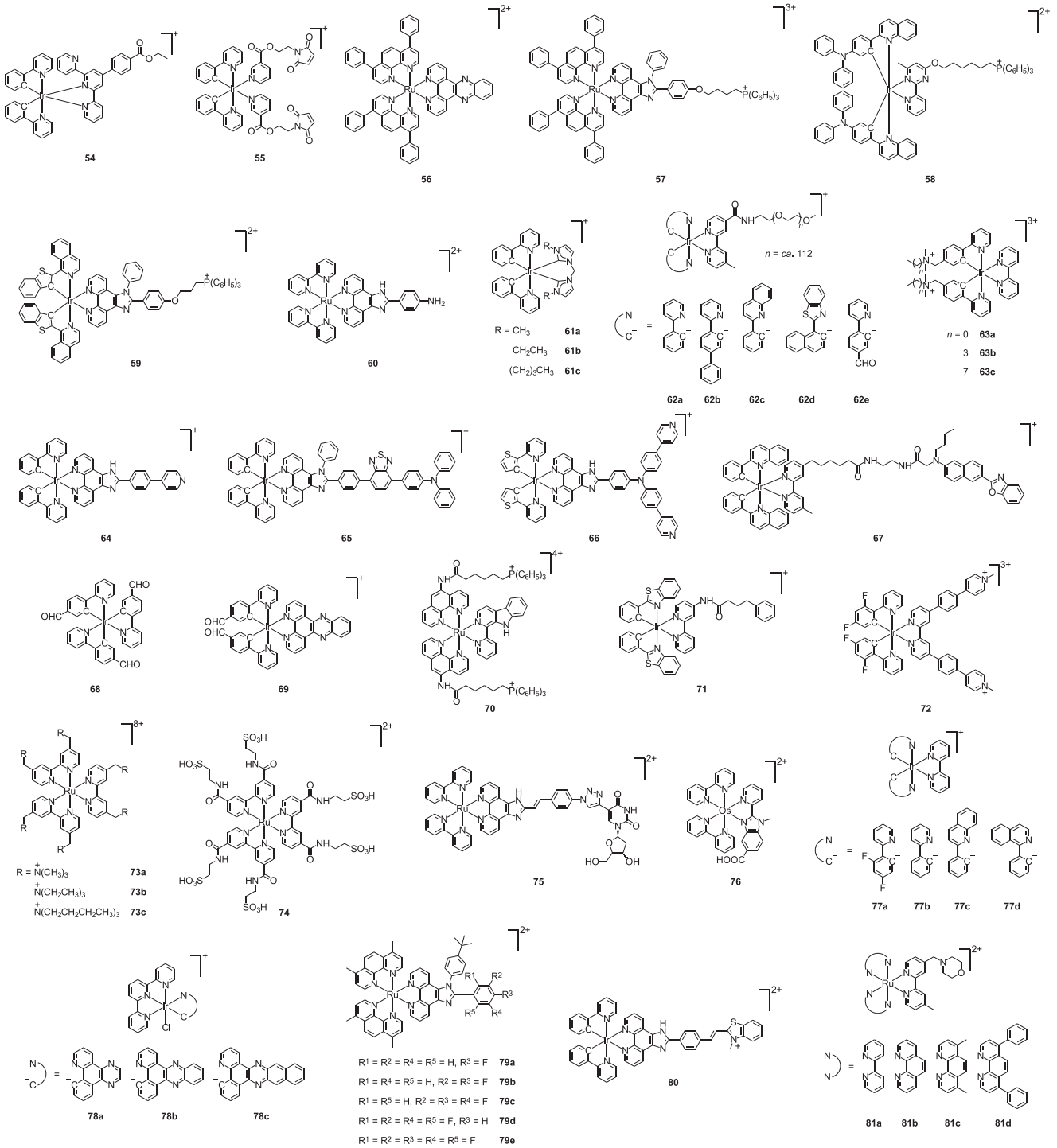

Figure 6. Structures of transition metal complexes for nucleus-targeted (**54**–**56**), mitochondria-targeted (**57**–**72**), lysosome-targeted (**73**–**76**), ER-targeted (**77** and **78**), and dual-organelle-targeted PDT (**79**–**81**).

not only switches on the emission and $^1O_2$-photosensitization properties of the complex but also facilitates its transport into the cell nucleus. Remarkably, the protein conjugate **HSA-55** displays negligible dark cytotoxicity toward cancer cells (A549, A549/DDP, and HepG2) ($IC_{50,dark}$ = 62.3–85.6 μM) but high photocytotoxic activity upon irradiation ($IC_{50,light}$ = 1.1–2.3 μM) due to efficient ROS generation, while remaining non-cytotoxic toward non-cancerous cells (LO2 and MRC-5) under both dark and light conditions (IC_{50} = 66.4–96.4 μM). This cancer-selective photocytotoxicity is also observed in 3D multicellular spheroids of cancer A549 cells ($IC_{50,light}$ = 4.8 μM) and normal MRC-5 cells ($IC_{50,light}$ > 100 μM).

Zhu and co-workers have utilized an ion-pairing approach for delivering the ruthenium(II) complex $[Ru(Ph_2\text{-phen})_2(dppz)]^{2+}$ (**56**) (Ph_2-phen = 4,7-diphenyl-1,10-phenanthroline) to the cell nucleus.[106] This complex is well-known as a molecular light-switch for DNA, showing emission turn-on upon DNA binding.[107] However, its limited nuclear uptake has hindered its effective targeting of nuclear DNA.[108] Interestingly, binding of the complex to hydrophobic weak acid counteranions such as 3,5-dichlorophenolate or flufenamate redirects it from the cytoplasm to the cell nucleus. Notably, only the Δ-isomer of the complex is selectively translocated into the nucleus, while the Λ-isomer remains trapped in the cytoplasm, which is attributed to their differential binding affinities for nuclear DNA and cytoplasmic proteins. The enantioselective cytoplasm-to-nucleus translocation of the complex enables the induction of DNA damage and apoptosis upon continuous visible-light irradiation.

4.2. Mitochondria-Targeted PDT

Mitochondria, which serve as the powerhouses of the cell responsible for energy production, play a pivotal role in various cellular processes.[109] Mitochondrial outer membrane permeabilization will lead to the release of pro-apoptotic proteins such as caspases into the cytosol, inducing apoptosis.[110] Thus, mitochondria have gained increasing attention as a prominent target for overcoming the resistance in current anticancer therapies.[111]

The conjugation of transition metal complexes with a cationic and lipophilic triphenylphosphonium (TPP) unit represents a versatile approach to promote their transport and accumulation in the mitochondria.[112] Chao and co-workers have designed a luminescent ruthenium(II) complex modified with a TPP moiety (**57**) as a mitochondria-targeting photosensitizer for two-photon-induced PDT.[113] Compared to its TPP-free counterpart ($IC_{50,light}$ = 13.1 μM), the introduction of a cationic TPP unit to the complex increases its cellular uptake efficiency and mitochondria specificity, resulting in substantially enhanced photocytotoxicity toward HeLa cells ($IC_{50,light}$ = 3.5 μM). Furthermore, the complex shows efficient penetration into HeLa MCTSs and $^1O_2$ generation upon two-photon excitation (830 nm, 800 J cm^{-2}) due to its large TPA cross-section ($\delta_{830\ nm}$ = 198 GM), effectively inhibiting the growth of MCTSs ($IC_{50,light}$ = 1.9 μM). Zhao, Huang, and co-workers have also developed a TPP-functionalized iridium(III) complex (**58**) for mitochondria-targeted PDT.[114] Notably, the mitochondrial accumulation of the complex leads to effective inhibition of mitochondrial respiration, resulting in a higher mitochondrial O_2 concentration for $^1O_2$ production. Thus, the complex displays significantly higher photocytotoxic activity toward HeLa cells even under hypoxia than its TPP-free counterpart that primarily targets the lysosomes. Chen, Guo, He, and co-workers have developed two iridium(III) complexes that can function as Type I photosensitizers and induce ferroptosis in hypoxic cancer cells through the generation of $O_2^{\bullet-}$ and HO•.[115] Notably, the TPP-containing complex (**59**) specifically accumulates in the mitochondria and, upon irradiation, induces MMP reduction and ATP production suppression, initiating apoptotic cell death pathways alongside ferroptosis. The synergetic effect of ferroptosis and apoptosis leads to the enhanced photocytotoxicity of complex **59** relative to its TPP-free counterpart toward refractory cancer cell lines such as triple-negative breast cancer (TNBC) MDA-MB-231 cells and apoptosis-resistant human pancreatic cancer PANC-1 cells under hypoxic conditions ($IC_{50,light}$ = 1.45 and 4.77 μM, respectively). The complex can also effectively inhibit the growth of MCF-7 MCTSs upon irradiation, highlighting its potential to eradicate hypoxic solid tumors in vivo. Rau, Weil, and co-workers have modified HSA with multiple TPP moieties and ruthenium(II) complexes (**60**) to afford a protein-based mitochondria-targeting photosensitizer (**HSA-TPP-60**) for PDT.[116] Compared to the free complex, the protein conjugate exhibits enhanced luminescence and $^1O_2$ generation efficiency due to the suppression of non-radiative decay pathways upon protein conjugation. Remarkably, the efficient accumulation of conjugate **HSA-TPP-60** in the mitochondria leads to very high photocytotoxic activity toward HeLa cells ($IC_{50,light}$ = 34.9 nM), which is ca. 220-fold higher than that of the free complex **60** ($IC_{50,light}$ = 7.7 μM). Further modification of the protein conjugate with an NIR light-excitable carbon dot (Cdot) yields a two-photon-active photosensitizer (**HSA-TPP-60-Cdot**) for mitochondria-targeted two-photon-induced PDT.[117] The FRET from the Cdot to the ruthenium(II) complex enables efficient production of $^1O_2$ in the mitochondria of cells upon two-photon excitation with NIR light at a low light dose (810 nm, 6.3 J cm^{-2}). This results in significant distortion of the mitochondrial morphology from filamentous structures to spheroid aggregates.

Cationic and lipophilic transition metal complexes can be directed to the mitochondria without the introduction of a targeting vector. For example, Mao and co-workers have developed three iridium(III) bis(*N*-heterocyclic carbene) complexes (**61**) as mitochondria-targeting theranostic agents.[118] Upon their cellular uptake and mitochondrial accumulation, the complexes initiate a cascade of events associated with mitochondrial damage including ROS production, cytochrome *c* release, caspase activation, and apoptosis, inducing significant cancer cell death ($IC_{50,dark}$ = 1.0–5.7 μM). The cytotoxic activity of the complexes is further enhanced upon irradiation ($IC_{50,light}$ = 0.86–160 nM). However, the high dark cytotoxicity of these complexes remains a concern. Thus, various design strategies have been implemented to improve the biocompatibility of mitochondria-targeting complexes. Lam, Cheng, Lo, and co-workers have developed a series of luminescent iridium(III) complexes modified with a PEG pendant (**62**) as mitochondria-targeting photosensitizers for PDT applications.[119] Notably, the PEG complexes show substantially reduced dark cytotoxicity ($IC_{50,dark}$ > 300 μM) compared to their PEG-free counterparts ($IC_{50,dark}$ = 0.12–136.8 μM), as the PEG unit can protect the complexes from interacting with intracellular components. Furthermore, PEGylation does not interfere with the mitochondria-targeting capabilities of the complexes; thus, the complexes specifically accumulate in the mitochondria after cellular uptake and efficiently generate $^1O_2$ upon irradiation, leading to significant oxidative damage to the mitochondria and thus the induction of necrosis. Xie, Hou, and co-workers have developed a series of amphiphilic iridium(III) complexes (**63**) as mitochondria-targeting theranostic agents for imaging and PDT.[120] Owing to the presence of two quaternary ammonium moieties as hydrophilic head groups and two long alkyl chains as hydrophobic tails, these complexes spontaneously self-assemble into vesicle-like nanostructures in aqueous media. The formation of

vesicles minimizes intermolecular π–π interaction and reduces non-radiative decay, substantially increasing their emission intensities and lifetimes and $^1O_2$ generation efficiencies. The formation of vesicles can also avoid non-specific interactions with cellular proteins. Thus, the complexes display negligible cytotoxic activity toward HepG2 and MCF-7 cells in the dark ($IC_{50,dark}$ > 300 μM) but high photocytotoxicity upon irradiation ($IC_{50,light}$ = 1.2–4.0 μM), enabling efficient inhibition of tumor growth in vivo without causing significant toxicity. The encapsulation of transition metal complexes into biocompatible carriers represents an alternative approach to improve their bioavailability and biocompatibility. Cationic, AIE-active iridium(III) complexes such as **64**,[121] **65**,[122] and **66**[123] have been developed as mitochondria-targeting photosensitizers for two-photon-induced PDT. These complexes exhibit increased emission intensities and ROS generation efficiencies in aqueous solutions due to aggregate formation. To improve their solubility while retaining their high ROS generation efficiencies in the aggregated state, these complexes have been encapsulated into phospholipid- or protein-based nanocarriers. The resultant nanoparticles show strong TPA and specific mitochondria localization, inducing mitochondria-mediated cancer cell apoptosis upon two-photon irradiation. In vivo studies show that the nanoparticles display excellent biocompatibility and induce significant tumor growth suppression with over 90% reduction in tumor volume upon two-photon excitation, prolonging the survival rate of the animals.

To shed light on the molecular targets of mitochondria-targeting photosensitizers, Seo, Kwon, and co-workers have developed a multifunctional iridium(III) complex (**67**) that enables the induction of mitochondrial oxidative stress and simultaneous monitoring of the mitochondrial response.[124] The complex incorporates an acedan derivative as a light-harvesting unit for the iridium(III)-based photosensitizer. The FRET efficiency between these two entities is highly sensitive to the local environment of the complex, allowing the complex to report on alternations in viscosity and polarity by photophysical changes. Studies on the mechanism of cell death through phenomenological observations and proteomic analysis reveal that the photogenerated ROS crosslink proteins around the mitochondria, leading to an increase in mitochondrial viscosity, which, in turn, reduces the diffusion of metabolites within the mitochondria and thus disrupts mitochondrial functions such as ATP production. Additionally, the photogenerated ROS oxidize proteins that maintain MMP, resulting in mitochondrial depolarization and swelling.

In addition to mitochondrial proteins, mtDNA is a promising target for PDT due to its high susceptibility to ROS-induced damage. He, Duan, and co-workers have designed a series of luminescent iridium(III)-based triple-stranded dinuclear metallohelices with structure-inherent DNA-targeting properties as photosensitizers targeting mtDNA.[125] These metallohelices are prepared from the reductive amination of *fac*-[Ir(pba)$_3$] (**68**) (Hpba = 4-(2-pyridyl)benzaldehyde) with a linear 1,2-diamine linker (2–5 carbons), wherein the length and odd–even character of the diamine spacer determines the formation of ΔΛ-mesocate (odd) or ΔΔ-/ΛΛ-helicate (even). Both mesocates and helicates exhibit similar $^1O_2$ generation efficiencies (Φ_Δ = 0.300–0.331) and specific mitochondrial localization. However, while all the metallohelices are essentially non-cytotoxic in the dark ($IC_{50,dark}$ > 30 μM), the photocytotoxic activity of the mesocates ($IC_{50,light}$ = 0.9–3.9 μM) is considerably higher than that of the helicates ($IC_{50,light}$ ≥ 5.2 μM). The enantiomer-dependent photocytotoxicity has been ascribed to the higher DNA-binding affinities of the mesocates, which induce more significant $^1O_2$-mediated cleavage of mtDNA upon irradiation and thus more pronounced cell death. A pair of homochiral and cationic double-stranded dinuclear metallohelicates have been developed using the Δ-/Λ-isomer of [Ir(pba)$_2$(dppz)]$^+$ (**69**) as the module and their spatially matching chiral (1*S*,2*S*)-/(1*R*,2*R*)-*trans*-1,2-cyclohexanediamine (*SS*-/*RR*-CHDA) as the linker.[126] Both of the optically pure metallohelicates, [(Δ-**69**)$_2$(*SS*-CHDA)$_2$]$^{2+}$ and [(Λ-**69**)$_2$(*RR*-CHDA)$_2$]$^{2+}$, show negligible cytotoxic activity toward A549 cells in the dark ($IC_{50,dark}$ > 300 μM) but very distinctive photocytotoxicity upon irradiation ($IC_{50,light}$ = 4.69 and 700.60 nM, respectively). Studies on the mechanism of action reveal that the chirality-induced photocytotoxicity is associated with the migration of [(Δ-**69**)$_2$(*SS*-CHDA)$_2$]$^{2+}$ from the mitochondria to the nucleus through an ATP-dependent transport pathway upon irradiation, which leads to the inhibition of SOD1 and eukaryotic translation initiation factor 5A (EIF5A) in the nucleus, inducing nuclear $O_2^{\bullet-}$ accumulation and downregulating messenger RNA (mRNA) splicing and translation, respectively. As a result, [(Δ-**69**)$_2$(*SS*-CHDA)$_2$]$^{2+}$ exerts a better phototherapeutic effect in A549 tumor-bearing mice than [(Λ-**69**)$_2$(*RR*-CHDA)$_2$]$^{2+}$, resulting in more significant inhibition of tumor growth and thus an increased survival rate. Zhang, Tan, and co-workers have designed an mtDNA-targeting ruthenium(II) β-carboline complex (**70**) as a photoactivator of the cyclic GMP-AMP synthase–stimulator of the interferon gene (cGAS–STING) pathway for cancer immunotherapy.[127] The incorporation of the cationic and lipophilic TPP moieties into the complex not only facilitates its accumulation in the mitochondria but also enhances its interaction with DNA, leading to DNA aggregation. Additionally, the complex can self-assemble into carrier-free nanoparticles due to the formation of multiple non-covalent intermolecular interactions, enhancing its cellular internalization via endocytosis. As a consequence, the complex can efficiently target and, upon irradiation, induce damage to mtDNA. The release of mtDNA into the cytosol triggers the activation of the cGAS–STING signaling pathway to elicit antitumor immune response, which significantly inhibits the growth of both the primary tumor and the distant tumor that is not irradiated in a bilateral mouse model bearing 4T1 tumor xenografts.

While mitochondria are known to play a central role in apoptosis, they have also been implicated in other forms of regulated cell death including necroptosis, ferroptosis, and pyroptosis that are involved in immune response regulation.[128] Gasser, Chao, and co-workers have developed a mitochondria-targeting iridium(III) complex (**71**) for two-photon-induced photodynamic immunotherapy.[129] This complex displays high photocytotoxic activity ($IC_{50,light}$ = 0.42–1.53 μM) toward a range of cancer cell lines, including breast cancer (MDA-MB-231 and 4T1), lung cancer (A549 and Lewis lung carcinoma), colon cancer (SW620 and CT26), and melanoma (A375 and B16-F10). Remarkably, exposure of the primary tumor in bilateral B16-F10 tumor-bearing mice to the complex and two-photon irradiation leads to strong inhibition of the growth of both primary and distant tumors due to immune activation. The induction of oxidative stress in

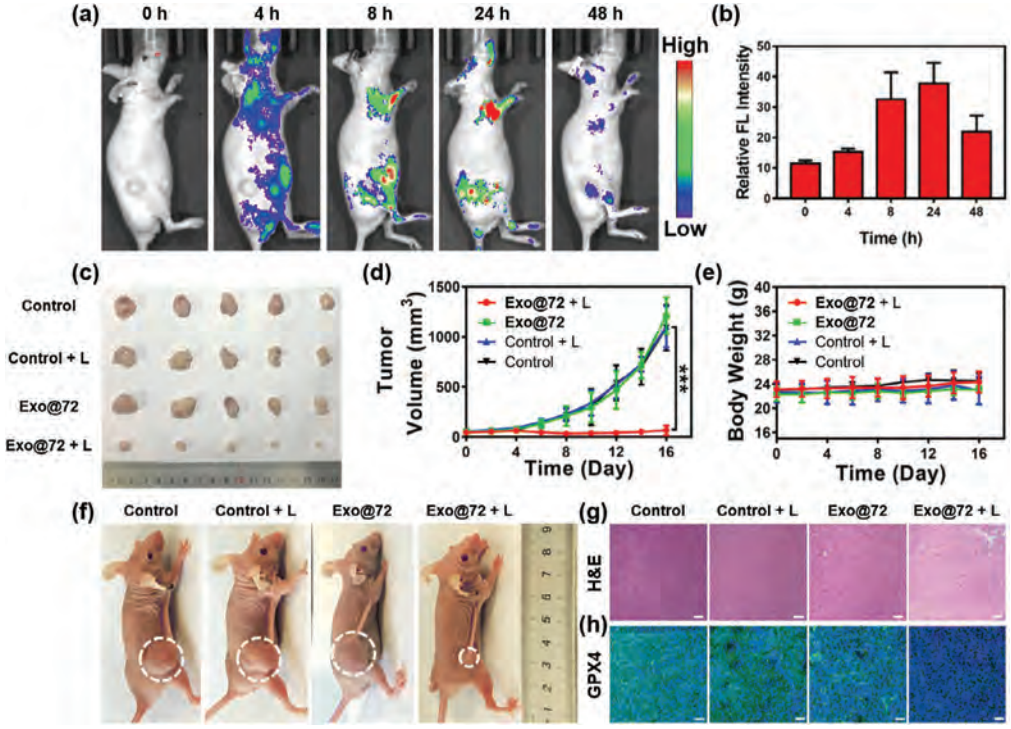

Figure 7. a) Luminescence images of an A375 tumor-bearing mouse administrated with **Exo@72** (5 mg kg^{-1}) through intravenous injection. The images were taken at 0, 4, 8, 24, and 48 h postinjection. λ_{ex} = 430 nm, λ_{em} = 520–580 nm. b) Time-dependent changes in the luminescence intensity in the tumor ($n = 3$). c) Representative photographs of the tumors dissected from A375 tumor-bearing mice after different treatments. d) Tumor growth curves and e) body weight of A375 tumor-bearing mice under different treatments ($n = 5$). ***$p < 0.001$. f) Representative photographs of A375 tumor-bearing mice after different treatments. The tumor sites are marked with white dashed circles. g) Hematoxylin and eosin (H&E) and h) GPX4 staining images of tumor tissues harvested from A375 tumor-bearing mice after different treatments. Scale bar = 50 µm. Control: saline; **Exo@72**: 5 mg kg^{-1}; L: 720 nm, 50 mW, 300 s. Adapted with permission.[130] Copyright 2024, Royal Society of Chemistry.

the mitochondria through the photogeneration of $O_2^{\bullet-}$ and $^1O_2$ triggers ferroptosis and ICD, which not only activates cytotoxic T cells and depletes regulatory T cells but also increases the number of effector memory T cells, stimulating long-lasting antitumor immune response inside the animal. A mitochondria-targeting pyridinium-functionalized iridium(III) complex (**72**) has also been developed for two-photon-induced photodynamic immunotherapy against melanoma.[130] The generation of oxidative stress in the mitochondria disrupts the mitochondrial respiratory chain and thereby disturbs mitochondrial oxidative phosphorylation and glycolysis, triggering cancer cell death through a combination of ferritinophagy (a selective form of autophagy that induces ferroptosis) and ICD. The complex has been encapsulated into exosomes derived from melanoma cells (A375 or B16-F10) for selective targeting of homologous tumor cells. As revealed by in vivo imaging, the resultant nanoparticles (**Exo@72**) exhibit maximal tumor accumulation in A375 tumor-bearing mice at 24 h after tail vein injection (**Figure** 7a,b). Subsequent exposure of the tumor region to two-photon irradiation (720 nm) leads to almost complete eradication of the tumors (Figure 7c–h). The PDT-induced immune response has been examined in bilateral B16-F10 tumor-bearing mice, showing that the PDT treatment promotes DC maturation and reprograms the immunosuppressive TME, generating robust and long-lasting antitumor immune response that can eliminate both the primary and distant tumors.

4.3. Lysosome-Targeted PDT

Lysosomes are membrane-bound organelles containing numerous hydrolytic enzymes for the degradation of macromolecules and recycling of their building blocks to regulate cellular homeostasis.[131] Lysosomal membrane permeabilization (LMP) will release cathepsins and other lysosomal enzymes into the cytosol, initiating cell death via different pathways such as apoptosis, autophagy, and necrosis.[132] Thus, targeting the lysosomes in cancer cells has emerged as a new therapeutic approach for cancer treatment.[133]

Gasser, Chao, and co-workers have developed three octacationic ruthenium(II) complexes (**73**) as lysosome-targeting photosensitizers for two-photon-induced PDT.[134] The introduction of polar ammonium groups facilitates the binding of the complexes to the cellular membrane, promoting their cellular internalization via an endocytic pathway and facilitating their trafficking to the lysosomes. Upon two-photon excitation, these complexes produce a significant amount of $^1O_2$ due to their strong TPA ($\delta_{800\,nm}$ = 185–250 GM) and high $^1O_2$ photosensitization efficiencies (Φ_Δ = 0.92–0.99). The photogenerated $^1O_2$ oxidizes the lysosomal membrane, releasing the complexes to the nucleus to induce oxidative stress and trigger cell death via necrosis. As a result, the complexes show high photocytotoxicity toward HeLa cells and MCTSs ($IC_{50,light}$ = 1.1–2.9 and 1.9–21.2 µM, respectively).

Zhang and co-workers have developed a taurine-modified ruthenium(II) complex (**74**) as a PDT agent targeting brain cancer cells.[135] The introduction of taurine substituents enhances its affinity for cancer cells through targeting the lysosomes. Additionally, the taurine modification increases the emission intensity and lifetime of the complex, facilitating the photosensitization of ROS. Thus, upon irradiation of the treated cells, the photogenerated ROS damage the lysosomal membrane, facilitating the lysosomal escape of the complex and the production of ROS in the cytoplasm. Notably, the photoinduced cell death is more prominent in brain cancer F98 cells than other cancer cell lines such as A375, A549, and HeLa cells, highlighting the potential use of the complex for the treatment of brain cancer with PDT.

Mei and co-workers have developed a uridine-modified ruthenium(II) complex (**75**) as a lysosome-targeting photosensitizer for the treatment of TNBC.[136] The complex specifically targets the lysosomes of MDA-MB-231 cells via binding to lysosomal integral membrane protein (LIMP)-2, one of the most abundant proteins distributed on the surface of the lysosomal membrane. Upon irradiation (650 nm), the complex efficiently generates $O_2^{\bullet-}$ and $^1O_2$, resulting in significant cell death ($IC_{50,light}$ = 1.09 μM). Notably, the photocytotoxic activity of the complex toward MDA-MB-231 cells is further enhanced under hypoxia ($IC_{50,light}$ = 0.36 μM), which is significantly higher than that toward non-TNBC MCF-7 cells and normal human breast epithelial MCF-10A cells ($IC_{50,light}$ = 36.03 and > 100 μM, respectively), offering a new therapeutic approach for treating TNBC.

Zhang, Zhang, Chao, and co-workers have developed an NIR luminescent osmium(II) complex (**76**) for lysosome-targeted imaging and PDT.[137] This complex displays MLCT absorption at 488 and 683 nm and NIR emission at 736 nm due to the higher-lying dπ orbital of the osmium(II) center, enabling the photosensitization of $^1O_2$ with red light (633 nm). Upon cellular internalization, the osmium(II) complex specifically localizes in the lysosomes, which is different from its ruthenium(II) counterpart that preferentially accumulates in the mitochondria. Importantly, the complex is essentially non-cytotoxic in the dark but exhibits substantially enhanced cytotoxicity toward cancer cells upon red-light irradiation (633 nm) due to $^1O_2$ generation. Notably, the complex shows negligible cytotoxic activity toward normal MRC-5 cells under both dark and light conditions.

4.4. ER-Targeted PDT

The ER is the largest membrane-bound organelle in the cell, being the major site of protein synthesis, folding, posttranslational modifications, and trafficking.[138] It also plays an important role in lipid and steroid synthesis, calcium storage, and xenobiotic metabolism. Perturbations to ER homeostasis will lead to the accumulation of unfolded/misfolded proteins, resulting in excessive ER stress and thus inducing cell apoptosis.[139] Furthermore, the induction of ER stress often leads to ICD, which can remodel the immunosuppressive TME to provoke robust and long-lasting protective antitumor immune response.[140] Thus, the ER has emerged as a promising target in the development of anticancer therapeutics.

Lim, Rhee, Kwon, and co-workers have developed four iridium(III) complexes (**77**) as ER-targeting photosensitizers.[141] Among these complexes, complexes **77c** and **77d** display higher ROS photosensitization efficiencies (Φ_Δ = 0.95 and 0.78, respectively) due to their well-matched triplet-state energy levels, resulting in high photocytotoxicity toward MCF-7 and human ovarian adenocarcinoma SK-OV-3 cells even under low-power light irradiation (1 J cm^{-2}). Characterization of the modes of action of the complexes using mass spectrometry reveals that the photogenerated $O_2^{\bullet-}$ and $^1O_2$ crosslink and oxidize, respectively, important proteins at both the ER and mitochondria (e.g., TRAP1 and PYCR1), leading to rapid cancer cell death. Nevertheless, the high dark cytotoxicity of the complexes remains a concern. Thus, a biocompatible and redox-sensitive nanogel has been utilized to achieve spatiotemporal control over the release of complex **77c** in cancer cells.[142] The nanogel is synthesized by self-crosslinking of a hyperbranched, disulfide-containing polyglycerol-based polymer through intra- and intermolecular thiol–disulfide exchange reactions, and during this process, the iridium(III) complex is encapsulated into the nanogel through hydrophobic interaction with the pyrene units on the polymer chain. Owing to the fully crosslinked amphiphilic micellar structure of the nanogel, the iridium(III) complex is stably embedded in the hydrophobic core of the nanogel, resulting in negligible release even in the presence of high concentrations of GSH that reduce the disulfide bonds into multiple free thiols. As a result, the nanogel encapsulation effectively reduces the dark cytotoxicity of the iridium(III) complex toward HeLa cells, with IC_{50} values increasing from 6.43–9.21 μM to > 16 μM. However, upon irradiation, the iridium(III) complex generates a substantial amount of ROS, leading to the irreversible conversion of the reduced thiols into their hyperoxidized sulfonic acid derivatives. This modification significantly disrupts the nanogel structure and promotes the rapid release of the iridium(III) complex, resulting in high photocytotoxic activity ($IC_{50,light}$ = 3.96 μM) that is comparable to the unencapsulated complex ($IC_{50,light}$ = 3.42 μM). Thus, the iridium(III)-containing nanogel **NG@77c** exhibits high biocompatibility in vivo and induces substantial tumor growth inhibition upon irradiation.

Liu, Jin, Chao, and co-workers have developed three lipophilic cyclometalated iridium(III) terpyridine complexes (**78**) as ER-targeting photosensitizers for PDT.[143] Increasing the π-conjugation of the cyclometalating ligand of the complexes leads to an increase in their $^1O_2$ generation efficiencies and thus photocytotoxic activity. These complexes show efficient cellular uptake and specific localization in the ER of the cells. Upon irradiation, the complexes produce $^1O_2$ and induce ER stress along with the efflux of Ca^{2+} from the ER to the cytosol, resulting in rapid and efficient induction of apoptosis.

4.5. Dual Organelle-Targeted PDT

Since different organelles possess their respective functions in cells, the development of photosensitizers that can target and attack multiple subcellular organelles would lead to synergistic disruption of cellular processes, producing superior therapeutic effects compared to those targeting a single organelle.

Chao and co-workers have developed a series of ruthenium(II) complexes (**79**) that can target both the cytomembrane and mitochondria of cancer cells.[144] All the complexes display large TPA cross-sections ($\delta_{825\ nm}$ = 163.31–190.11 GM) and high $^1O_2$ generation efficiencies (Φ_Δ = 0.53–0.59). As revealed by LSCM, these complexes accumulate on the plasma membrane of HeLa cells within 30 min of incubation and in both the cell membrane and mitochondria after 4 h. The simultaneous presence of the complexes allow the photogenerated $^1O_2$ to induce extensive cellular damage to both organelles, resulting in more significant cell death upon irradiation than when the complexes are exclusively enriched in the cytomembrane. The complexes also exhibit effective tumor penetration in 3D HeLa MCTSs and substantial inhibition of their growth upon two-photon excitation ($IC_{50,light}$ = 0.52–1.04 μM). Remarkably, complex **79d** induces significant tumor regression (TIR = 90.5%) in HeLa tumor-bearing mice upon irradiation without causing significant damage to the normal organs.

Yu, Mao, Liu, and co-workers have designed an iridium(III) complex integrated with a cationic benzothiazolium moiety (**80**) to realize cascade photosensitization in the mitochondria and nucleoli.[145] The introduction of a benzothiazolium pendant enhances the interaction of the complex with DNA and RNA, endowing the complex with nucleus-targeting potential. After cellular internalization, the complex accumulates in the mitochondria and causes oxidative damage upon irradiation through the production of HO$^\bullet$ and $^1O_2$. This process leads to a significant reduction in MMP, enabling the complex to migrate from the mitochondria to the nucleoli and to cause photodamage to nucleic acids. The light-driven mitochondria-to-nucleoli translocation allows the complex to induce more significant cancer cell ablation than the analog bearing a neutral benzothiazole unit, which is enriched in the mitochondria and does not migrate to the nucleus after irradiation.

Zhang, Chao, and co-workers have designed ruthenium(II) complexes modified with a morpholine moiety (**81**) for inducing stepwise lysosomes-to-mitochondria photodamage.[146] All the complexes are essentially non-cytotoxic toward A549 cells in the dark ($IC_{50,dark}$ > 100 μM); however, upon irradiation, the cytotoxicity of the complexes significantly increases, with complex **81d** showing the most potent photocytotoxic activity ($IC_{50,light}$ = 0.4 μM) due to its most efficient cellular uptake and $^1O_2$ generation. Studies on the mechanism of action show that the complexes are enriched in the lysosomes after cellular uptake, attributed to the protonation of the morpholine unit that facilitates the retention of the attached complexes inside this acidic organelle. Upon irradiation, the photogenerated $^1O_2$ induces lysosomal damage and the complex undergoes rapid translocation from the lysosomes to the mitochondria, inducing stepwise damage to these organelles and thus significant cancer cell death.

4.6. Discussion

Each organelle in a cell possesses distinct functions and plays specific roles in maintaining cellular homeostasis. The selective targeting of photosensitizers to specific organelles in cancer cells allows for the effective disruption of vital cellular processes, triggering cancer cell death. Among the various organelles, the nucleus, mitochondria, lysosomes, and ER are considered the most predominant targets for PDT due to their important roles and functions in cellular homeostasis. However, most of the transition metal complexes developed to date preferentially accumulate in the mitochondria due to their cationic charge and lipophilicity, or primarily localize in the lysosomes as a result of their cellular internalization via an endocytic pathway. While these are important organelles, it is crucial to develop new targeting strategies to direct transition metal complexes to the nucleus and ER, which also play significant roles in cellular processes and cell death. To facilitate their transport to these organelles, transition metal complexes can be conjugated with an NLS[147] that binds to nuclear transport receptors on the nuclear envelope, or modified with an ER-targeting group such as *p*-toluenesulfonamide[148] and KDEL peptide[149] that bind to specific receptors on the ER membrane. In addition to the aforementioned organelles, other subcellular organelles such as the plasma membrane,[150] Golgi apparatus,[151] and lipid droplets[152] have emerged as potential therapeutic targets for cancer treatment. Therefore, it is imperative to develop new targeting strategies for these organelles to expand the scope of PDT and enhance its effectiveness in treating cancer. Furthermore, the design of photosensitizers that can simultaneously or sequentially target multiple subcellular organelles is expected to result in synergistic disruption of cellular processes, producing superior therapeutic effects compared to those targeting a single organelle. However, the development of photosensitizers with dual- or multi-organelle-targeting capabilities could be a challenging task. An alternative approach involves the combined use of photosensitizers with distinct organelle specificity, which has been demonstrated to produce enhanced therapeutic effects.[153]

5. Transition Metal Complexes for Cancer-Targeted PDT

Although the use of light in PDT allows controlled activation of the photosensitizers for ROS generation, conventional photosensitizers lack the ability to specifically recognize cancer cells. This non-selective distribution leads to their inadequate accumulation at the tumor site and increases the risk of photodamage to adjacent organs. Thus, various strategies have been developed for selective targeting of photosensitizers to cancer cells to enhance the safety and efficacy of PDT.

5.1. Passive Targeting

Passive targeting takes advantage of the structural and functional differences between tumor and normal vasculature to deliver therapeutic agents to the tumor site.[154] The discontinuous arrangement of vascular endothelial cells and the defective lymphatic drainage at the tumor site often facilitate the penetration and retention of macromolecules and nanoparticles into tumor tissues. This enhanced permeability and retention (EPR) effect has been exploited in the development of tumor-targeting nanomedicines for cancer treatment; examples include Doxil[155] and Abraxane,[156] where the anticancer drugs doxorubicin (DOX) and paclitaxel (PTX) are loaded into PEGylated liposomes and

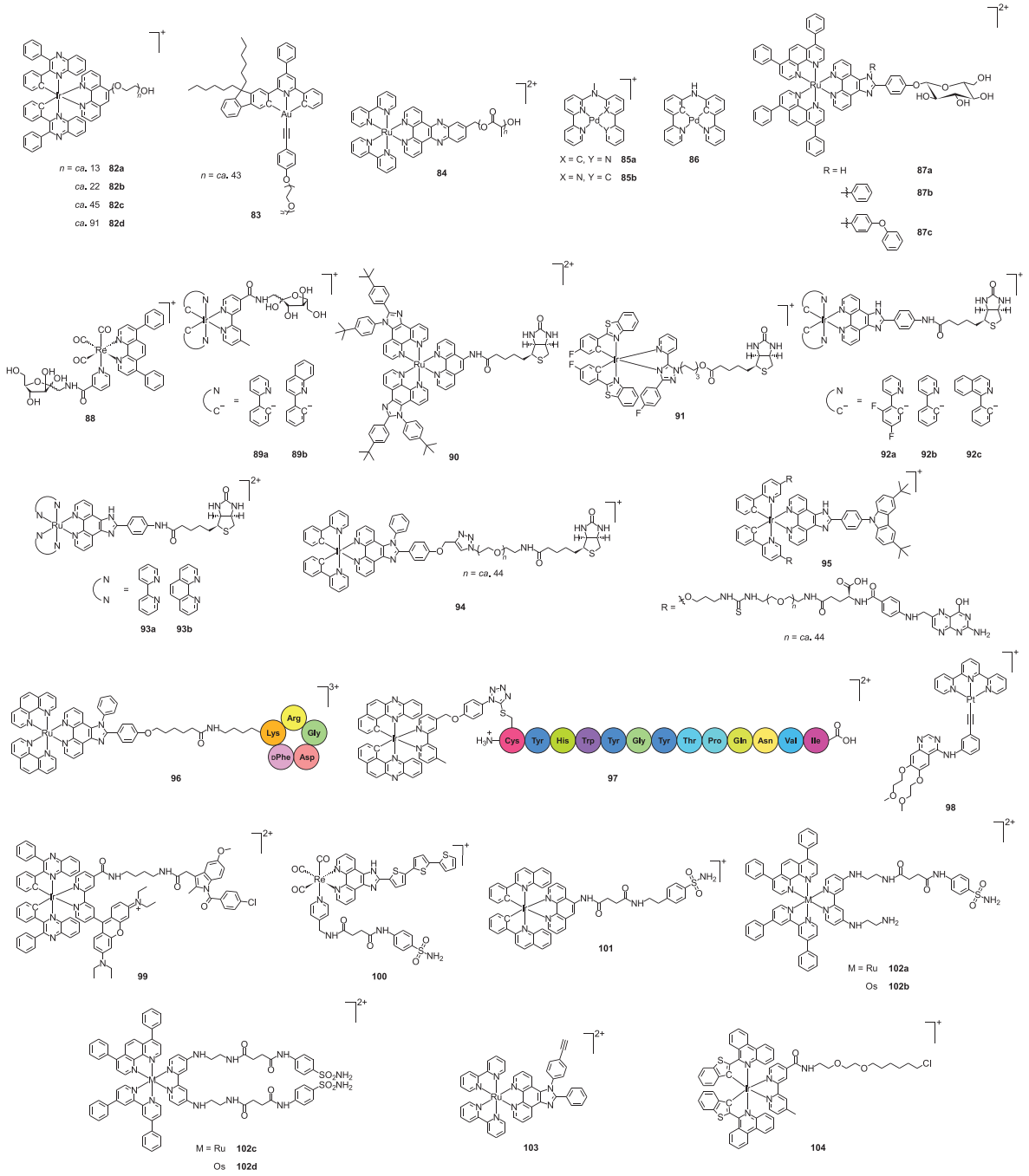

Figure 8. Structures of transition metal complexes (**82**–**104**) for cancer-targeted PDT.

albumin-bound nanoparticles, respectively, to facilitate their extravasation and accumulation in solid tumors.

Sun, Li, and co-workers have designed a series of amphiphilic iridium(III) PEG complexes (**82**) (**Figure 8**) that can self-assemble into nanosized micelles (**82 NPs**) for selective tumor imaging and PDT.[157] The size of the micelles decreases from 76 to 34 nm upon increasing the length of the PEG pendant from 600 to 4000 Da, and thus **82c NPs** and **82d NPs** display the highest micellar stability across the series. Notably, the introduction of a long PEG chain is critical to reducing the non-specific interactions of the micelles with proteins, which in turn prolongs their blood circulation time and promotes their tumor accumulation in vivo due to the EPR effect. Additionally, **82c NPs** and **82d NPs** exhibit efficient cellular uptake and accumulation in cancer cells with low dark cytotoxicity. However, the cytotoxic activity of the micelles substantially increases upon irradiation due to $^1O_2$ generation, with **82c NPs** showing higher photocytotoxicity due to higher cellular uptake. Che and co-workers have also developed a macromolecular gold(III) PEG complex (**83**).[158] This amphiphilic complex self-assembles into nanosized micelles

(size = ca. 160 nm) with a long emission lifetime of 84 µs in aqueous solutions, which enables efficient photosensitization of $^1O_2$. Thus, the complex displays low dark cytotoxicity, high photocytotoxic activity, and selective tumor accumulation in vivo, favoring its application in tumor-specific imaging and PDT.

Gasser, Thomas, and co-workers have utilized a drug-initiated ring-opening polymerization approach to convert a cell-impermeable ruthenium(II) complex into a cell-permeable ruthenium(II)-containing polymer (**84**) for PDT.[159] The precursor complex features a hydroxyl group, which allows for its covalent incorporation into the polymer chain during ruthenium-initiated ring-opening polymerization of lactide. The resultant metallopolymer is then formulated into nanoparticles using a nanoprecipitation method. Compared to the monomeric precursor complex, the nanoparticles exhibit enhanced emission intensities and $^1O_2$ generation efficiencies due to effective shielding of the phenazine nitrogen atoms from water molecules. Importantly, the nanoparticles show substantially enhanced cellular uptake and retention, resulting in higher photocytotoxicity upon irradiation. Pharmacokinetics and biodistribution studies of a related ruthenium(II)-containing polymer in tumor-bearing mice reveal that polymer encapsulation promotes the tumor accumulation of the complex while reducing non-specific accumulation in vital organs such as the brain and lungs.[160] These observations highlight that the incorporation of transition metal complexes into polymers is an effective approach to increase their tumor uptake and accumulation.

Sun, Bonnet, and co-workers have leveraged the self-assembly behavior of square-planar cyclometalated palladium(II) complexes (**85**) to enhance their tumor uptake for PDT.[161] These complexes self-assemble into supramolecular nanorods in aqueous solutions via Pd···Pd and π–π interactions. The nanorods are stabilized in the cell medium by serum proteins and internalized into cells via endocytosis. Notably, the cellular uptake of these complexes is higher than their dicationic tetrapyridyl counterpart, which exclusively exists as monomeric species due to the strong intermolecular electrostatic repulsion and enters cells through passive diffusion. Additionally, the position of the Pd–C bond has a strong impact on the HOMO, which is centered on the non-coordinated amine bridge of the tetradentate ligand. The close proximity between the electron-rich metalated phenyl ring and the amine bridge of the ligand leads to a larger HOMO–LUMO energy gap; thus, complex **85a** displays stronger absorption in the range of 400–500 nm ($\varepsilon_{455\ nm}$ = 1500 M^{-1} cm^{-1}) than complex **85b** and its tetrapyridyl counterpart ($\varepsilon_{455\ nm}$ = 37 and 56 M^{-1} cm^{-1}, respectively). The enhanced blue-light absorption of complex **85a** allows efficient $^1O_2$ generation in both its monomeric and aggregated forms (Φ_Δ = 0.78 and 0.73, respectively) upon irradiation with blue light, inducing significant cancer cell death in vitro and in vivo. A related biscyclometalated palladium(II) complex (**86**) has also been developed for PDT.[162] The self-assembly of the complex into nanoparticles is accompanied by the emergence of a new absorption band at 504 nm and emission band at 610–670 nm, originating from the metal–metal-to-ligand charge-transfer (MMLCT) state where Pd···Pd interaction plays a key role. Notably, the complex efficiently sensitizes the production of $O_2^{\bullet-}$ but not $^1O_2$ in both the monomeric and aggregated states (Φ_Δ = 0.09 and 0.04, respectively) upon green-light irradiation, resulting in high photocytotoxicity toward hypoxic A375 cells and MCTSs ($IC_{50,light}$ = 0.49 and 0.20 µM, respectively). Biodistribution studies show that the complex, which self-assembles into supramolecular nanostructures upon intravenous injection and remains self-assembled during circulation, exhibits long blood circulation time (>12 h) and efficient tumor accumulation (up to 10.2% ID g^{-1}) in A375 tumor-bearing mice due to the EPR effect, enabling efficient tumor destruction upon green-light irradiation.

5.2. Active Targeting

Active targeting leverages the pathophysiological difference in the expression of receptors and antigens between tumor and normal cells to achieve tumor accumulation.[163] This tumor-targeting approach involves the modification of drug molecules or drug carriers with a biomolecule (e.g., sugars, vitamins, peptides, antibodies, and aptamers) that can bind to specific receptors overexpressed on the surface of cancer cells or tumor-associated endothelial cells to achieve precise tumor targeting. A representative example of active targeting is antibody–drug conjugates (ADCs), where cytotoxic payloads are conjugated to monoclonal antibodies for accurate and efficient elimination of cancer cells.[164] To date, there are 13 approved ADCs available worldwide for cancer treatment and over 100 ADCs are being investigated in clinical trials, demonstrating the promising and effective nature of active targeting strategies in tumor targeting.

5.2.1. Glucose Transporters

Glucose plays a crucial role in cellular metabolism and serves as an essential energy source for supporting cell growth.[165] The transport of glucose across the plasma membrane of cells is mediated by the membrane-bound glucose transporters (GLUTs).[166] The elevated glucose uptake and metabolism in cancer cells is associated with the upregulation of GLUT expression.[167]

Chao and co-workers have developed luminescent ruthenium(II) complexes modified with a D-glucose moiety (**87**) for cancer-specific two-photon-induced PDT.[168] The complexes are internalized into cells via a GLUT-mediated pathway, leading to a higher level of accumulation in cancer cells (A549, A549/DDP, HeLa, and HepG2) over normal cells (LO2). Additionally, the complexes specifically accumulate in the mitochondria after cellular uptake. The dual specific targeting of cancer cells and their mitochondria results in selective photocytotoxic activity toward cancer cells ($IC_{50,light}$ = 2.1–14.2 µM) over normal cells ($IC_{50,light}$ = 20.4–25.2 µM). The strong TPA ($\delta_{810\ nm}$ = 128 GM), high $^1O_2$ photosensitization efficiency (Φ_Δ = 0.85), and excellent cancer selectivity and mitochondria specificity enable complex **87a** to achieve complete tumor ablation in HeLa tumor-bearing mice upon two-photon excitation (810 nm).

The substrates of GLUTs are not limited to glucose; for example, GLUT5 shows preferential uptake of fructose.[169] The expression of GLUT5 is upregulated in breast cancer tissues while its presence is limited in other cancer cells and normal breast

tissues.[170] Lo and co-workers have designed a luminescent rhenium(I) complex appended with a D-fructose pendant (**88**) for PDT of breast cancer.[171] The cellular uptake of this fructose complex is mediated by fructose transporters but independent of glucose-specific transporters. Thus, the complex displays more efficient uptake in breast cancer cells (MCF-7 and MDA-MB-231) over non-breast cancer (A549 and HepG2) and non-cancerous cells (human embryonic kidney HEK293T and mouse embryonic fibroblast NIH/3T3). Consequently, complex **88** exhibits higher dark cytotoxicity toward breast cancer cells (MCF-7 and MDA-MB-231; $IC_{50,dark}$ = 9.6 and 4.9 μM) than non-breast cancer cells (A549 and HepG2; $IC_{50,dark}$ = 26.8 and 33.9 μM), and its cytotoxic activity toward MCF-7 cells is further enhanced upon irradiation ($IC_{50,light}$ = 2.0 μM) due to efficient $^1O_2$ generation. Related iridium(III) D-fructose complexes (**89**) also exhibit selective uptake in MCF-7 cells over HEK293T cells.[172] These complexes are essentially non-cytotoxic toward MCF-7 cells in the absence of light ($IC_{50,dark}$ > 498.4 and 128.4 μM), but display high photocytotoxicity ($IC_{50,light}$ = 5.0 and 11.2 μM) as a result of the generation of $^1O_2$ upon irradiation.

5.2.2. Biotin Receptors

Biotin (vitamin B_7) is an essential nutrient that plays a crucial role in the metabolism of glucose, amino acids, and fatty acids, which are important to cell growth, proliferation, and differentiation.[173] In cancer cells, biotin receptors (BRs), in particular sodium-dependent multivitamin transporters, are often overexpressed on the plasma membrane for acquiring biotin to support their rapid proliferation.[174] Thus, biotin conjugation has been developed as a versatile approach for cancer-targeted imaging and therapy.

Chen, Chao, and co-workers have designed a luminescent ruthenium(II) complex modified with a biotin moiety (**90**) for tumor-targeted two-photon-induced PDT.[175] This complex exhibits strong TPA ($\delta_{820\,nm}$ = 140.26 GM) and efficient $^1O_2$ photosensitization (Φ_Δ = 0.87). Remarkably, biotinylation promotes the cellular internalization of the complex via a BR-mediated pathway, leading to higher accumulation in A549/DDP cells (BR-positive) compared to human lymphatic fibroblast HLF-a cells (BR-negative). Upon two-photon excitation (820 nm), the complex produces $^1O_2$ and activates caspase-3/7, resulting in cell apoptosis. As a result, the complex shows higher photocytotoxic activity toward A549/DDP cells ($IC_{50,light}$ = 3.3 μM) than non-cancerous HLF-a cells ($IC_{50,light}$ = 36.4 μM), and this cancer-selective photocytotoxicity is also observed in 3D multicellular spheroids. Tian and co-workers have developed a luminescent iridium(III) biotin complex with multiphoton absorption properties (**91**) for image-guided PDT.[176] The good two-photon ($\delta_{775\,nm}$ = 19.36 GM) and three-photon absorption ($\sigma_{1200\,nm}$ = 18.5 × 10^{-82} cm^6 s^2 $photon^{-2}$) of the complex in the NIR region enable the photosensitization of $^1O_2$ with multiphoton excitation. The complex displays preferential uptake and accumulation in BR-overexpressing HeLa cells over normal human hepatocyte QSG-7701 cells, efficiently inducing cancer cell apoptosis upon irradiation. In vivo imaging shows that the tumor accumulation of the complex reaches the maximum 3 h after intratumoral injection. Subsequent exposure of the tumor region to irradiation with an NIR laser (760 nm, 120 J cm^{-2}) leads to significant tumor regression with a TIR of 87.66%.

Shao, Wang, and co-workers have developed three luminescent iridium(III) biotin complexes (**92**) as mitochondria-targeting theranostic agents for tumor-targeted imaging and PDT.[177] The preferential uptake and accumulation of these complexes in cancer cells and mitochondria allow the complexes to induce cancer cell apoptosis through causing mitochondrial dysfunction upon irradiation, resulting in selective photocytotoxic activity toward cancer cells (A549, MCF-7, and MDA-MB-231; $IC_{50,light}$ = 0.24–1.58 μM) over normal cells (baby hamster kidney (BHK); $IC_{50,light}$ = 5.60–7.50 μM) and thus significant tumor regression in vivo without causing systemic toxicity. Related ruthenium(II) biotin complexes (**93**) have also been developed for tumor-targeted PDT.[178] These complexes are AIE-active and exhibit high emission intensities and $^1O_2$ generation efficiencies in aqueous solutions. Additionally, the complexes can induce NADH oxidation and DNA cleavage upon irradiation. As revealed by LSCM, upon selective uptake and accumulation in BR-overexpressing cancer cells, the complexes are enriched in the mitochondria. Upon irradiation, the complexes induce ROS generation and NADH depletion, triggering a cascade of events including MMP reduction, caspase-3 activation, DNA damage, cell cycle arrest, and apoptosis induction. The induction of apoptotic cell death in cancer cells leads to effective inhibition of tumor growth in A549 tumor-bearing mice. Shao, Wang, and co-workers have also developed a related luminescent iridium(III) biotin complex (**94**) for bioimaging and tumor-targeted PDT.[179] The introduction of a PEG linker between the iridium(III) core and the biotin unit promotes the self-assembly of the complex into micellar nanoparticles. Similar to other biotin complexes, the resulting nanoparticles (**94 NPs**) show higher cellular uptake in BR-positive cancer cells (A549 and MDA-MB-231) compared to BR-negative normal cells (BHK and LO2), with specific accumulation in the mitochondria. Upon irradiation, the nanoparticles disrupt intracellular redox homeostasis by generating $^1O_2$ and depleting intracellular NADPH and GSH, which ultimately triggers cancer cell death through a combination of apoptosis and ferroptosis. Furthermore, the nanoparticles efficiently accumulate at the tumor site in A549 tumor-bearing mice following tail vein injection due to both the EPR effect and active targeting of BRs overexpressed on cancer cells, resulting in significant tumor regression upon irradiation.

5.2.3. Folate Receptors

Folic acid (vitamin B_9) is involved in de novo nucleotide synthesis and one-carbon metabolism, which are crucial for the production of DNA/RNA and amino acids for cell survival and proliferation.[180] The cellular uptake of folic acid is mediated by FRs, a group of membrane-bound glycoproteins that display high affinity for folic acid.[181] Notably, the isoform FRα is overexpressed in various types of cancer cells but not in normal tissues.[182] Thus, FRα has been recognized as an important cancer biomarker for cancer-targeted imaging and drug delivery.[183]

Shao, Wang, and co-workers have developed an iridium(III) complex functionalized with a folic acid moiety (**95**) for

tumor-targeted PDT.[184] This complex can self-assemble into uniform nanoparticles in aqueous solutions due to the PEG pendant, which facilitates its tumor accumulation via both the EPR effect and FR targeting. The complex is efficiently internalized into FR-positive HeLa cells via a FR-mediated endocytic pathway and specifically enriched in the mitochondria. In contrast, the cellular uptake of the complex in FR-negative A549 cells is negligible. In vivo biodistribution studies reveal that upon tail vein injection, the complex exhibits more efficient tumor accumulation in HeLa tumor-bearing mice than in A549 tumor-bearing mice with a higher tumor-to-liver signal ratio due to the synergistic effect of both passive and active targeting. Remarkably, the complex shows very high efficiency in generating $^1O_2$ ($\Phi_\Delta = 0.97$) upon irradiation, which leads to GSH and GPX4 depletion as well as LPO accumulation. The efficient induction of apoptotic and ferroptotic cell death results in effective suppression of tumor growth in vivo (TIR = 71.9%).

5.2.4. Integrins

Integrins are a class of heterodimeric transmembrane glycoproteins composed of an α-subunit and a β-subunit.[185] These pivotal proteins serve as cell adhesion receptors, mediating cell–cell and cell–extracellular matrix (ECM) adhesion that regulate essential cellular functions such as migration, proliferation, and apoptosis. Among the integrin family, integrin $\alpha_v\beta_3$ is frequently overexpressed in cancer cells, playing a significant role in promoting tumor growth, invasion, and metastasis.[186] Thus, integrin $\alpha_v\beta_3$ has emerged as an important target for cancer therapy.

Wang and co-workers have developed a ruthenium(II) complex conjugated with a cyclic RGD peptide (**96**) for two-photon-induced PDT of tumor cells.[187] The RGD peptide is a cell adhesion sequence that binds to integrin $\alpha_v\beta_3$ with high affinity; thus, the peptide conjugation facilitates the binding of the complex to integrin $\alpha_v\beta_3$ and promotes its cellular internalization via an integrin $\alpha_v\beta_3$-mediated pathway, leading to an increased uptake of the complex in human glioblastoma U-87 MG cells ($\alpha_v\beta_3$-positive) over MCF-7 cells ($\alpha_v\beta_3$-negative). Furthermore, the complex specifically accumulates in the mitochondria of U-87 MG cells and triggers mitochondria-mediated apoptosis upon irradiation, resulting in high photocytotoxicity toward U-87MG cells and MCTSs. Remarkably, the complex significantly inhibits tumor growth in U-87 MG tumor-bearing mice upon two-photon-excitation (820 nm) with a TIR of 87%, which is significantly higher than its peptide-free counterpart (15%) due to enhanced tumor accumulation.

5.2.5. Epidermal Growth Factor Receptor

The epidermal growth factor receptor (EGFR) is a transmembrane glycoprotein that belongs to the ErbB family of receptor tyrosine kinases and is involved in various important signaling pathways associated with cell differentiation and proliferation.[188] The overexpression of EGFR in cancer cells is implicated in tumor progression, metastasis, resistance to therapies, and poor prognosis.[189] Various EGFR-targeting monoclonal antibodies (e.g., cetuximab and panitumumab) and tyrosine kinase inhibitors (e.g., erlotinib, gefitinib, and lapatinib) are now in clinical use for the treatment of various types of cancer.

Lam, Lo, and co-workers have conjugated an NIR luminescent iridium(III)-based photosensitizer with the dodecapeptide GE11, which binds to EGFR with high affinity and selectivity, for cancer-selective imaging and PDT.[190] The resultant peptide conjugate (**97**) selectively accumulates in the plasma membrane of cancer cells (A431 and MDA-MB-231) but not in non-cancerous cells (HEK293T) due to its specific binding to the EGFRs overexpressed on the surface of cancer cells. The differential cellular uptake leads to substantially higher photocytotoxic activity toward A431 and MDA-MB-231 cells ($IC_{50,light}$ = 0.49 and 1.01 μM, respectively) compared to HEK293T cells ($IC_{50,light}$ = 10.09 μM). Karges, Zhang, Huang, and co-workers have designed a platinum(II) complex functionalized with an erlotinib unit (**98**) for EGFR-targeted PDT.[191] This complex exists as a monomer and displays weak emission in organic solvents; however, in aqueous solutions, it self-assembles into supramolecular nanostructures that exhibit intense and long-lived deep-red luminescence and efficient $^1O_2$ generation. Encapsulation of the complex into DSPE-PEG affords luminescent nanoparticles (**PM@98**) that show a higher level of cellular accumulation and photocytotoxicity in EGFR-overexpressing cancer cells (A431, A549, and its cisplatin-resistant (A549/DDP) and taxol-resistant (A549/Tax) derivative; $IC_{50,light}$ = 1.28–5.17 μM) over MRC-5 cells with normal EGFR expression ($IC_{50,light}$ > 320 μM). Mechanistic studies indicate that the nanoparticles induce EGFR degradation via the lysosomal degradation pathway upon irradiation.

5.2.6. Cyclooxygenases

Cyclooxygenases (COXs) are membrane-bound, heme-containing peroxidases responsible for catalyzing the conversion of arachidonic acid to prostaglandins, which play a key role in mediating inflammatory response.[192] Of particular significance is the inducible isoform COX-2, which is overexpressed in inflamed and neoplastic tissues while maintaining low expression in normal tissues.[193] The distinct expression profiles of COX-2 render it a promising molecular target for both the prevention and treatment of cancer.

Liu and co-workers have developed an iridium(III)–rhodamine dyad bearing an indomethacin moiety (**99**) for COX-2-targeted PDT.[194] The incorporation of indomethacin, a COX-2 inhibitor, into the complex enhances its affinity for COX-2, thereby promoting its cellular uptake in cancer cells (HeLa and MCF-7) over non-cancerous cells (HEK293T and LO2). The increased cancer selectivity of the complex enhances its tumor accumulation in vivo, enabling a substantial reduction in the tumor size from ca. 1000 to 200 mm^3 in MCF-7 tumor-bearing mice upon irradiation.

5.2.7. Carbonic Anhydrases

Carbonic anhydrases (CAs) are a family of metalloenzymes that catalyze the reversible hydration of carbon dioxide to bicarbonate and protons.[195] Among these enzymes, the hypoxia-inducible, membrane-bound isoforms CA-IX and CA-XII are overexpressed

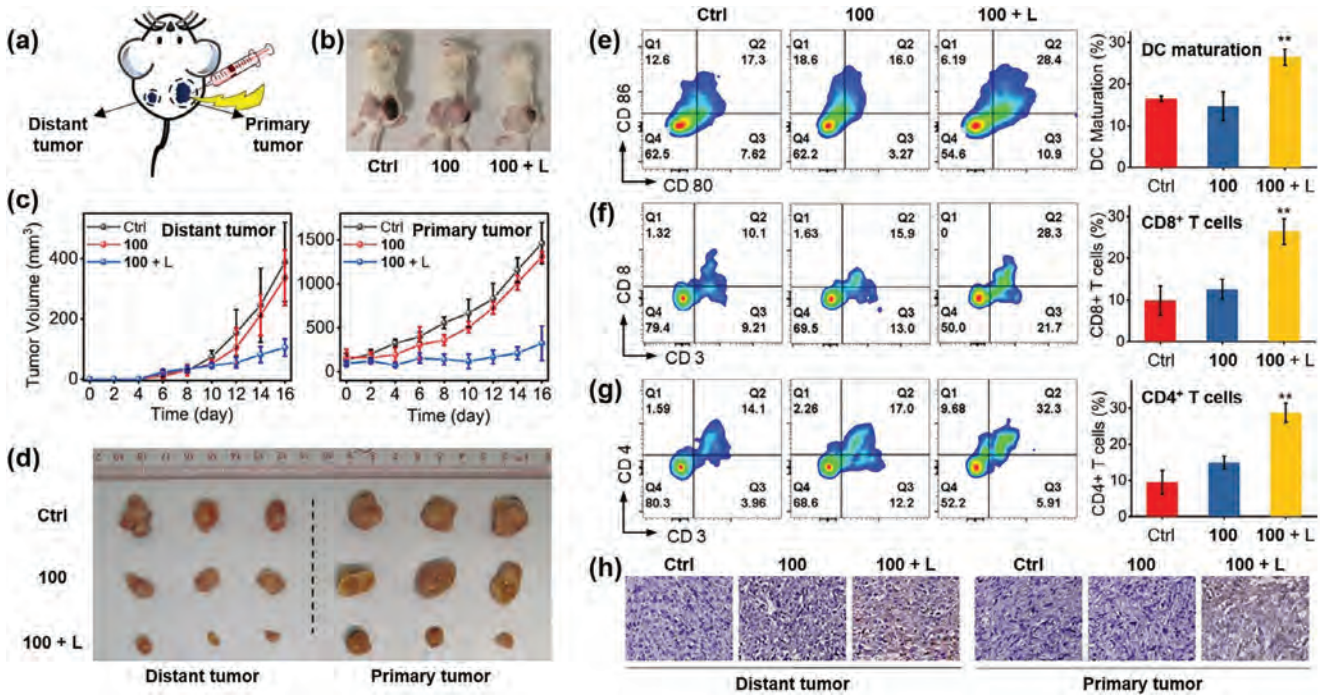

Figure 9. a) In vivo therapeutic protocol using a bilateral model. b) Representative photographs of bilateral 4T1 tumor-bearing mice after different treatments. c) Tumor growth curves of primary and distant tumors in bilateral 4T1 tumor-bearing mice under different treatments. d) Representative photographs of tumors dissected from bilateral 4T1 tumor-bearing mice after different treatments. e–g) Flow cytometric analysis of the populations of e) mature DCs, f) $CD8^+$ T cells, and g) $CD4^+$ T cells in distant tumors of bilateral 4T1 tumor-bearing mice after different treatments ($n = 3$). $^*p < 0.05$, $^{**}p < 0.01$, and $^{***}p < 0.001$. h) Immunohistochemistry analysis of tumor-infiltrating $CD8^+$ T cells in primary and distant tumor tissues harvested from bilateral 4T1 tumor-bearing mice after different treatments. Ctrl: saline; complex **100**: 5 mg kg^{-1}; L: 525 nm, 15 mW cm^{-2}, 1 h. Adapted with permission.[198] Copyright 2022, Wiley-VCH.

in various solid tumors, playing a crucial role in promoting tumor growth by counteracting acidosis through the regulation of intracellular pH.[196] Thus, the inhibition of tumor-associated CA-IX and CA-XII with specific inhibitors such as benzenesulfonamides can interfere with tumor pH regulation, inhibiting tumor growth and metastasis.[197]

Cao, Mao, and co-workers have designed a rhenium(I) α-oligothiophene complex modified with a benzenesulfonamide unit (**100**) as a CA-IX-targeting photosensitizer.[198] The strong binding of the complex to CA-IX allows its specific accumulation in the plasma membrane of cancer cells, resulting in very high cancer-selective photocytotoxic activity toward breast cancer cells (MDA-MB-231 and 4T1; $IC_{50,light}$ = 7.3–220 nM) compared to normal breast cells (MCF-10A; $IC_{50,light}$ = 0.12–0.39 μM), with PI values > 13700 and > 5000 under normoxia and hypoxia, respectively. Mechanistic studies indicate that the complex induces effective CA-IX inhibition and HIF-1α downregulation, alleviating tumor hypoxia and favoring ROS photosensitization. The photogenerated ROS on the cell membrane induce plasma membrane rupture through lipid peroxidation, triggering gasdermin D (GSDMD)-mediated pyroptosis. The subsequent exposure of damage-associated molecular patterns (DAMPs) on the cell surface stimulates the maturation of DCs and activates T cell-dependent adaptive immune response in vivo, effectively inhibiting the growth of both primary and distant tumors (TIR = 78 and 73%, respectively) in bilateral 4T1 tumor-bearing mice (**Figure 9**). A related iridium(III) benzenesulfonamide complex (**101**) has also been developed as an ICD photoinducer through targeted CA-IX photodegradation.[199] Cariou, Rossel, Gasser, and co-workers have developed ruthenium(II) and osmium(II) complexes modified with one or two benzenesulfonamide moieties (**102**) as photosensitizers for the treatment of hypoxic tumors.[200] The high affinities of the complexes for CAs (K_d = 111.5–151.2 nM for human CA-II) enable their efficient cellular uptake in A549 and MDA-MB-231 cells, leading to high photocytotoxicity under both normoxic and hypoxic conditions.

5.2.8. Sialylated Glycans

Sialic acids are nine-carbon monosaccharides derived from neuraminic acid and are expressed at the termini of the glycan chains of cell-surface glycoproteins and glycolipids.[201] The addition of sialic acid to glycoproteins and glycolipids (i.e., sialyation) is an important post-translational modification involved in embryonic development, neurodevelopment, oncogenesis, and immune response. Aberrant sialylation is a hallmark of various types of cancer and is associated with cancer progression, invasion, metastasis, and immune evasion.[202]

Chao and co-workers have utilized a two-step approach combining metabolic glycoengineering and bioorthogonal labeling to achieve precise targeting of a ruthenium(II)-based photosensitizer (**103**) to TNBC, which lacks intrinsic targetable receptors.[203] In this approach, an unnatural azide-modified

sialic acid precursor 1,3,4,6-tetra-*O*-acetyl-*N*-azidoacetyl-D-mannosamine (Ac_4ManNAz) is incorporated into cell-surface glycans by hijacking the sialic acid biosynthetic pathway. Subsequent reaction of the membrane-bound azide units with the alkyne-functionalized complex allows for the in situ generation and immobilization of a triazole derivative that shows large TPA ($\delta_{810\,nm}$ = 212 GM) and efficient $^1O_2$ photosensitization (Φ_Δ = 0.80) on the plasma membrane for two-photon-induced PDT. Thus, the complex displays negligible cytotoxic activity toward MDA-MB-231 cells under both dark and light conditions (IC_{50} > 40 μM), but exhibits high photocytotoxicity ($IC_{50,light}$ = 10.6 μM) when the cells are pretreated with Ac_4ManNAz, as the photogenerated ROS cause significant membrane disruption and induce cell death. The high photocytotoxic activity of the complex is retained in Ac_4ManNAz-pretreated MDA-MB-231 MCTSs. Notably, the complex is essentially non-(photo)cytotoxic toward both Ac_4ManNAz-pretreated and untreated non-cancerous MCF-10A cells (IC_{50} > 40 μM), suggesting that metabolic glycoengineering is an effective means to generate artificial receptors for cancer-specific imaging and treatment.

5.3. Anaerobic Bacteria

Anaerobic bacteria have recently emerged as promising carriers for targeted drug delivery to tumors.[204] Owing to their intrinsic hypoxia tropism and self-propelled motility, these bacteria can navigate along the O_2 gradients toward the hypoxic TME, facilitating them to target, penetrate, and colonize in solid tumors. Through the use of genetic engineering techniques, these bacteria can be modified and exploited as tumor-targeting vehicles for delivering therapeutic agents into the TME.

Shen, Mao, Xia, and co-workers have utilized engineered *Escherichia coli* NISSLE 1917 (EcN) for targeted delivery of an iridium(III)-based photosensitizer to tumor cells for photodynamic immunotherapy.[205] This probiotic strain is genetically modified to express the HaloTag protein, a self-labeling protein derived from the haloalkane dehalogenase, on its outer membrane for covalent labeling with an iridium(III) complex bearing a chloroalkane pendant (**104**) through an enzymatic ligation reaction. The labeled bacteria (**HaloECN-104**) selectively accumulate and penetrate into tumor tissues and efficiently produce ROS via both Type I ($O_2^{\bullet-}$ and HO$^\bullet$) and Type II pathways ($^1O_2$) upon irradiation. The increased ROS production in cancer cells induces GSDMD-mediated pyroptosis and ICD, evoking both innate and adaptive immune response to inhibit tumor growth in vivo (TIR = 85%).

5.4. Discussion

Passive targeting through the EPR effect and active targeting via specific cell-surface receptors are the two most common strategies used for tumor targeting. Effective delivery of therapeutic agents to tumors requires both passive and active targeting mechanisms to enhance their accumulation at the tumor site and facilitate internalization into cancer cells within the tumor. However, the limited number of targetable endogenous proteins and receptors have restricted the effectiveness of conventional active targeting strategies to certain types of cancer. Furthermore, the heterogeneity within and between tumors poses a significant challenge to achieving precise and effective cancer treatment.[206] To overcome these limitations, the combination of metabolic glycoengineering and bioorthogonal chemistry has provided a promising alternative to increase the precision of tumor targeting.[207] This approach involves the incorporation of bioorthogonal handles into the cell-surface glycans as artificial receptors for cancer targeting via bioorthogonal reactions. The utilization of nanosized[208] or enzyme-responsive[209] metabolic precursors allows selective labeling of cancer cell membrane with bioorthogonal units in a controlled, cancer-specific, and cell phenotype-independent manner, providing a new targeting approach to treat cancers lacking targetable receptors (e.g., TNBC). Furthermore, living cells (e.g., red blood cells, macrophages, stem cells, bacteria, and viruses)[210] and extracellular vesicles (e.g., exosomes)[211] as well as biomimetic nanoparticles (e.g., cell membrane-coated nanoparticles)[212] have emerged as new delivery platforms that can target tumors through a "Trojan Horse" approach. These cell-based materials retain or mimic the characteristic membrane composition of native cells that endow them with immune evasion and tumor homing capabilities, prolonging their blood circulation time and facilitating their tumor accumulation. These new tumor-targeting strategies are expected to advance cancer treatment with PDT.

6. Transition Metal Complexes for Activatable PDT

Traditional photosensitizers used in PDT have intrinsic limitations such as non-selective tissue distribution and uncontrollable ROS generation, leading to off-target photocytotoxicity toward normal tissues such as skin and organs. Since tumor tissues often display distinct features such as low pH, elevated ROS/GSH levels, and aberrant enzyme activity that differentiate them from normal tissues, there has been emerging interest in the design of activatable photosensitizers that exhibit emission and ROS-photosensitization turn-on in response to specific tumor-associated stimuli for cancer-targeted PDT.[213] This on-target activation allows for the discrimination of cancer cells from normal cells, thereby minimizing off-target photodamage and enhancing the precision of PDT.

6.1. pH-Activatable Photosensitizers

Owing to the hypoxic TME, cancer cells mainly rely on glycolysis for energy production, producing a significant amount of lactate and protons.[214] To prevent intracellular acidification, the expression of various pH-regulating proteins on the cancer cell membrane is upregulated to facilitate the efflux of lactate and protons, resulting in a lower extracellular pH (6.5–7.1) compared to normal cells (7.2–7.5). This mild acidity is a hallmark of TME and plays an important role in promoting cancer cell proliferation, migration, and invasion.[215]

Tan, Mao, and co-workers have designed a series of iridium(III) *β*-carboline complexes (**105**) (**Figure 10**) as pH-activatable photosensitizers for lysosome-targeted imaging and PDT.[216] The emission intensities and $^1O_2$ generation efficiencies of the complexes are highly sensitive to the pH of the local

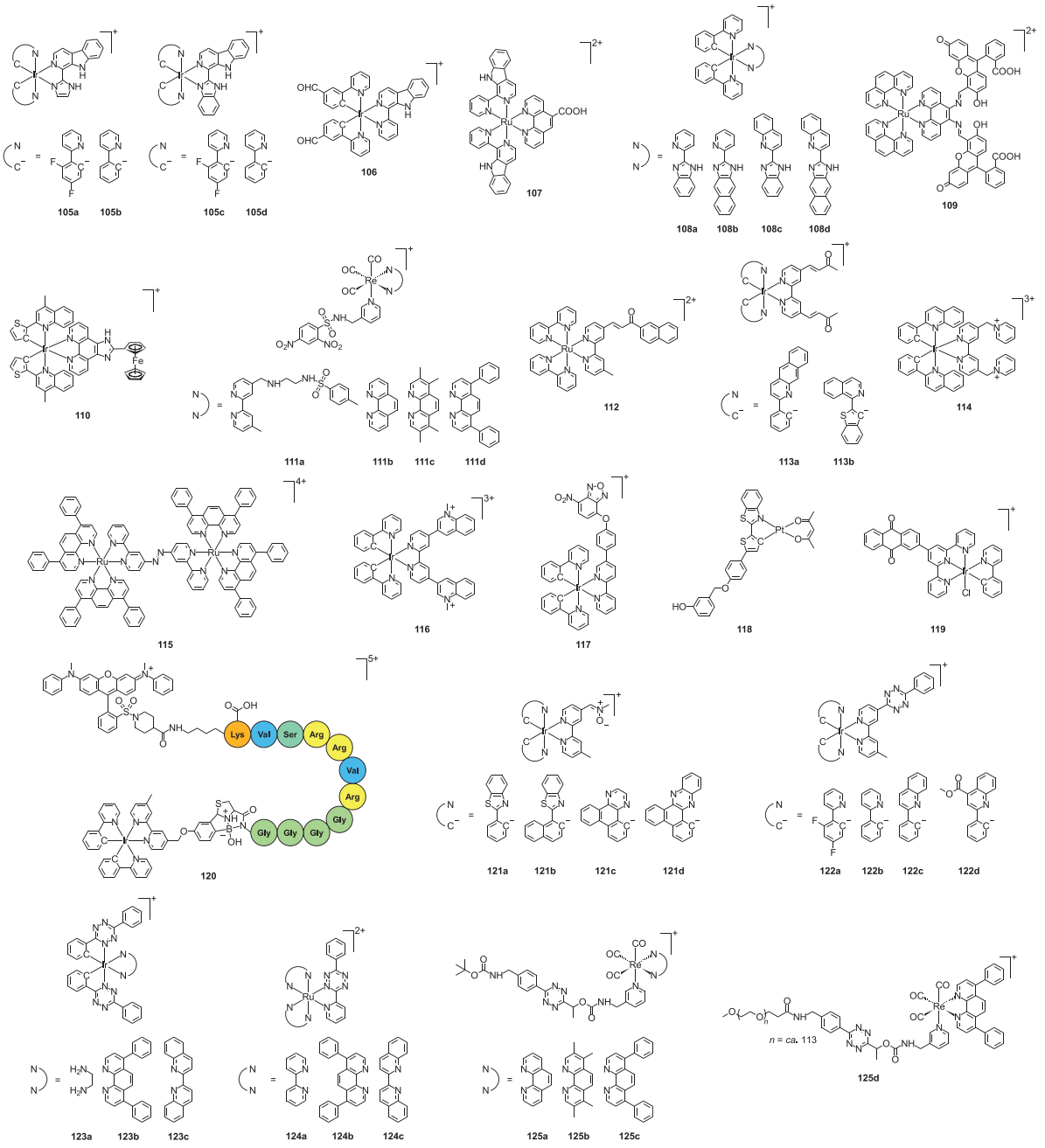

Figure 10. Structures of transition metal complexes for pH (**105–109**), ROS (**110**), GSH (**111–115**), NADH (**116**), H_2S (**117**), enzyme (**118–120**), and bioorthogonally activatable PDT (**121–125**).

environment due to the deprotonation/protonation of the indole ring in the β-carboline ligand. Among these complexes, complex **105d** shows the largest photophysical changes in response to pH; the emission and $^1O_2$ generation quantum yields of this complex increase from 0.019 and 0.05 to 0.092 and 0.51, respectively, upon decreasing the pH from 7.4 to 3.0. Remarkably, complex **105d** is essentially non-cytotoxic in the dark ($IC_{50,dark}$ > 100 μM), but it displays higher photocytotoxic activity toward cancerous A549 and A549/DDP cells ($IC_{50,light}$ = 0.12 and 0.16 μM, respectively) compared to normal LO2 cells ($IC_{50,light}$ = 4.4 μM). Studies on the mode of cell death indicate that the complex specifically accumulates in the lysosomes and induces apoptosis through causing lysosomal damage and cathepsin B release upon irradiation. Additionally, the high lysosome specificity of the complex offers opportunities to monitor therapeutic outcomes in situ by real-time tracking changes in lysosomal integrity during the photoinduced cell death. A related iridium(III) pyridyl-β-carboline complex (**106**) also exhibits enhanced emission and $^1O_2$ generation under acidic conditions, enabling selective killing of cancerous HeLa cells ($IC_{50,light}$ = 3.8 μM) over non-cancerous MRC-5

cells ($IC_{50,light}$ = 50.7 μM) upon irradiation.[217] Tan, Mao, and co-workers have conjugated a ruthenium(II) β-carboline complex (**107**) to Cdots for lysosome-targeted two-photon-induced luminescence imaging and PDT.[218] Compared to the free complex ($\delta_{810\,nm}$ = 171 GM), the nanoconjugate (**Cdot@107**) shows substantially enhanced TPA ($\delta_{810\,nm}$ = 1118 GM) and cellular uptake, allowing more effective inhibition of cancer cell growth in both 2D cells and 3D MCTSs upon two-photon excitation.

Tan, Mao, and co-workers have also developed a series of pH-sensitive iridium(III) benzimidazole complexes (**108**) for lysosome-targeted PDT.[219] These complexes display higher $^1O_2$ photosensitization efficiencies in acidic solutions than in neutral solutions. The efficient generation of $^1O_2$ in the lysosomes leads to lysosomal damage and caspase-mediated apoptosis, resulting in potent photocytotoxicity toward cancer cells (A549, A549/DDP, and HeLa; $IC_{50,light}$ = 0.21–1.43 μM). Additionally, the complexes effectively inhibit several cellular processes associated with tumor progression and metastasis, including cell migration, invasion, colony formation, and angiogenesis. Screening against 70 kinases reveals that maternal embryonic leucine zipper kinase (MELK), phosphoinositide-3-kinase catalytic subunit alpha (PIK3CA), and AMP-activated protein kinase (AMPK) are the possible molecular targets. In vivo studies show that treatment of HeLa tumor-bearing mice with complex **108d** and light results in a 74.5% reduction in the tumor volume.

Elias and co-workers have designed a ruthenium(II) salphen complex containing two fluorescein moieties (**109**) as a pH-activatable photosensitizer for theranostic applications.[220] This complex exhibits efficient cellular uptake and nuclear localization due to the extended aromatic structure of fluorescein which endows the complex with higher affinity toward the genetic material. Notably, the $^1O_2$ photosensitization efficiency of the complex substantially increases from 0.07 to 0.66 upon decreasing the pH from 7.5 to 5.5. As a result, while the complex shows negligible cytotoxic activity toward human osteosarcoma U-2 OS cells in the dark ($IC_{50,dark} \geq 96$ μM), the photocytotoxicity of the complex remarkably increases upon decreasing the intracellular pH from 7.5 ($IC_{50,light}$ = 3.84 μM) to 5.5 ($IC_{50,light}$ = 0.93 μM) due to increased $^1O_2$ generation under acidic conditions.

6.2. ROS-Activatable Photosensitizers

The delicate balance between the generation and elimination of ROS is pivotal for maintaining intracellular redox homeostasis.[221] At low-to-moderate concentrations, ROS serve as crucial mediators of signal transduction; however, excessive ROS production will lead to oxidative stress, inducing severe cellular damage and cell death. Compared to normal cells, cancer cells exhibit elevated levels of ROS to promote tumor progression and development.[222]

Mao, Tan, and co-workers have designed an iridium(III) complex appended with a ferrocene unit (**110**) as an ROS-activatable photosensitizer for treating TNBC.[223] The complex exhibits weak emission (Φ_{em} = 0.008) and $^1O_2$ generation (Φ_Δ = 0.02) due to efficient quenching by the electron-rich ferrocene moiety via PET. However, upon oxidation of the ferrocene unit by endogenous ROS, both the emission and $^1O_2$-generation capability of the complex are restored due to blockage of the PET process. Additionally, the ferrocene moiety can react with H_2O_2 in the presence of light to produce cytotoxic HO• through the photo-Fenton reaction. Thus, the ferrocene complex can catalyze the generation of ROS via both Type I and Type II processes in a self-amplifiable manner. Additionally, the presence of a ferrocene unit facilitates the binding of the complex with transferrin and promotes its cellular internalization via a transferrin receptor-mediated pathway, leading to higher cellular uptake of the complex in TNBC MDA-MB-231 cells with a high expression level of transferrin receptors. Thus, the complex shows selective photocytotoxic activity toward MDA-MB-231 cells ($IC_{50,light}$ = 0.05 μM; PI = 1509) over non-TNBC MCF-7 ($IC_{50,light}$ = 1.2 μM; PI = 19) and normal MCF-10A cells ($IC_{50,light}$ = 2.5 μM; PI = 33). Studies on the mechanism of action indicate that the photogenerated HO• and $^1O_2$ induce lipid peroxidation, triggering ferroptosis in MDA-MB-231 cells under both normoxia and hypoxia. Since ferroptosis can induce ICD, the complex stimulates robust antitumor immune response in a bilateral mouse model bearing 4T1 tumor xenografts upon irradiation, resulting in effective eradication of both primary and distant tumors.

6.3. GSH-Activatable Photosensitizers

In mammalian cells, GSH is the most abundant biothiol, with an intracellular concentration of ca. 1–10 mM. Serving as the primary cellular antioxidant, GSH plays a key role in maintaining cellular redox homeostasis to counteract oxidative stress-induced cell death. The elevated GSH levels observed in cancer cells compared to normal cells are crucial to tumor development and contribute to the increased resistance against chemotherapeutic agents.[224]

Lo and co-workers have designed four rhenium(I) complexes functionalized with a 2,4-dinitrophenylsulfonamide (DNPS) moiety (**111**) as thiol-activatable photosensitizers.[225] These complexes show weak emission (Φ_{em} = 0.003–0.043) and $^1O_2$ photosensitization (Φ_Δ = 0.06–0.15) due to efficient PET quenching from the rhenium(I) polypyridine unit to the electron-withdrawing DNPS moiety. Upon nucleophilic aromatic substitution reaction with intracellular GSH, the thiol-sensitive sulfonamide linker is cleaved, separating the quenching DNPS unit from the rhenium(I) core. As a result, the complexes display emission and $^1O_2$-photosensitization turn-on, contributing to their intense emission and high photocytotoxic activity in HeLa cells. Li and co-workers have developed ruthenium(II) (**112**)[226] and iridium(III) complexes (**113**)[227] bearing an α,β-unsaturated ketone moiety for GSH-mediated cancer imaging and PDT. Upon the addition reaction of GSH to the electron-deficient α,β-unsaturated ketone pendant, these complexes exhibit remarkable emission turn-on, offering opportunities for image-guided PDT of cancer cells with high intracellular GSH levels. Liu, Huang, Zhao, and co-workers have developed an iridium(III) complex bearing two electron-deficient *N*-alkyl pyridinium units (**114**) for GSH-selective imaging and PDT.[228] The introduction of two electron-deficient *N*-alkylpyridinium moieties enables efficient emission quenching by PET. However, the electron transfer from GSH to the pyridinium pendant increases its susceptibility to nucleophilic attack and promotes the substitution reaction by hydroxide in aqueous solutions, leading to an increased

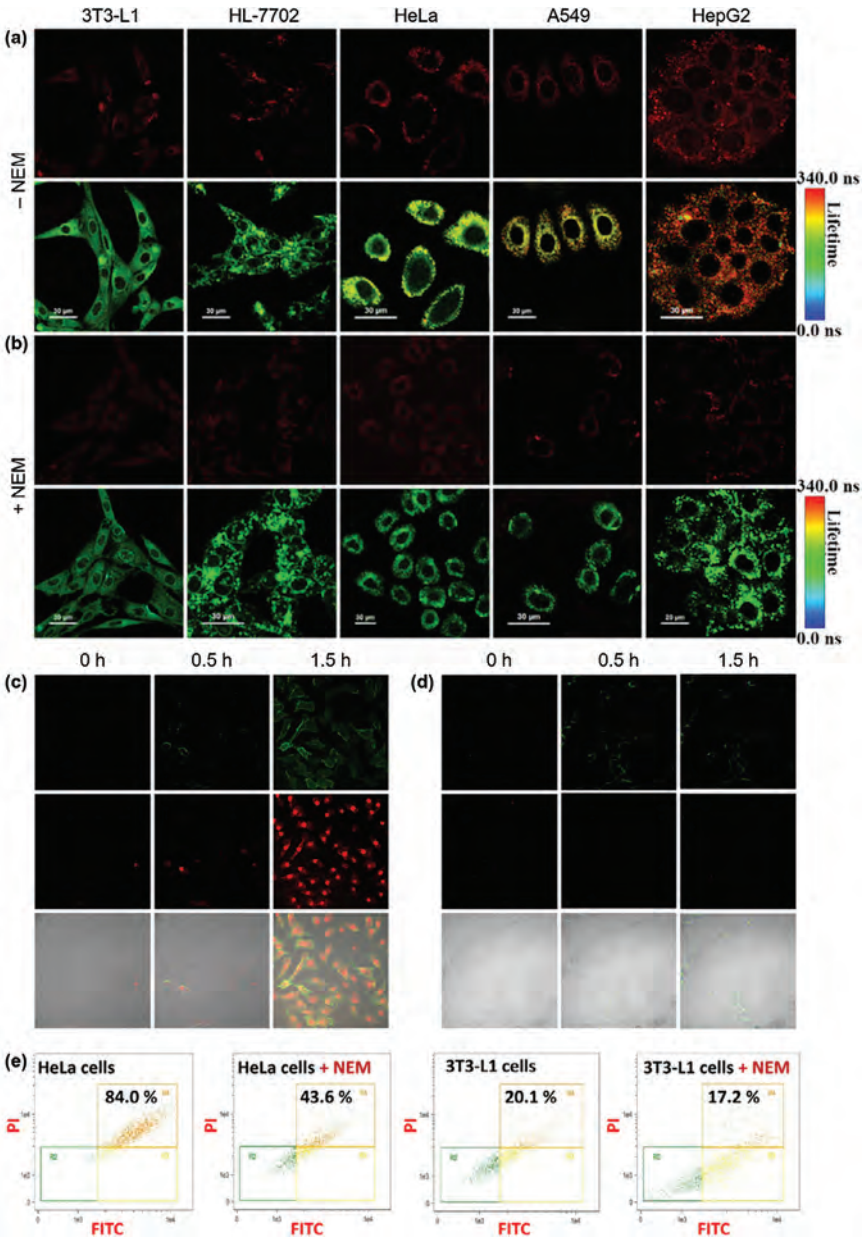

Figure 11. a,b) LSCM and PLIM images of different types of cells incubated with complex **114** (10 μM, 1 h) a) without and b) with pretreatment with the thiol scavenger *N*-ethylmaleimide (NEM) (2 μM, 20 min). λ_{ex} = 405 nm, λ_{em} = 550–650 nm. Scale bar = 30 μm. c,d) LSCM images of c) HeLa and d) 3T3-L1 cells incubated with complex **114** (10 μM, 1 h) and then irradiated (475 nm, 30 mW cm^{-2}, 10 min), followed by staining with Annexin V–FITC and propidium iodide (PI). λ_{ex} = 488 nm, λ_{em} = 500–560 nm (Annexin V–FITC); 600–680 nm (PI). e) Flow cytometric quantification of apoptosis in HeLa and 3T3-L1 cells under different treatments. Adapted with permission.[228] Copyright 2019 Wiley-VCH.

emission intensity (I/I_o = 12.5) and lifetime (from 84.7 to 690.5 ns) and an enhanced $^1O_2$ photosensitization quantum yield (from 0.12 to 0.68). These remarkable photophysical changes enable the facile differentiation between cancerous (HeLa, A549, and HepG2) and non-cancerous (3T3-L1 and human liver HL-7702) cells using LSCM and PLIM, as well as the selective induction of photocytotoxicity in cancer cells due to different intracellular GSH levels (**Figure 11**). Chao and co-workers have developed a dinuclear ruthenium(II) complex (**115**) as a GSH-activatable photosensitizer for two-photon-induced PDT.[229] The electron-deficient azo group functions as both a bridging unit and an emission quencher; thus, reduction of the azo group by GSH to a non-quenching hydrazo derivative results in a substantial increase in the emission intensity (I/I_o = 50), TPA cross-section ($\delta_{810\,nm}$ = 210 GM), and $^1O_2$ generation efficiency (Φ_Δ = 0.40) of the complex. As a result, the complex shows high photocytotoxic activity toward cancer cells and MCTSs upon two-photon excitation (810 nm).

6.4. NADH-Activatable Photosensitizers

The balance between the NAD(P)H/NAD(P)$^+$ redox couples is crucial to maintaining intracellular redox homeostasis and regulating a wide range of cellular processes such as energy metabolism, calcium homeostasis, gene expression, and immune response.[230] Alternations in these redox couples have been linked to various pathological conditions. Specifically, increased levels of NAD(P)H in cancer cells are vital for countering oxidative stress to facilitate cell proliferation and survival.[231]

Suresh, Maiti, and co-workers have designed an iridium(III) complex carrying two *N*-methylquinolinium moieties (**116**) as an NADH-activatable theranostic agent.[232] This complex exhibits weak emission and $^1O_2$ photosensitization due to efficient PET from the iridium(III) center to the electron-deficient quinolinium units. However, reduction of the quinolinium moiety by NADH through hydride transfer inhibits PET quenching, substantially increasing the emission intensity and $^1O_2$ generation efficiency of the complex. This structural transformation also weakens the electrostatic interaction between the complex and gold nanoparticles (AuNPs), reducing the surface-enhanced Raman scattering (SERS) signal. These changes enable bimodal detection of endogenous NADH in HepG2 cells via luminescence and SERS imaging. Notably, the complex can serve as an NADH scavenger in the dark and generate $^1O_2$ and NAD$^\bullet$ upon irradiation, inducing NADH depletion and redox imbalance to trigger apoptosis in cancer cells under both normoxic and hypoxic conditions.

6.5. H_2S-Activatable Photosensitizers

Hydrogen sulfide (H_2S), recognized as the third gaseous signaling molecule alongside nitric oxide and carbon monoxide (CO), serves as an endogenous gasotransmitter participating in diverse biological processes.[233] In cancer cells, H_2S is overproduced and engages in multiple signaling pathways associated with cell proliferation and migration, playing a crucial role in promoting tumor growth and metastasis.[234]

Maiti and co-workers have developed an iridium(III) complex functionalized with a 7-nitro-2,1,3-benzoxadiazole (NBD) unit (**117**) as a H_2S-activatable theranostic agent.[235] In the absence of H_2S, the complex shows low emission intensity and $^1O_2$ generation efficiency due to efficient PET from the iridium(III) center to the NBD moiety. However, the ether linker is cleaved upon nucleophilic attack by H_2S, which separates the quenching NBD unit from the iridium(III) complex, giving rise to substantial emission enhancement. Additionally, the H_2S-mediated cleavage reaction generates NBD-SH, which shows an intense characteristic Raman peak at 1328 cm^{-1} in the presence of AuNPs as the SERS substrate. The increase in both the emission and SERS signals enables the monitoring of the activation of complex **117** at the cellular level through luminescence and SERS imaging, revealing its rapid reaction with H_2S in human breast adenocarcinoma SK-BR-3 cells but not in normal MCF-10A cells. Upon cellular uptake, the complex is enriched in the mitochondria of SK-BR-3 cells, allowing the detection and quantification of the subtle fluctuations in mitochondrial H_2S levels. Importantly, the reaction of the complex with endogenous H_2S in SK-BR-3 cells results in H_2S depletion, which inhibits glyceraldehyde 3-phosphate dehydrogenase (GADPH) activity and ATP synthesis and thereby disrupts mitochondrial function and glycolysis. Upon irradiation, the excessive production of ROS leads to mitochondrial depolarization and the release of cytochrome *c*, triggering apoptosis-mediated cell death. Notably, SERS imaging provides additional insights into the apoptotic events, showing the changes in various biomolecular events (e.g., DNA fragmentation, protein denaturation, and cytochrome *c* release) after the PDT treatment. Furthermore, the complex can differentiate the blood samples collected from breast cancer patients and healthy volunteers based on their H_2S expression levels through bimodal luminescence and SERS detection, highlighting the broad clinical potential of the complex in cancer diagnosis and therapy.

6.6. Enzyme-Activatable Photosensitizers

Enzymes are essential in maintaining cellular homeostasis and controlling metabolic activities. Aberrant enzyme activity is frequently associated with the onset and progression of various diseases including cancers.[236] Thus, cancer cells often show distinct enzyme activity profiles compared to normal cells as a result of the requirement for activated cell proliferation, invasion, and metastasis.[237]

6.6.1. Tyrosinase

Tyrosinase is a copper-containing oxidase that catalyzes the hydroxylation of L-tyrosine to 3,4-dihydroxyphenylalanine and its oxidation to dopaquinone, playing a key role in melanin biosynthesis.[238] Notably, tyrosinase is markedly overexpressed in melanoma, making it an important biomarker for the diagnosis and treatment of melanoma.[239]

Zhang, Yoon, and co-workers have developed a platinum(II) complex caged with a 3-hydroxybenzyloxy group (**118**) as a tyrosinase-activatable photosensitizer for imaging and PDT of melanoma.[240] Upon recognition by tyrosinase, the 3-hydroxybenzyloxy group is hydroxylated at the 4-position vacancy, initiating a spontaneous 1,6-rearragement–elimination reaction that leads to the uncaging of the platinum(II) complex, resulting in an increase in its emission intensity and $^1O_2$ generation efficiency. The complex has been used to image A375 cells that overexpress tyrosinase, and it induces cancer cell death through apoptosis upon continuous white-light irradiation. Remarkably, it can efficiently detect early-stage melanoma in A375 tumor-bearing mice and suppress tumor growth upon irradiation with no obvious side effects.

6.6.2. Reductases

In solid tumors, the hypoxic TME leads to an increase in reductive stress, which is accompanied by elevated expression of various reductases such as quinone reductases, nitroreductases, and azoreductases. The overexpression of these enzymes has been recognized as an important biomarker for cancer diagnosis[241] and therapy.[242]

Chen, Zhang, Chao, and co-workers have developed an iridium(III) complex carrying an anthraquinone moiety (**119**) as a mitochondria-targeting two-photon-active photosensitizer for generating reactive radicals against hypoxic tumors.[243] The complex is non-emissive in solutions (Φ_{em} = 0.005) due to the quenching anthraquinone unit; however, upon reduction by the overexpressed reductases in hypoxic cells, the anthraquinone moiety is converted to a non-quenching anthracene-diol derivative, resulting in substantial emission enhancement. Notably, the anthracene-diol derivative efficiently sensitizes the production of reactive radicals upon irradiation. The efficient photogeneration of reactive radicals in the mitochondria under hypoxia leads to a substantial reduction in MMP, resulting in significant cancer cell death in vitro and in vivo.

6.6.3. Furin

Furin is a ubiquitous proprotein convertase localized in the *trans*-Golgi network, playing a crucial role in the cleavage of substrates at the consensus sequence RX(K/R)R (X = any amino acid).[244] This enzymatic activity is pivotal for the proteolytic processing and conversion of proproteins into their active forms, including hormones, growth factors, and cytokines. Notably, furin is implicated in various pathological conditions, with its expression upregulated in various types of cancer for promoting tumor progression, metastasis, and angiogenesis.

Lo and co-workers have designed an iridium(III)-based peptide conjugate (**120**) as a furin-responsive theranostic agent.[245] The conjugate is constructed by conjugating a luminescent iridium(III) complex and an emission quencher QSY-7 to the N- and C-terminus of a furin-cleavable peptide CGGGGRVRR↓SVK (↓ indicates the cleavage site), respectively. The peptide conjugate is non-emissive in aqueous solutions (Φ_{em} = 0.003) due to FRET; however, the specific cleavage of the RVRR sequence by furin separates the quencher from the iridium(III) complex, leading to a substantial increase in the emission intensity (I/I_o = 11.0) and $^1O_2$ generation efficiency. The conjugate has been used to monitor furin activity in live HeLa cells, showing that the furin activity is reduced in the presence of furin inhibitor II. Remarkably, while the conjugate exhibits negligible cytotoxicity toward HeLa and HEK293 cells in the dark ($IC_{50,dark}$ = 29.1 and 31.5 μM, respectively), it shows higher photocytotoxic activity toward HeLa cells ($IC_{50,light}$ = 1.3 μM) compared to HEK293 cells ($IC_{50,light}$ = 8.2 μM) due to its higher cellular uptake and cleavage in cancer cells overexpressing furin.

6.7. Bioorthogonally Activatable Photosensitizers

Bioorthogonal chemistry has emerged as a powerful tool in chemical biology, enabling the investigation of the localization, dynamics, and functions of biomolecules in their native environments,[246] as well as the targeted delivery of theranostic agents for disease diagnosis and treatment.[247] Various efficient and selective bioorthogonal reactions have been developed, including copper(I)-catalyzed azide–alkyne cycloaddition (CuAAC),[248] strain-promoted azide–alkyne cycloaddition (SPAAC),[249] strain-promoted alkyne–nitrone cycloaddition (SPANC),[250] strain-promoted sydnone–alkyne cycloaddition (SPSAC),[251] and inverse electron-demand Diels–Alder (IEDDA) reaction.[252] The exploitation of these "new-to-nature" reactions can enable a high degree of control of both the localization and activation of photosensitizers, enhancing the precision of PDT.[253]

Lo and co-workers have designed four iridium(III) complexes appended with a nitrone unit (**121**) as bioorthogonally activatable photosensitizers for imaging and PDT.[254] The introduction of a nitrone moiety provides a facile non-radiative decay pathway for triplet state deactivation through photoinduced C=N isomerization, resulting in very weak emission ($\Phi_{em} \leq$ 0.023) and $^1O_2$ photosensitization (Φ_Δ = 0.19–0.26). However, upon the SPANC reaction with (1*R*,8*S*,9*s*)-bicyclo[6.1.0]non-4-yn-9-ylmethanol (BCN-OH), the quenching nitrone unit is converted to a non-quenching isoxazoline derivative, leading to a substantial increase in the emission intensities (I/I_o = 7.2–47.1) and $^1O_2$ generation efficiencies (Φ_Δ = 0.42–0.91) of the complexes. The emission and $^1O_2$-photosensitization turn-on properties allow selective imaging and photoactivated killing of Chinese hamster ovary (CHO)-K1 cells transfected to express SNAP-tag proteins using BCN-modified O^6-benzylguanine (BCN-BG) as a substrate.

Iridium(III) complexes bearing a tetrazine moiety (**122**) have also been developed for bioorthogonal imaging and PDT.[255] The emission of these complexes is quenched due to a dual quenching mechanism involving FRET and PET from the iridium(III) core to the tetrazine unit. Upon the IEDDA reaction with BCN-OH, these complexes exhibit enhanced emission intensities and $^1O_2$ generation efficiencies (I/I_o = 51.7–105.3; Φ_Δ = 0.31–0.76). These increases are larger than those with *trans*-cyclooct-4-en-1-ol (TCO-OH) (I/I_o = 1.8–13.5; Φ_Δ = 0.23–0.36), indicative of bioorthogonal control of the luminescence and $^1O_2$-photosensitization behavior of tetrazine complexes by using different reaction partners. Complex **122b** has been utilized for selective imaging and photoactivated killing of HeLa cells transfected to express HaloTag proteins using a BCN-modified chloroalkane substrate (BCN-C6-Cl). Iridium(III) *bis*-tetrazine complexes (**123**) have also been developed as phosphorogenic bioorthogonal probes for *bis*-cyclooctynylated substrates.[256] These complexes show extremely weak emission (Φ_{em} = 0.0001–0.0009) and $^1O_2$ photosensitization (Φ_Δ = 0.02–0.07) due to the tetrazine moieties. However, reaction of the complexes with a *bis*-cyclooctynylated substrate (*bis*-BCN) results in a significant increase in their emission intensities (I/I_o = 1008.2–3885.7) and $^1O_2$ photosensitization efficiencies (Φ_Δ = 0.62–0.77). These changes enable selective imaging and photocytotoxicity toward cells pretreated with *bis*-BCN.

Lo and co-workers have utilized enzyme-instructed self-assembly (EISA) and bioorthogonal chemistry to develop a targeting approach that allows for selective accumulation and controllable activation of ruthenium(II) tetrazine complexes (**124**) in cancer cells.[257] This two-step cancer-targeting approach involves the use of a BCN-modified self-assembling peptide Nap-FFK(BCN)Yp (Nap = naphthalene, Yp = phosphorylated tyrosine) to anchor the BCN units. Dephosphorylation of the peptide by alkaline phosphatase (ALP) overexpressed in cancer cells induces the formation of large supramolecular assemblies in these cells, leading to the large accumulation of BCN units in

cancer cells. Subsequent IEDDA reaction with the tetrazine complexes enables their selective localization in cancer cells and activation of their emission and $^1O_2$-photosensitization properties for cancer-selective imaging and PDT. Notably, the photocytotoxicity of the ruthenium(II)-containing supramolecular assemblies is higher when EISA occurs in the intracellular space than on the cell membrane, as the photogenerated $^1O_2$ causes direct oxidative damage to proximal organelles instead of diffusing across the plasma membrane or extracellular space, illustrating the importance of cellular localization in determining their photocytotoxic activity.

Furthermore, Lo and co-workers have utilized a "click-to-release" approach to activate the emission and $^1O_2$-photosensitization behavior of rhenium(I) tetrazine complexes (**125**).[258] These complexes display weak emission (Φ_{em} = 0.029–0.039) and $^1O_2$ photosensitization (Φ_Δ = 0.22–0.27) due to the quenching tetrazine moiety. Incubation of the complexes with TCO-OH induces the bioorthogonal cleavage of the tetrazine carbamate linker, liberating the aminomethylpyridine complexes coupled with emission and $^1O_2$-generation turn-on. Notably, the PEG complex **125d** exhibits relatively low dark cytotoxicity ($IC_{50,dark}$ = 51.1–73.7 μM) but substantially enhanced cytotoxic activity toward TCO-OH-pretreated cells upon irradiation ($IC_{50,light}$ = 0.6–4.6 μM), resulting from the synergistic release of the highly cytotoxic aminomethylpyridine complex and increased $^1O_2$ generation. Studies on the mechanism of action indicate that the complex localizes in the lysosomes and induces lysosomal dysfunction, autophagy suppression, and ICD upon sequential bioorthogonal cleavage reaction and light irradiation.

6.8. Discussion

The development of activatable photosensitizers that specifically respond to tumor-associated stimuli (e.g., low pH, elevated ROS/GSH levels, and aberrant enzyme activity) has emerged as a promising approach to address the limitations of non-selective tissue distribution and uncontrollable ROS generation observed in traditional photosensitizers. These smart photosensitizers can confine their photocytotoxic effects to cancer cells while sparing surrounding normal tissues, thereby improving the precision and effectiveness of PDT. However, the use of photosensitizers that respond to a single stimulus may still cause damage to normal tissues if the difference between cancer and normal cells is subtle. To address this issue, a feasible solution lies in the development of transition metal complexes capable of responding to multiple stimuli. The photoactivity of these complexes is only activated upon the simultaneous presence of two distinct stimuli, thereby minimizing off-target activation and photodamage. Another approach involves the utilization of bioorthogonal reactions for targeted activation of the photosensitizers at the tumor site. The introduction of abiotic chemical reporters to cancer cells through metabolic engineering or receptor targeting can overcome the challenges posed by tumor heterogeneity such as variations in pH, ROS/GSH levels, and enzyme activity among different cancer cells. In addition to the typical bioorthogonal ligation or dissociation reactions, there is emerging interest in exploiting the non-covalent interaction between synthetic host–guest pairs as a bioorthogonal strategy for tumor pretargeting due to their high structural selectivity, fast association kinetics (k_{on} = ca. 10^7 M^{-1} s^{-1}), and tunable binding affinity (K_a up to 10^{15} M^{-1}).[259] The rapidly evolving field of bioorthogonal chemistry is expected to offer new opportunities for the development of activatable photosensitizers for cancer-targeted PDT.

7. Transition Metal Complexes for TME Remodeling and PDT

The TME is a complex and dynamic milieu encompassing interactions between cancer cells and various non-malignant cells (e.g., immune cells, endothelial cells, stromal cells, and cancer-associated fibroblasts) as well as non-cellular components (e.g., ECM, cytokines, chemokines, and growth factors).[260] Compared to normal tissue environment, the TME displays several distinct features including hypoxia,[29] mild acidity,[215] and overproduction of GSH[224] and H_2O_2[261] due to metabolic alternations in cancer cells, which contribute to tumor growth, metastasis, immunosuppression, and resistance to therapies including PDT. Recent advancements in nanoparticle engineering have led to the development of innovative approaches for targeting and remodeling the TME, offering promising opportunities to enhance the effectiveness of PDT and improve therapeutic outcomes.[262]

7.1. Hypoxia Alleviation

Hypoxia is a major hallmark of solid tumors, posing a significant challenge for various O_2-dependent therapies including PDT.[29] A direct method to address tumor hypoxia is to replenish O_2 through the use of O_2 nanocarriers or the in situ O_2 production.[55] Given that water is the most abundant molecule in cells, the incorporation of water splitting materials in conjugation with photosensitizers can provide a sustainable source of O_2 for ROS production. This approach can overcome the limited availability of O_2 in hypoxic TME, thereby enhancing the efficacy of PDT against large solid tumors.

Titanium oxide (TiO_2)-based materials are the most prominent photocatalysts used for water splitting due to their high photocatalytic activity, excellent chemical stability and photostability, minimal toxicity, and low cost.[263] Mao, Cheng, Tan, Wu, and coworker have designed a hypoxia-adaptive nanocomposite (**TiO_2-126@siRNA**) for photoimmunotherapy against oral squamous cell carcinoma (OSCC).[264] The nanocomposite is formed upon the covalent attachment of carboxyl-modified TLD1433 (**126**) (**Figure 12**) to the surface of amine-functionalized TiO_2 nanoparticles, followed by loading with a small interfering RNA (siRNA) targeting HIF-1α. Upon photoexcitation, the PET from the ruthenium(II) complex to TiO_2 results in efficient electron–hole separation, facilitating the production of $HO^\bullet$ and $^1O_2$. These photogenerated ROS induce lysosome damage and promote siRNA escape to alleviate tumor hypoxia. The effective modulation of the hypoxic and immunosuppressive TME facilitates the induction of potent antitumor immune response to inhibit oral carcinogenesis in vivo.

Graphitic-phase carbon nitride (g-C_3N_4)-based nanomaterials are a class of metal-free conjugated semiconductor photocatalysts used for water splitting.[265] Cheng, Zhang, and coworkers have utilized iron-doped g-C_3N_4 as a platform to develop

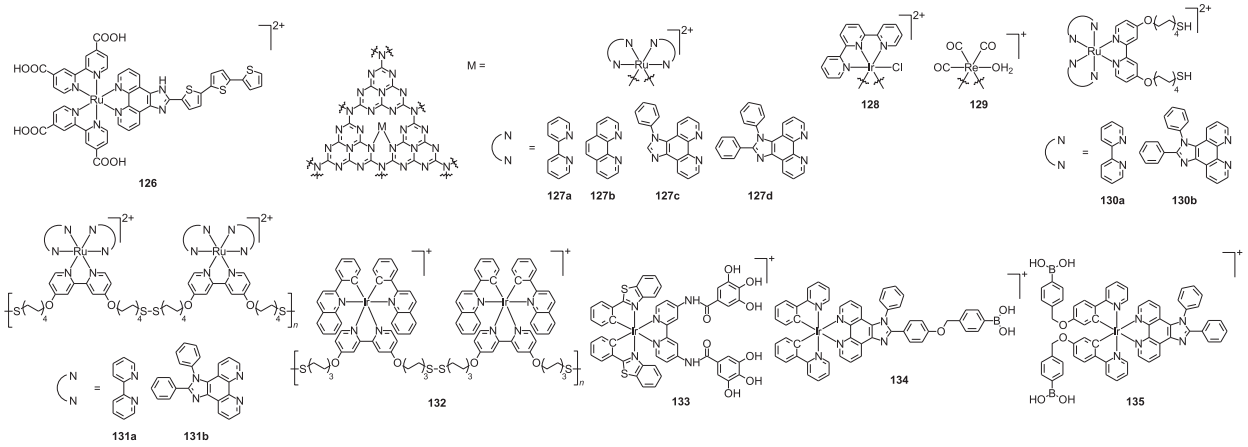

Figure 12. Structures of transition metal complexes for hypoxia alleviation (**126**–**129**) and GSH depletion (**130**–**135**).

an O_2-evolving nanophotosensitizer for PDT against hypoxic tumors.[266] The iron-doped g-C_3N_4 is loaded with $[Ru(bpy)_3]^{2+}$ and coated with a hyperbranched conjugated polymer (HCP). The HCP possesses a large TPA cross-section ($\delta_{800\,nm}$ = 1128 GM) and exhibits strong blue fluorescence (λ_{em} = 452 nm), serving as a two-photon light-harvesting unit for $[Ru(bpy)_3]^{2+}$. Notably, the loading of $[Ru(bpy)_3]^{2+}$ allows efficient sensitization of the iron-doped g-C_3N_4 upon two-photon excitation through PET, facilitating the generation of O_2 via water splitting for $^1O_2$ photosensitization and thus inducing high photocytotoxicity under hypoxia. In vivo experiments show that the nanocomposite specifically accumulates at the tumor site following tail vein injection and significantly suppresses tumor growth upon irradiation. Metabonomics studies reveal that the nanocomposite promotes HIF-1α degradation and produces succinic acid upon irradiation, thereby reprograming the TME to enhance the PDT efficacy.

Wang, Zhang, Chao, and co-workers have coordinated a ruthenium(II) complex to the surface of g-C_3N_4 nanosheets to afford an O_2 self-sufficient photosensitizer (**127a**) for PDT under hypoxia.[267] The direct metal coordination substantially enhances the photocatalytic activity of g-C_3N_4 nanosheets, facilitating the photoinduced conversion of water or H_2O_2 to O_2 and ROS including $O_2^{\bullet-}$, $HO^{\bullet}$, and $^1O_2$. The production of multiple cytotoxic ROS in hypoxic cells increases oxidative stress, inducing mitochondria dysfunction and apoptosis. Notably, the coordination of ruthenium(II) complexes bearing more π-conjugated ligands to the surface of g-C_3N_4 nanosheets yields nanoconjugates (**127b–127d**) with exceptional TPA (δ = up to 34209 GM) and $^1O_2$ generation capabilities (Φ_Δ = up to 0.72).[268] To enhance the pharmacological properties, nanoconjugate **127d** has been formulated into nanoparticles through encapsulation into DSPE-PEG. The resultant nanoparticles (**PM@127d**) induce efficient cell death in hypoxic cancer cells and MCTSs by a combination of apoptosis, paraptosis, ferroptosis, and ICD upon two-photon excitation. The induction of immune response in vivo effectively inhibits the growth of both primary and distant tumors in bilateral B16-F10 tumor-bearing mice. In addition to the photophysical and photochemical properties, the cellular localization behavior and thus the mechanism of action of the g-C_3N_4 nanosheets can be manipulated by a judicious choice of transition metal complexes. The functionalization of g-C_3N_4 nanosheets with an iridium(III) complex produces a nanoconjugate (**128**) that selectively targets the mitochondria of cancer cells, inducing mitochondrial dysfunction upon irradiation and triggering cell death via both ferroptosis and apoptosis pathways.[269] As a result, the nanoconjugate can effectively inhibit tumor growth in A375 tumor-bearing mice upon two-photon excitation (750 nm) within a single treatment. In contrast, the modification of g-C_3N_4 nanosheets with a rhenium(I) complex affords a nanoconjugate (**129**) that specifically targets the ER of cells, inducing robust ROS-mediated ER stress upon irradiation and triggering cell death by a combination of apoptosis, pyroptosis, ferroptosis, and ICD.[270] The activation of diverse cell death pathways enables efficient killing of doxorubicin-resistant MDA-MB-231 cells and MCTSs. Remarkably, the induction of ICD triggers potent antitumor response, significantly inhibiting the growth of both primary and distant tumors (TIR = 86 and 77%, respectively) in bilateral 4T1 tumor-bearing mice.

7.2. GSH Depletion

In cancer cells, the elevated production of GSH serves as a crucial defense mechanism against ROS-induced damage, facilitating tumor initiation, progression, and metastasis and conferring resistance to ROS-based therapies.[224] Thus, depleting GSH levels in cancer cells represents a promising approach to weaken their antioxidant defense against oxidative stress, enhancing the effectives of PDT.[271]

Chao and co-workers have utilized ruthenium(II) complexes carrying two terminal thiol groups (**130**) to prepare GSH-sensitive polymer nanoparticles (**131**) that can deplete endogenous GSH for enhanced PDT.[272] Upon internalization into cancer cells, the high levels of endogenous GSH induce significant disulfide bond cleavage and thus the disintegration of the nanoparticles, releasing the constituent ruthenium(II) monomers into the cytoplasm. This process can be monitored in real time using PLIM (**Figure 13a**) due to the distinct emission lifetimes of the ruthenium(II) complexes in the monomeric state (621 and 924 ns) and when embedded within the nanoparticles (385 and 168 ns). Notably, the formulation of the complexes into GSH-sensitive polymer nanoparticles enhances their

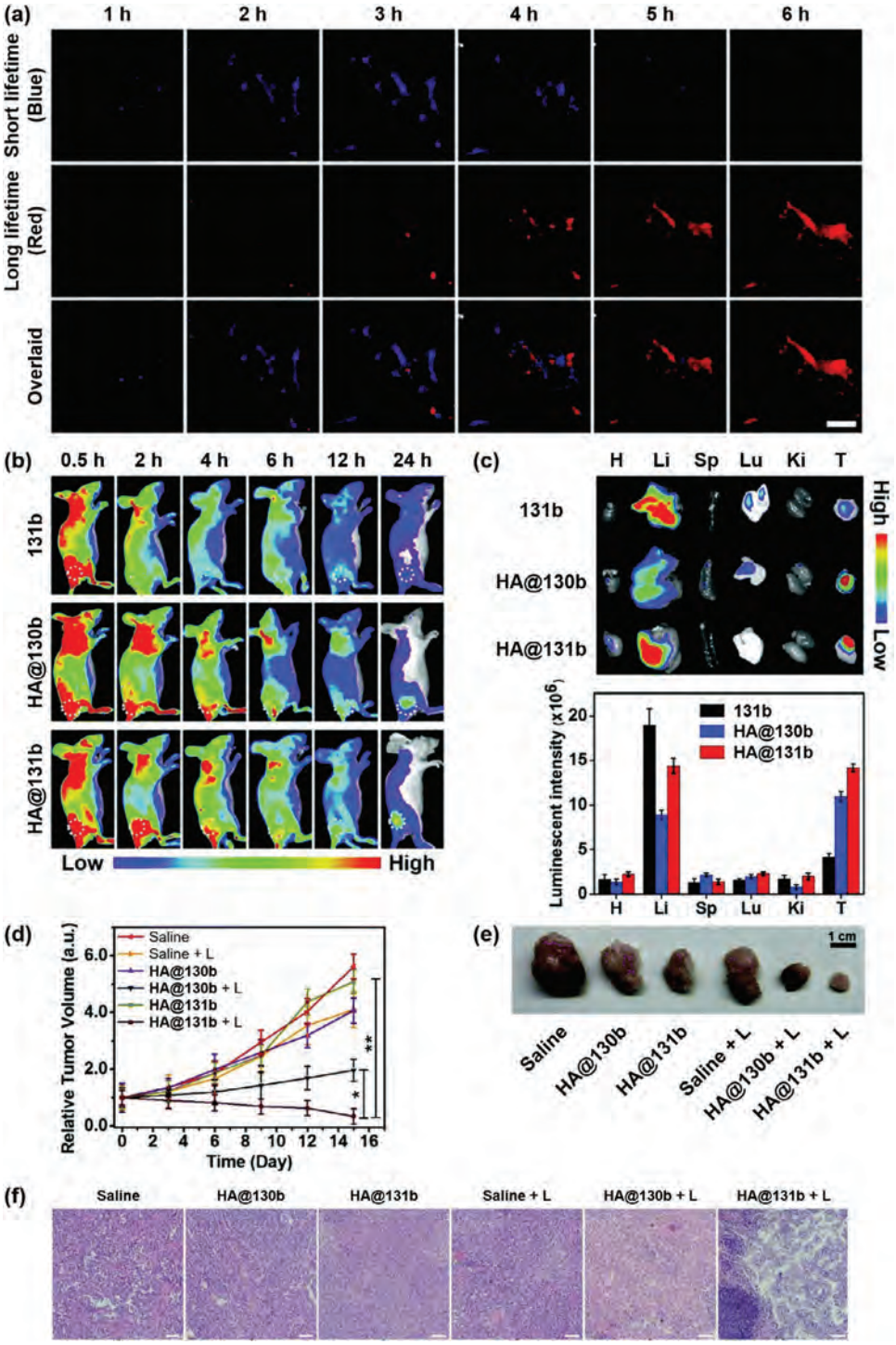

Figure 13. a) Real-time PLIM images of MDA-MB-231 cells incubated with the polymer nanoparticle **131b** (10 μM) for 1, 2, 3, 4, 5, and 6 h. λ_{ex} = 810 nm, λ_{em} = 590–620 nm. b) Luminescence images of MDA-MB-231 tumor-bearing mice administrated with nanoparticles **131b**, **HA@130b**, and **HA@131b** ([Ru] = 0.01 mmol kg^{-1}) through intravenous injection. The images were taken at 0.5, 2, 4, 6, 12, and 24 h postinjection. The tumor sites are marked with white dashed circles. c) Representative images and average luminescence intensity of main organs and tumor harvested from the mice at 6 h postinjection. H: heart; Li: liver; Sp: spleen; Lu: lung; Ki: kidney; T: tumor. d) Tumor growth curves of MDA-MB-231 tumor-bearing mice under different treatments (n = 5), ** $p < 0.01$ and * $p < 0.05$. e) Representative photographs and f) H&E staining images of tumors harvested from MDA-MB-231 tumor-bearing mice after different treatments. **HA@130b** and **HA@131b**: [Ru] = 0.01 mmol kg^{-1}; L = 810 nm, 50 mW, 1 kHz, pulse width 35 fs, 5 s mm^{-1}. Adapted with permission.[272] Copyright 2021, Royal Society of Chemistry.

cellular uptake while reducing GSH levels in cancer cells. Consequently, the polymer nanoparticles **131a** and **131b** show significantly higher photocytotoxic activity toward MDA-MB-231 cells ($IC_{50,light}$ = 5.1 and 2.8 μM, respectively) than their constituent monomers ($IC_{50,light}$ > 40 μM) upon two-photon irradiation. To facilitate in vivo PDT applications, the nanoparticles have been coated with hyaluronic acid (HA) to endow them with tumor-targeting capabilities. As revealed by in vivo and ex vivo luminescence imaging, the HA-coated nanoparticles (**HA@131b**) display more effective tumor accumulation in MDA-MB-231 tumor-bearing mice than the unmodified nanoparticles (**131b**) or free complex encapsulated in HA (**HA@130b**) after intravenous injection (Figure 13b,c). Importantly, upon two-photon excitation (810 nm, 15 J cm^{-2}), the HA-coated nanoparticles **HA@131b** induce significant tumor regression with minimal side effects (Figure 13d–f). A related iridium(III) polymer nanoparticle (**132**) has also been developed for two-photon-induced PDT.[273] This nanoparticle specifically accumulates in the mitochondria and induces mitochondria dysfunction and fragmentation upon irradiation through the production of $O_2^{\bullet-}$ and $^1O_2$. Furthermore, the nanoparticle efficiently depletes endogenous GSH, resulting in GPX4 downregulation and LPO accumulation. As a result, the nanoparticle induces cancer cell death via both apoptosis and ferroptosis pathways. The nanoparticle has been encapsulated into DSPE-PEG-biotin to facilitate its tumor-selective uptake in vivo and induces almost complete tumor ablation upon two-photon excitation.

Pan, He, Chao, and co-workers have utilized the coordination-driven self-assembly between an iridium(III) complex modified with two pyrogallol moieties (**133**) and Fe^{3+} to prepare a pH-responsive nanoscale coordination ensemble (**PM@133-Fe**) for PDT.[274] Upon cellular internalization, the nanoensemble specifically accumulates in acidic lysosomes and dissociates into complex **133** and Fe^{3+}. The released complex **133** generates $O_2^{\bullet-}$ and $^1O_2$ upon irradiation, inducing apoptosis and autophagy; while the released Fe^{3+} is reduced by GSH to Fe^{2+}, triggering ferroptosis by causing GSH depletion. Camouflaging the nanoensemble with A375-derived exosomes promotes its selective uptake in A375 cells, increases tumor penetration, and prolongs blood circulation. These remarkable properties result in the enhanced accumulation of the nanoensemble at the tumor site in A375 tumor-bearing mice, enabling effective inhibition of A375 tumor growth and metastasis upon two-photon excitation and thereby significantly increasing the survival rate of the mice.

Tang, Chao, and co-workers have designed a boronic acid-caged prodrug (**134**) that can release an iridium(III) complex as a $^1O_2$ photosensitizer for two-photon-induced PDT and methylquinone as a GSH scavenger for GSH depletion in response to the elevated levels of H_2O_2 in the TME.[275] Interestingly, the H_2O_2-mediated boronic acid cleavage reaction is accompanied by a substantial reduction in the emission intensity and lifetime of the complex. These photophysical changes facilitate the monitoring of the prodrug activation process using LSCM and PLIM, revealing that the complex specifically accumulates in the mitochondria of human gastric adenocarcinoma AGS cells after cellular uptake, with the cleavage reaction occurring within 1 h of incubation. The released methylquinone reacts with endogenous GSH and disrupts redox homeostasis inside the mitochondria. Thus, the ROS generated upon irradiation induce MMP reduction, initiating apoptosis-mediated cell death. Notably, the complex exhibits higher photocytotoxicity toward AGS cells ($IC_{50,light}$ = 0.51 μM) than other cancerous (A549 and HeLa) and normal (LO2) cell lines ($IC_{50,light}$ = 2.62–6.1 μM) due to higher intracellular H_2O_2 levels, enabling selective eradication of AGS tumors in vivo upon irradiation. Zhao, Chao, and co-workers have modified selenium nanoparticles (SeNPs) with an NIR luminescent iridium(III) boronic acid complex (**135**) and camouflaged with A375 cell membrane for specific two-photon-induced PDT against melanoma.[276] The SeNPs can dissociate in cancer cells, releasing selenium that binds to and depletes intracellular GSH. This synergizes with the released methylquinone to disrupt the intracellular redox balance, sensitizing the cells to oxidative stress. As a result, the nanocomposites (**SeNP-135@CM**) show high photocytotoxic activity toward A375 cells ($IC_{50,light}$ = 4.4 μM), while displaying negligible (photo)cytotoxicity toward other cancer (A549, HepG2, and MCF-7) and normal (LO2) cell lines (IC_{50} ≥ 31.8 μM). Furthermore, the NIR luminescence properties of the complex allow for real-time tracking of the nanocomposite biodistribution in A375 tumor-bearing mice via in vivo luminescence imaging. Notably, the cancer cell membrane-camouflaged nanocomposites exhibit prolonged blood circulation time ($t_{1/2}$ = 5.4 h) and increased tumor retention (7% ID g^{-1}) compared to their unmodified counterparts (**SeNP-135**) ($t_{1/2}$ = 1.7 h; < 4% ID g^{-1}). The efficient and selective tumor accumulation of the nanocomposites enables almost complete eradication of tumors with a single dose of NIR light (730 nm).

7.3. Discussion

The intricate TME poses a significant obstacle to the effective clinical application of PDT in cancer treatment. However, advancements in our understanding of the TME have led to the identification of various biological barriers that compromise the effectiveness of PDT, fueling the development of innovative approaches to remodel the TME and enhance PDT outcomes. Among these strategies, nanoparticles have emerged as a crucial tool for targeting and regulating the TME due to their controllable size, structure, composition, and surface modification.[262] Thus, the integration of photosensitizers with TME-modulating nanomaterials has allowed for enhanced PDT. Recent progress has focused on addressing two key challenges: 1) alleviating tumor hypoxia through O_2 replenishment and 2) suppressing antioxidant defense mechanisms via GSH depletion. However, exploring additional TME reprograming mechanisms is essential. For example, the ECM within the TME acts as a barrier impeding the diffusion of therapeutic agents and infiltration of immune cells into the tumor site, enhancing tumor resistance to various therapies.[277] Disrupting major ECM components such as collagen and HA using specific enzymes or inhibitors can degrade the ECM, reshaping the immunosuppressive TME. Another promising avenue involves targeting immunometabolism within the TME.[278] In particular, indoleamine 2,3-dioxygenase (IDO) represents a promising therapeutic target as it catalyzes the conversion of tryptophan to kynurenine, which suppresses effector T cell activation and promotes regulatory T cell generation.[279]

Blocking IDO with inhibitors such as NLG919 and 1-methyl-D-tryptophan can relieve kynurenine-mediated immunosuppression. Through these approaches, the immunosuppressive TME can be remodeled to enhance PDT-induced antitumor immune response, inhibiting tumor growth and metastasis. Additionally, the use of nanomaterials as a platform enables the combination of multiple TME reprogramming strategies. Thus, the integration of transition metal complexes with TME-modulating nanomaterials represents a promising design paradigm for more effective PDT agents.

8. Transition Metal Complexes for Combination Therapy

While PDT has shown effectiveness in treating various types of cancer, its therapeutic impact on deep-seated or large solid tumors is often limited due to its strong reliance on O_2 and light penetration depth. Incomplete elimination of cancer cells during PDT can lead to tumor recurrence and metastasis, resulting in poor prognosis. To address this challenge, the combination of PDT with other therapeutic modalities can offer a promising approach to overcome the limitations associated with PDT alone. Combination therapy that involves the simultaneous use of two or more treatments with distinct mechanisms of action has emerged as a promising treatment option for cancer in clinical settings.[280] Compared to monotherapies, combination therapy can produce enhanced therapeutic effects at lower doses, minimizing undesirable side effects and reducing the development of treatment resistance. Thus, the combination of PDT with other therapeutic modalities can generate an additive or even synergistic therapeutic effect, enhancing treatment efficacy and patient outcomes.

8.1. Combined PDT and Chemotherapy

Chemotherapy plays a vital role in cancer treatment in the clinic. However, conventional chemotherapeutic drugs have drawbacks such as low aqueous solubility, poor cancer selectivity, and high systemic toxicity. Furthermore, cancer cells with intrinsic or acquired multidrug resistance can regrow after exposure to chemotherapeutic agents, resulting in treatment failure and tumor recurrence.[3b] Since chemotherapy and PDT exert their therapeutic effects through different mechanisms of action, their combination can overcome multidrug resistance in cancer and even sensitize resistant cancer cells to chemotherapeutics, leading to enhanced therapeutic effects.

Cao, Mao, and co-workers have developed a three-in-one nanoplatform for combined PDT and chemotherapy.[281] The nanoplatform is constructed based on the self-assembly of an adamantane-functionalized ruthenium(II) complex (**136**) (**Figure 14**) with cyclodextrin (CD) through host–guest interaction, followed by loading of 5-fluorouracil (5-Fu) and lonidamine (LND). The octahedral geometry of the ruthenium(II) complex and the hydrogen bonding interaction between two adjacent CDs are crucial to bridge the monomers to form a 3D architecture for drug loading. The resultant nanoparticles (**136-CD@5-Fu/LND**) enter cells via an endocytic pathway and accumulate in the lysosomes, in which the acidic environment triggers the release of the drugs from the nanocarrier. Upon irradiation, the nanocarrier generates ROS and damages lysosomes, allowing the drugs to escape from the lysosomes and reach their sites of action, inducing mitochondria dysfunction and cancer cell apoptosis. In vivo studies show that the three-in-one nanoplatform can effectively inhibit tumor growth in A549 tumor-bearing mice (TIR = 85%) without inducing systemic side effects, outperforming the individual treatment modalities.

Liu, Zhao, and co-workers have designed two iridium(III) complexes conjugated with the chemotherapeutic drug camptothecin via a GSH-sensitive disulfide linker (**137**) for combined PDT and chemotherapy.[282] These complexes are encapsulated into folic acid-modified PF127 for precise targeting of cancer cells that overexpress FRs. Thus, the resultant micelles (**PM-FA@137**) display higher uptake and accumulation in FR-overexpressing HeLa cells than in MCF-7 cells with lower FR expression. Upon cellular internalization, the high levels of endogenous GSH trigger the cleavage of the disulfide bonds, releasing the iridium(III) complexes and camptothecin for PDT and chemotherapy, respectively. Notably, the combination of PDT and chemotherapy results in a synergistic therapeutic effect, effectively killing cancer cells at a lower dosage in comparison to individual treatment modalities.

Zhang and co-workers have utilized an amphiphilic iridium(III) complex (**138**) to develop a dual-responsive nanoplatform for the treatment of HCC with combined PDT and chemotherapy.[283] The complex features two long hydrophobic tails and two free amino groups, which allow the loading of DOX into the nanovesicles through hydrophobic interaction and the conjugation with transferrin through amide coupling, respectively. Owing to the EPR effect and active targeting of transferrin receptors overexpressed on cancer cells, the drug-loaded nanovesicles (**138-Tf@DOX**) can specifically accumulate in tumors and enter cancer cells through receptor-mediated endocytosis. Upon NIR-light irradiation, the nanovesicles generate ROS ($O_2^{\bullet-}$ and $^1O_2$) and release DOX. The release of DOX is further accelerated in the presence of GSH that induces the disassembly of the nanovesicles by cleaving the disulfide bonds in the complex. Treatment of mice bearing syngeneic Hepa 1-6 tumors with the nanovesicles and NIR-light irradiation leads to almost complete tumor ablation with negligible side effects, demonstrating the synergistic effect of combined PDT and chemotherapy. Additionally, the nanoplatform is compatible with PAI, enabling real-time monitoring of tumor progression during the treatment.

Sadler and co-workers have designed a concerted hypoxia- and light-activatable theranostic prodrug (**139**), wherein a ruthenium(II)-based photosensitizer and an aniline mustard are conjugated with an azo linkage, for multimodal cancer therapy.[284] Owing to the electron-withdrawing azo group, both the ruthenium(II) and aniline mustard moieties remain inactive. Thus, the prodrug exhibits low (photo)cytotoxicity toward both cancer (A549 and HepG2; IC_{50} = 36.7–56.6 μM) and normal cells (HEK293, MRC-5, and human liver epithelial THLE-3; IC_{50} = 30.2–60.5 μM) under normoxic conditions. However, in hypoxic cancer cells, the azo bond is reduced and cleaved by the overexpressed reductases, releasing: 1) a luminescent and photoactive ruthenium(II) complex that, upon irradiation, generates ROS such as $^1O_2$ and H_2O_2 and catalyzes the redox reactions between NADH and Fe^{3+}-cytochrome *c*; and 2) the bioactive

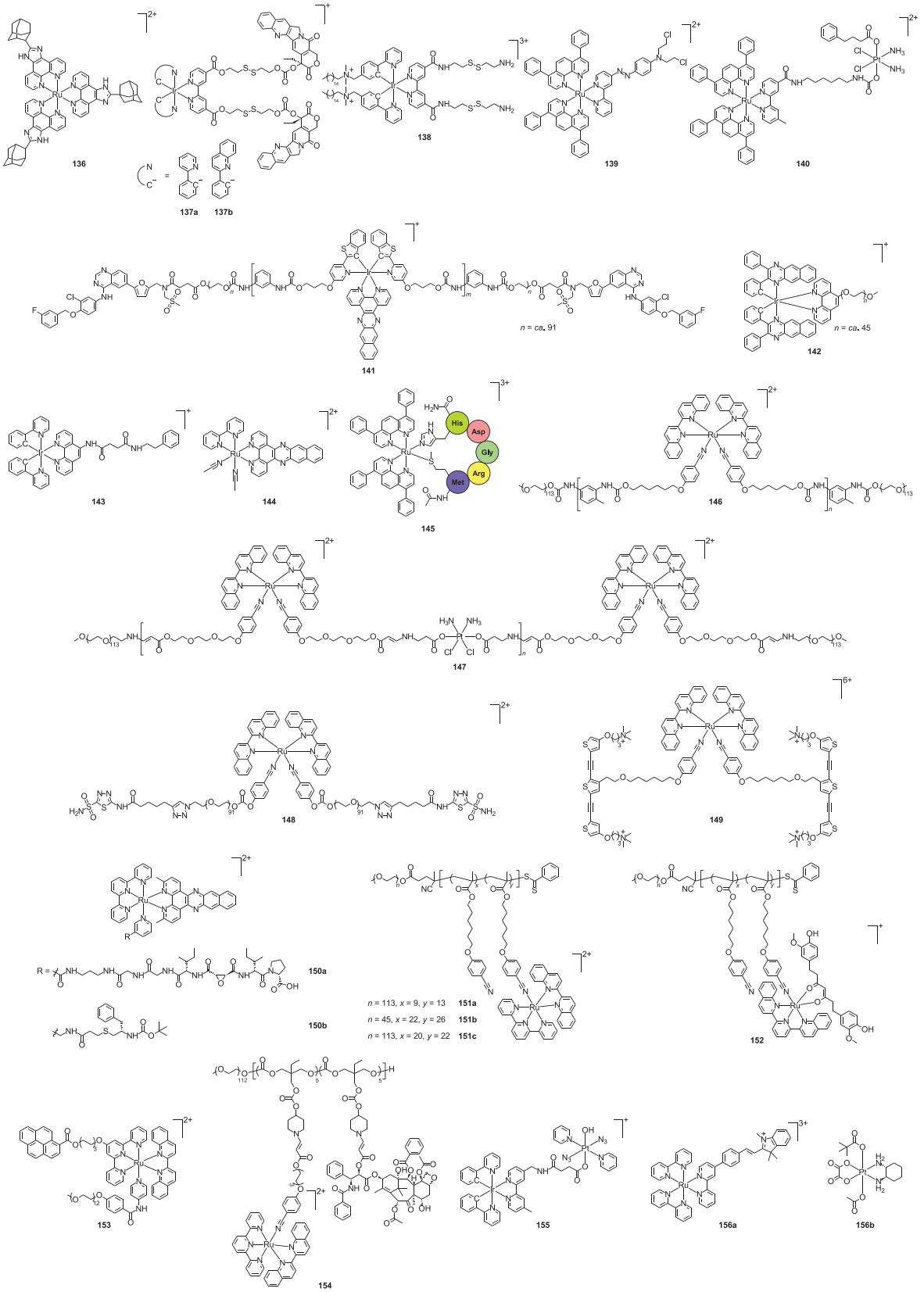

Figure 14. Structures of transition metal complexes for combined PDT and chemotherapy (**136**–**140**), PDT and targeted therapy (**141**), PDT and immunotherapy (**142** and **143**), PDT and PACT (**144**–**158**), and PDT and PTT (**159**–**170**).

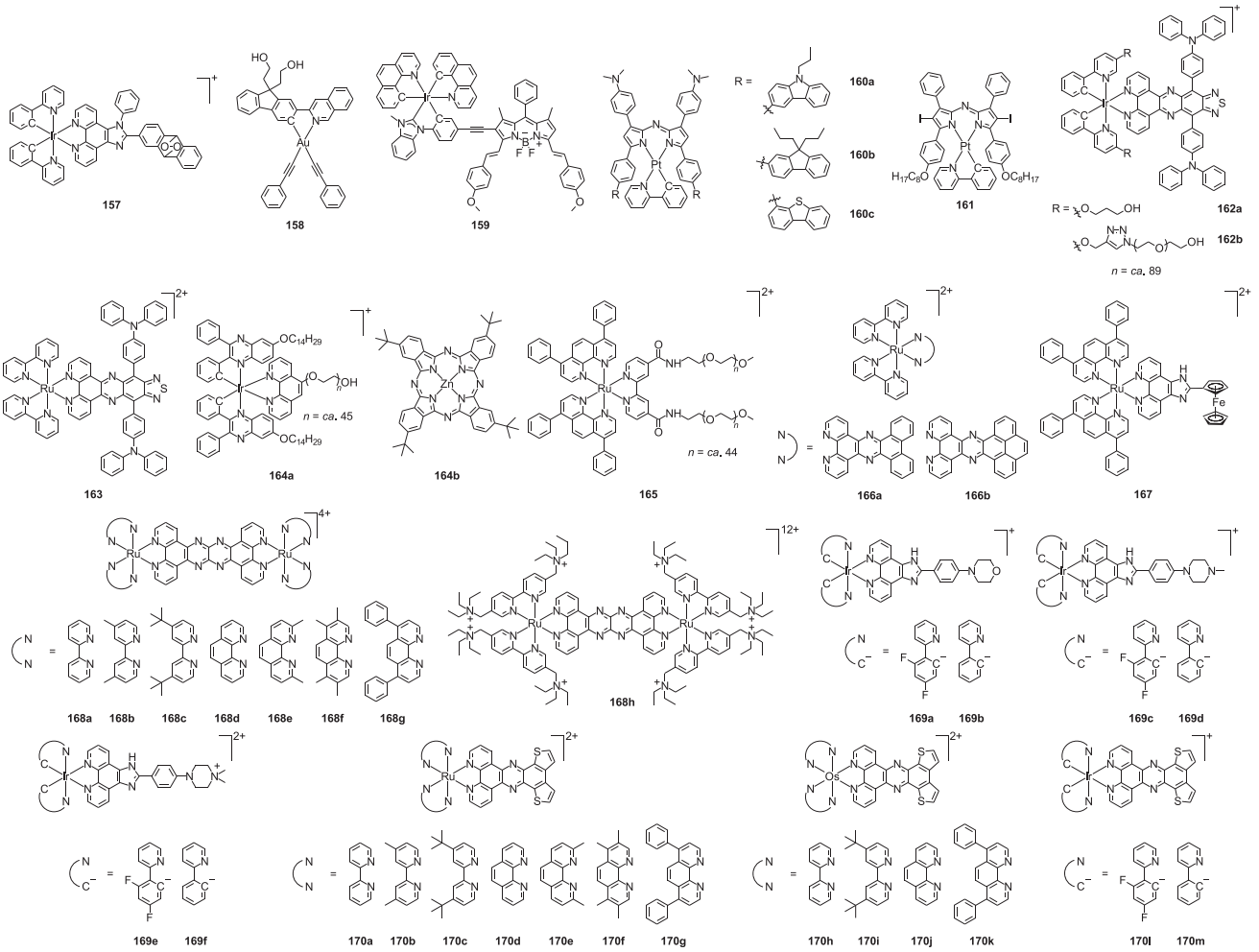

Figure 14. *Continued*

aniline mustard that crosslinks DNA. Since the prodrug specifically accumulates in the mitochondria after cellular uptake, the combined action of the two released entities induces ROS outburst, NADH and ATP deprivation, MMP reduction, and mtDNA depletion, triggering significant cancer cell death via apoptosis. As a result, the prodrug shows high photocytotoxic activity toward hypoxic HepG2 cells and MCTSs ($IC_{50,light}$ = 2.3 and 3.4 μM, respectively), effectively combating hypoxia-mediated drug resistance in cancer cells.

Gibson, Gasser, and co-workers have conjugated a ruthenium(II)-based photosensitizer with a platinum(IV) prodrug to afford a bimetallic complex (**140**) for combined PDT and chemotherapy.[285] Upon internalization into cancer cells, the platinum(IV) prodrug is reduced to cisplatin concomitant with the release of phenylbutyrate and the ruthenium(II) complex. The active cisplatin enters the cell nucleus and causes DNA damage through binding to DNA, which is favored by the released phenylbutyrate ligand that acts as a histone deacetylase (HDAC) inhibitor and induces chromatin de-condensation. Meanwhile, the released ruthenium(II) complex specifically accumulates in the Golgi apparatus of the cells and efficiently generates $^1O_2$ upon irradiation. The multiple targets and mechanisms of action of complex **140** effectively overcome drug resistance developed in tumors, resulting in similarly high photocytotoxicity toward A2780 cells ($IC_{50,light}$ = 0.08–0.16 μM) and its cisplatin-resistant (A2780cis; $IC_{50,light}$ = 0.10–0.19 μM) and doxorubicin-resistant derivatives (A2780ADR; $IC_{50,light}$ = 0.09–0.17 μM). The high photocytotoxic activity of the complex is also retained in A2780 MCTSs ($IC_{50,light}$ = 0.49–0.68 μM), highlighting the synergistic effect of combining PDT and chemotherapy.

8.2. Combined PDT and Targeted Therapy

The advancement in the knowledge of molecular events implicated in tumorigenesis and progression has led to the identification of novel molecular targets for targeted cancer therapy.[286] Targeted cancer therapy utilizes small-molecule inhibitors or monoclonal antibodies that target specific molecular targets in cancer cells, interfering with signal transduction pathways that regulate cell growth and proliferation, migration, metastasis, invasion, and angiogenesis within the tumor.[287] Compared to traditional chemotherapy, targeted cancer therapy specifically induces cytotoxicity toward cancer cells while sparing normal cells.

Thus, the combination of PDT with targeted therapy can produce a better therapeutic outcome compared with individual treatments.

Fang, Xu, Gou, and co-workers have developed an NIR light-activatable iridium(III)-based polymeric micelle for combined PDT and targeted therapy against human epithelial growth factor receptor 2 (HER2)-overexpressing cancers.[288] The polymeric micelle is constructed from the self-assembly of an amphiphilic iridium(III)-containing block copolymer conjugated with the HER2 inhibitor lapatinib at its two ends (**141**), with the hydrophobic iridium(III) complex embedded in the core and the hydrophilic PEG–lapatinib motifs localized in the shell. Additionally, $NaYF_4$:Yb/Tm@$NaYF_4$ UCNPs are incorporated into the micelles during the self-assembly process to allow photoexcitation with NIR light. The resultant nanoparticles (**141@UCNP**) display high photocytotoxicity toward HER2-overexprssing SK-OV-3 cells due to efficient production of ROS and inhibition of HER2 phosphorylation. Furthermore, the nanoparticles exhibit efficient tumor accumulation and retention in SK-OV-3 tumor-bearing mice due to both the EPR effect and specific targeting of HER2. Thus, exposure of the tumor region to NIR-light irradiation results in significant suppression of tumor growth, outperforming the nanoparticles without the HER2-targeting lapatinib units.

Weng, Li, Shen, and co-workers have utilized the nanomicelles derived from an iridium(III) PEG complex (**82c**) to encapsulate sorafenib, a multi-kinase inhibitor, for treating HCC via bimodal PDT and targeted therapy.[289] The nanomicelles gradually release sorafenib after cellular internalization and efficiently generate $^1O_2$ upon irradiation, effectively inhibiting the proliferation and migration of HCC cells and promoting their cell death through apoptosis. This synergistic approach leads to significant suppression of tumor growth in mice bearing orthotopic Huh-7 tumor xenografts. Li, Zheng, and co-workers have developed an NIR luminescent iridium(III) PEG complex (**142**) that can self-assemble into nanomicelles to encapsulate TH287, an inhibitor that targets MutT homolog 1 (MTH1), for combined PDT and targeted therapy.[290] Upon release from the nanomicelles in cells, TH287 selectively and effectively inhibits MTH1 activity, preventing the hydrolysis of 8-oxo-2′-deoxyguanosine triphosphate (8-oxo-dGTP) that is formed upon the oxidation of deoxyguanosine triphosphate by the photogenerated ROS. The increased accumulation of 8-oxo-dGTP in cells promotes its incorporation into DNA during replication, impairing DNA function and inducing cell death. Thus, treatment of 4T1 tumor-bearing mice with the TH287-loaded nanomicelles and irradiation effectively suppresses tumor growth with a TIR of 83.51%, which is substantially higher compared to the treatment involving the nanomicelles without TH287 (58.51%).

8.3. Combined PDT and Immunotherapy

Recent advances in immunotherapeutic strategies such as immune checkpoint blockade (ICB) therapy,[291] chimeric antigen receptor (CAR) T-cell therapy,[292] and cancer vaccines[293] have revolutionized cancer treatment. In particular, ICB therapy, which utilizes monoclonal antibodies or small-molecule inhibitors to block immune checkpoint proteins from interacting with their partner proteins, has demonstrated great success in the treatment of various types of cancer in clinical settings.[291] Representative examples of immune checkpoints include cytotoxic T-lymphocyte-associated antigen-4 (CTLA-4) and programmed cell death protein 1 (PD-1) expressed on T cells, where their interactions with corresponding ligands CD80/CD86 and PD-L1/PD-L2 on antigen-presenting cells are crucial to the downregulation of T cells and promotion of tumoral immune escape. However, the response rate of ICB therapy is often low in patients with cold tumors due to insufficient T cell infiltration. Since PDT can induce ICD of cancer cells and remodel the immunosuppressive TME, the combination of PDT with ICB therapy can achieve a synergistic effect in inducing significant and durable immune response against tumors.

Li, Zhang, and co-workers have utilized the nanomicelles derived from the PEG complex **142** as a carrier for loading of a non-nucleoside DNA methyltransferase inhibitor RG108 to afford a nanoagonist for pyroptosis-mediated photodynamic immunotherapy.[294] After cellular internalization, the released RG108 binds to DNA methyltransferases and reduces gasdermin E (GSDME) promoter DNA methylation, resulting in the upregulation of GSDME in cells. Upon irradiation, the complex produces $^1O_2$ and activates caspase-3, which cleaves GSDME into N-terminal (GSDME-N) and C-terminal (GSDME-C) fragments. The GSDME-N fragment perforates the plasma membrane of the cells and induces pyroptosis, releasing pro-inflammatory cytokines (e.g., IL-1β and IL-18) into the TME. This relieves the immunosuppressive TME, leading to DC maturation, cytotoxic T cell activation, and PD-1 expression enhancement in vivo. Thus, cotreatment with the PD-1 inhibitor anti-PD-1 enhances the tumoral infiltration of effector T cells, inducing potent antitumor immune response to suppress tumor growth.

Cheng, Tan, Wu, and co-workers have developed an iridium(III) complex (**143**) that targets the ER through non-covalent binding to ER-associated phospholipids and proteins.[295] Upon visible-light irradiation, the complex induces ER stress through the generation of HO$^\bullet$ and $^1O_2$, triggering ICD and upregulating PD-L1 expression in OSCC cells. Synergizing the PDT treatment with the PD-L1 inhibitor BMS-1 promotes DC maturation, T cell infiltration, cytokine secretion, and PD-L1 blockade, effectively eliciting robust antitumor immune response to inhibit oral carcinogenesis and SCC7 tumor growth in vivo.

8.4. Combined PDT and Photoactivated Chemotherapy

Photoactivated chemotherapy (PACT) represents an innovative treatment paradigm that utilizes light to activate a prodrug localized at the tumor site. In contrast to PDT that necessitates the presence of O_2, PACT operates via an O_2-independent mechanism that involves covalent or coordination bond photocleavage, making it a promising option for the treatment of hypoxic tumors. Transition metal complexes have gained significant attention for their potential as PACT agents due to their rich excited state properties.[296] Their strategic designs can integrate elements of PDT and PACT in the same molecule to produce synergistic therapeutic benefits.

8.4.1. Ruthenium(II) Complexes

Ruthenium(II) complexes have emerged as a promising class of PACT agents due to the presence of low-lying dissociative triplet metal-centered (^{3}MC) excited states that are close in energy with the ^{3}MLCT excited states.[297] Manipulation of the relative energies of the ^{3}MC and ^{3}MLCT states through ligand regulation can facilitate the thermal population of the dissociative ^{3}MC states from the ^{3}MLCT states, enabling excited state deactivation via photosubstitution reactions.

Ruthenium(II) complexes with photolabile ligands such as *cis*-$[Ru(N^N)_2(L)_2]^{2+}$ and *cis*-$[Ru(N^N)_2(L^L)]^{2+}$ can serve as photoactivatable prodrugs that, upon irradiation, generate a *bis*-aqua species that binds to DNA in a manner similar to cisplatin.[298] Dunbar, Turro, and co-workers have developed a photoactive tris-heteroleptic ruthenium(II) dppn complex (**144**) as a dual PDT and PACT agent.[299] The complex intercalates into DNA via the dppn ligand and upon irradiation, it produces two reactive species: 1) $[Ru(bpy)(dppn)(OH_2)_2]^{2+}$ that covalently binds to DNA; and 2) $^1O_2$ via the dppn-centered ^{3}IL state to trigger cancer cell death. Sun, Bonnet, and co-workers have developed a chiral ruthenium(II)–RGD peptide conjugate (**145**) as an integrin-targeting phototherapeutic prodrug for the treatment of brain tumors.[300] The cyclic metallopeptide is prepared by the direct coordination of a chiral anticancer drug *cis*-$[Ru(Ph_2\text{-}phen)_2(OH_2)_2]^{2+}$ with an RGD-containing peptide (MRGDH) through its terminal methionine and histidine residues. Owing to its amphiphilic nature, the peptide conjugate self-assembles in serum-containing media into nanoparticles. The cellular uptake of these nanoparticles is mediated by integrins $\alpha_v\beta_3$ and $\alpha_v\beta_5$, leading to their higher accumulation in U-87 MG cells that express elevated levels of integrins compared to other cancer and normal cell lines. Photoactivation of the prodrug in cells with green light generates *cis*-$[Ru(Ph_2\text{-}phen)_2(OH_2)_2]^{2+}$ that binds to proteins or DNA, forming secondary photoproducts that show strong emission and efficient ROS photosensitization. Thus, both the Λ- and Δ-isomers of the peptide conjugate display high photocytotoxic activity toward U-87 MG cells ($IC_{50,light}$ = 3.8 and 3.6 μM) and MCTSs ($IC_{50,light}$ = 7.6 and 10.9 μM). Remarkably, the conjugate efficiently accumulates in the tumor in U-87 MG tumor-bearing mice 12 h after intravenous injection due to the combined effect of passive and active targeting, and substantially inhibits tumor growth upon irradiation.

Liang, Wu, and co-workers have utilized the photosensitive ruthenium(II) scaffold *cis*-$[Ru(biq)_2(RCN)_2]^{2+}$ (biq = 2,2′-biquinoline) to develop an amphiphilic ruthenium(II)-containing triblock copolymer (**146**) as a photoactivatable prodrug.[301] The metallopolymer self-assembles into nanoparticles exhibiting long blood circulation time, high tumor accumulation, and efficient cellular uptake, facilitating the generation of cytotoxic *cis*-$[Ru(biq)_2(OH_2)_2]^{2+}$ and $^1O_2$ in cancer cells upon irradiation. The introduction of a reduction-sensitive platinum(IV) motif to the polymer backbone affords a dual-responsive bimetallic polymer (**147**) that produces cisplatin under the reductive intracellular environment of tumors.[302] The synergistic effect of cisplatin, *cis*-$[Ru(biq)_2(OH_2)_2]^{2+}$, and $^1O_2$ results in effective inhibition of the growth of cisplatin-resistant tumors in a patient-derived cancer xenograft mouse model. Zhao, Gou, and co-workers have utilized an acetazolamide-modified ruthenium(II)-containing metallopolymer (**148**) to fabricate a light-responsive nanocarrier for a hypoxia-activated prodrug (CC5) for treating hypoxic tumors via combined PDT and PACT.[303] The resultant nanoparticles (**148@CC5**) show selective tumor accumulation and retention in mice bearing MDA-MB-231 tumor xenografts due to the EPR effect and specific targeting of CA-IX overexpressed in MDA-MB-231 cells. Upon red-light irradiation, the nanoparticles generate *cis*-$[Ru(biq)_2(OH_2)_2]^{2+}$ and $^1O_2$ to kill the cancer cells; meanwhile, the photoinduced ligand dissociation leads to micelle disintegration, releasing CC5 into the tumor tissue. The released prodrug CC5 is then activated and cleaved under the hypoxic and acidic TME to produce a HIF-1α inhibitor (YC-1) and a HDAC inhibitor (CI-944) as anticancer agents. The combined effect of multiple therapeutic modalities results in effective tumor regression (TIR = 87.5%) in MDA-MB-231 tumor-bearing mice. Tang and co-workers have developed a CO/light dual-activatable ruthenium(II)-containing conjugated oligomer (**149**) as a lysosome-targeting multimodal cancer therapeutic.[304] This oligomer undergoes ligand substitution in response to endogenous CO or exogenous light irradiation. The released oligo(2,5-thiophene ethynylene) ligand not only selectively accumulates in the lysosomes and physically disrupts their integrity but also efficiently sensitizes the photogeneration of $^1O_2$ that causes severe lysosome damage. Meanwhile, the released ruthenium(II) complexes *cis*-$[Ru(biq)_2(L)_2]^{2+}$ (L = OH_2 or CO) serve as anticancer chemo- and phototherapeutics. The multiple modes of action lead to efficient killing of MDA-MB-231 cells in vitro and in vivo.

Another important class of ruthenium(II)-based PACT agents is built upon the $[Ru(tpy)(N^N)(L)]^{2+}$ scaffold (tpy = terpyridine).[305] The tridentate terpyridine ligand induces significant structural distortion of the complex, lowering the energy of the dissociative ^{3}MC state and thereby facilitating photoinduced ligand dissociation. This scaffold has been exploited as a photocaging group for bioactive molecules such as a microtubule-targeting rigidin thioether derivative[306] and the nicotinamide phosphoribosyltransferase (NAMPT) inhibitor STF-31.[307] Turro, Kodanko, and co-workers have utilized the photosensitive ruthenium(II) complex $[Ru(tpy)(Me_2\text{-}dppn)(L)]^{2+}$ (Me_2-dppn = 3,6-dimethylbenzo[*i*]dipyrido[3,2-*a*:2′,3′-*c*]phenazine) as a photocage for the inhibitors of cathepsin B (**150a**)[308] and cytochrome P450 3A4 (CYP3A4) (**150b**).[309] The incorporation of a dppn ligand imparts a long-lived ^{3}IL state for efficient $^1O_2$ photosensitization, while the addition of steric bulk to the ligand further induces structural distortion of the complex, substantially enhancing the photoinduced ligand dissociation efficiency. Thus, upon irradiation, these complexes can not only efficiently generate $^1O_2$ but also release the enzyme inhibitor to inactivate the target enzyme, resulting in significant cell death.

Wu and co-workers have utilized the $[Ru(tpy)(N^N)(L)]^{2+}$ scaffold to develop ruthenium(II)-containing block copolymers of different molecular weights (**151**) as light-responsive nanomaterials for combined PDT and PACT.[310] These metallopolymers self-assemble into different nanostructures in aqueous solutions including micelles, vesicles, and large compound micelles, depending on the chain length of the blocks. Exposure of the assemblies to red-light irradiation (656 nm) leads to the release of $[Ru(tpy)(biq)(OH_2)]^{2+}$, which displays both anticancer and $^1O_2$-photosensitization properties. Among the three assemblies, the

micelles exhibit the most efficient cellular uptake and highest photocytotoxicity in HeLa cells. A related metallopolymer containing an NIR light-responsive ruthenium(II) photocage (**152**) has also been developed.[311] The incorporation of a more π-conjugated tridentate 2,6-di(quinolin-2-yl)pyridine (dqpy) ligand and an electron-donating tetrahydrocurcumin (THC) ligand into the ruthenium(II) complex reduces the HOMO–LUMO energy gap, shifting the MLCT absorption to the NIR region. Upon irradiation with NIR light (760 nm), photoinduced ligand dissociation occurs, releasing $[Ru(dqpy)(THC)(OH_2)]^+$ that inherits the potent anticancer properties of THC and inhibits cancer cell proliferation by suppressing the mitogen-activated protein kinase signaling pathway. Owing to its amphiphilic nature, the metallopolymer self-assembles into nanoparticles, which efficiently accumulate at the tumor site of 4T1 tumor-bearing mice via the EPR effect. Subsequent exposure of the tumor region to NIR light results in substantial suppression of tumor growth due to both the release of $[Ru(dqpy)(THC)(OH_2)]^+$ and the generation of $^1O_2$ from the nanoparticles. Liang, Wu, and co-workers have designed a red light-sensitive pyrene-modified ruthenium(II) PEG complex (**153**) for combined PDT and PACT.[312] The hydrophobic pyrene moiety is introduced to endow the complex with amphiphilic properties and thereby promote its self-assembly into vesicles that efficiently circulate in the bloodstream and accumulate in the tumor. Upon exposure to red light, the PEG pendant is cleaved, inducing a morphological shift of the nanostructure from vesicles to micelles with reduced diameters and enhanced zeta potentials. This structural transformation enhances the tumor penetration and cellular internalization of $[Ru(tpy)(biq)(OH_2)]^{2+}$. Subsequent exposure to the second dose of red light triggers the generation of $^1O_2$, leading to the efficient eradication of cancer cells in vivo. Wei, Li, Sun, and co-workers have developed a red light-activatable metallopolymer (**154**), where both the ruthenium(II) complex and PTX are conjugated to the polymer backbone via a $^1O_2$-cleavable aminoacrylate linker, for combined PDT and PACT.[313] Exposure of the self-assembled nanoparticles accumulated at the tumors to red light results in the release of $[Ru(tpy)(biq)(OH_2)]^{2+}$ and the production of $^1O_2$, which cleaves the aminoacrylate linker to release PTX. This sequential dual-release approach allows for the on-demand release of therapeutic agents at the tumor site while minimizing drug leakage at off-target sites, enabling the effective inhibition of tumor growth in vivo without causing systemic toxicity.

8.4.2. Platinum(IV) Complexes

Diazido platinum(IV) complexes represent another important class of PACT agents used for cancer therapy.[314] These complexes can be reduced upon irradiation to release cytotoxic platinum(II) species, azidyl radicals, and ROS to induce cell death.

Shi, Sicilia, Huang, Sadler, and co-workers have developed a bimetallic iridium(III)–platinum(IV) complex (**155**) for combined PDT and PACT.[315] The conjugation of an iridium(III)-based photosensitizer with a diazido platinum(IV) prodrug allows for charge-transfer to occur between the two entities, facilitating the photoactivation of the platinum(IV) complex. Thus, upon photoexcitation, the complex undergoes more rapid photodecomposition than the parent diazido platinum(IV) prodrug, efficiently producing the active platinum(II) species and azidyl radicals. Additionally, the complex can generate $^1O_2$ and oxidize NADH to NAD$^\bullet$ and NAD^+ upon irradiation due to the photoactive iridium(III)-based excited states. The synergistic action between the two subunits leads to more potent photocytotoxic activity toward cancer cells (A2780, A549, and PC-3; $IC_{50,light}$ = 1.3–9.7 μM) compared to the individual mononuclear complexes or their simple mixture. Studies on the mechanism of action indicate that upon irradiation, the released radicals and ROS induce nuclear membrane rupture, facilitating the photogenerated platinum(II) species to bind to DNA and induce cell death. Synchrotron X-ray fluorescence (SXRF) imaging of iridium and platinum in the treated cells reveals that the intracellular platinum content is ca. 4-fold higher compared to iridium, with the iridium signal partially confined to small compartments such as lysosomes, suggestive of the cleavage of the complex inside cells and excretion of the iridium(III) fragment via recycling vesicles. Bradley and co-workers have designed a mitochondria-targeting ruthenium(II) complex (**156a**) that can function as both a photosensitizer for $^1O_2$ generation and a photocatalyst for platinum(IV) prodrug (**156b**) activation.[316] Cotreatment with the ruthenium(II) complex and the platinum(IV) prodrug followed by light irradiation results in significant cell death in both wild-type SK-OV-3 cells and oxaliplatin-resistant SK-OV-3-OxR cells, indicating that the dual mode of action can overcome drug resistance.

8.4.3. Iridium(III) and Gold(III) Complexes

In addition to ruthenium(II) and platinum(IV) complexes, various other transition metal complexes have been designed as PACT agents. For example, iridium(III) PEG complexes incorporating a photolabile 2-nitrobenzyl linkage have been developed as PACT agents, exhibiting photocytotoxicity upon photoinduced release of the biocompatible PEG pendants.[317] Cyclometalated gold(III) complexes bearing a hydride or alkyl ligand have also been developed as PACT agents, showing potent photoinduced thiol reactivity to inhibit thiol-containing enzymes.[318]

Gasser, Chao, and co-workers have designed an iridium(III) complex functionalized with an anthracene endoperoxide moiety (**157**) as a two-photon-activatable prodrug for combined PDT and PACT.[319] Exposure of the complex to light irradiation triggers the cleavage of the O–O bond of endoperoxide, which not only releases $^1O_2$ but also generates a highly cytotoxic iridium(III) anthracene complex and an alkoxy radical. As a result, the complex displays very high photocytotoxic activity toward hypoxic A549 cells and MCTSs ($IC_{50,light}$ = 60 and 730 nM, respectively). Mechanistic studies show that the endoperoxide complex is specifically enriched in the mitochondria and, upon irradiation, converted to its anthracene counterpart concomitant with the generation of ROS, inducing significant mitochondrial shrinkage and MMP reduction. The complex has been encapsulated into DSPE-PEG-biotin to afford nanoparticles (**PM-Biotin@157**) that exhibit increased blood circulation time and efficient tumor accumulation in A549 tumor-bearing mice, enabling almost complete tumor ablation with a single dose of NIR light (750 nm).

Zou and co-workers have designed a cyclometalated gold(III) complex (**158**) that can function as both a photosensitizer and a photocatalytic substrate for combined PDT and PACT.[320] This

complex possesses a long-lived ^{3}ILCT state (τ_o = 101 μs), which enables efficient photosensitization of ROS under aerated conditions. However, upon O_2 depletion, the complex undergoes efficient photoreduction, releasing the blue fluorescent bidentate ligand and a thiol-reactive gold(I) species that can inhibit thioredoxin reductase, an enzyme that is crucial for regulating cellular redox homeostasis and is overexpressed in various cancer cells. This O_2-dependent conditional photoactivity leads to a paradigm shift from PDT to PACT in response to the O_2 content in tumor tissues, resulting in high photocytotoxicity toward cancer cells (A375, A549, human colorectal carcinoma HCT116, and HepG2) under both normoxia and hypoxia ($IC_{50,light}$ = 0.47–1.23 and 1.85–5.08 μM, respectively). Notably, the photoreduction of complex **158** can be catalyzed by external photosensitizers such as riboflavin. Since riboflavin is an endogenous photosensitizer and its transporters are often overexpressed in melanoma cells, treatment of A375 tumor-bearing mice with the complex followed by irradiation at 465 nm, the excitation wavelength for riboflavin but not the complex, leads to selective and significant inhibition of tumor growth with a TIR of 92%.

8.5. Combined PDT and Photothermal Therapy

Photothermal therapy (PTT) has emerged as a promising alternative to PDT for the treatment of cancer.[321] This approach utilizes a photothermal transduction agent (PTA) that converts light into heat through vibrational relaxation upon returning to the ground state. The increase in local temperature leads to cell death through plasma membrane destruction and protein denaturation. Notably, the localized heat generation can also accelerate local blood flow and increase the O_2 concentration in tumor tissues, sensitizing the tumor to PDT. Thus, the combination of PDT and PTT holds significant potential for combating tumors, particularly large solid tumors characterized by a hypoxic TME.

Various NIR-absorbing organic molecules such as cyanines, diketopyrrolopyrroles, and porphyrins have been developed as PTAs for PTT.[322] Deng, Chen, Sun, and co-workers have designed a far-red/NIR-absorbing neutral iridium(III) complex bearing a distyryl-BODIPY pendant (**159**) for combined PDT and PTT.[323] The introduction of a distyryl-BODIPY motif to the iridium(III) complex enhances its absorption in the NIR region (λ_{abs} = 685 nm) and imparts a long-lived BODIPY-centered ^{3}IL state (τ_o = 9.78 μs), allowing efficient $^1O_2$ and heat generation upon NIR-light irradiation. The complex has been encapsulated into micelles (**PM@159**) to enhance its water solubility and tumor retention while retaining its high $^1O_2$ photosensitization (Φ_Δ = 0.53) and photothermal conversion efficiency (η_T = 0.30). These remarkable properties result in complete tumor ablation and effective tumor metastasis inhibition in mice bearing orthotopic 4T1 tumors upon irradiation at 660 nm. Liu, Zhao, and co-workers have developed three NIR-absorbing azadipyrromethene-based platinum(II) complexes (**160**) for combined PDT and PTT.[324] These complexes are designed based on two rationales: 1) the direct chelation of the platinum(II) ion to the azadipyrromethene scaffold promotes singlet-to-triplet transition via ISC, enabling efficient ROS photosensitization; 2) the strong intramolecular PET from the dimethylamine moiety (electron donor) to the azadipyrromethene core (electron acceptor) facilitates excited state relaxation via non-radiative decay for boosting photothermal conversion, resulting in a strong photothermal effect. These complexes show strong absorption in the NIR region (λ_{abs} = 693–717 nm), allowing efficient generation of $^1O_2$ and heat upon irradiation with a 690-nm laser. Complex **160a** has been encapsulated into DSPE-PEG to afford water-soluble and biocompatible nanoparticles (**PM@160a**) that display high tumor retention and efficient $^1O_2$ photosensitization and photothermal conversion upon irradiation with NIR light (730 nm), leading to complete tumor ablation in vivo with negligible side effects. A related platinum(II) complex (**161**) has also been developed as a bimodal phototherapeutic agent.[325] The diiodination of the azadipyrromethene skeleton further promotes ISC and non-radiative relaxation processes, boosting the generation of $^1O_2$ (Φ_Δ = 0.53) and the conversion of light into heat (η_T = 0.306). Encapsultion of the complex into DSPE-PEG affords water-soluble nanoparticles (**PM@161**) with high $^1O_2$ generation and photothermal conversion efficiencies. As revealed by PAI, the nanoparticles accumulate in the tumor 4 h after intravenous injection, enabling image-guided PDT–PTT to inhibit tumor growth in vivo.

Zhao, Xu, Gou, and co-workers have designed an iridium(III) complex incorporating a donor–acceptor–donor (D–A–D) type chromophoric ligand (**162a**) for NIR light-mediated PDT and PTT.[326] The strong intramolecular charge-transfer from [1,2,5]thiadiazolo-[3,4-*i*]dipyrido[*a*,*c*]phenazine (electron donor) to triphenylamine (electron acceptor) results in intense NIR absorption ($\varepsilon_{716\,nm} = 9.0 \times 10^3$ M^{-1} cm^{-1}) and efficient photothermal conversion (η_T = 0.275). Additionally, the coordination of the octahedral iridium(III) complex to the D–A–D chromophore favors the formation of J-aggregates in aqueous solutions, which not only induces a significant red shift in the absorption to longer wavelengths (λ_{abs} = 814 nm) but also facilitates ROS photosensitization through a Type I process. To enhance its water solubility and biocompatibility, the complex has been modified with PEG pendants to yield an amphiphilic polymer (**162b**), which self-assembles into polymeric micelles with a core–shell nanostructure. These micellar nanoparticles exhibit preferential tumor accumulation and efficient ROS ($HO^•$ and $O_2^{•-}$) and heat generation upon irradiation at 808 nm, leading to significant tumor regression (TIR = 96%) with a cure rate of 67% in A549 tumor-bearing mice. A related ruthenium(II) complex (**163**) has been mixed with a self-assembling diphenylalanine peptide to construct a supramolecular photosensitizer for combined PDT and PTT.[327] The coassembly of the ruthenium(II) complex with the diphenylalanine peptide induces J-aggregation, resulting in red-shifted absorption (from 713 to 790 nm) and enhanced ROS and heat generation. The resultant nanoparticles (**163-FF**) show efficient tumor accumulation and penetration in vivo, enabling effective inhibition of tumor growth (TIR = 95.3%) in A549 tumor-bearing mice upon irradiation at 808 nm. Furthermore, matrix-assisted laser desorption/ionization mass spectrometry imaging (MALDI-MSI) has been used to gain insights into the biochemical response of the tumor tissues to the treatment, revealing alternations in the phospholipid composition of cancer cells and the release of heme *b* from damaged blood cells.

Sun, Li, and co-workers have developed dual-light-activatable nanomicelles using an amphiphilic iridium(III) PEG complex

(**164a**) and a zinc(II) phthalocyanine derivative (**164b**) for combined PDT and PTT.[328] Similar to the aforementioned iridium(III) PEG complexes, the hydrophilic PEG pendant of complex **164a** aids in nanomicelle formation, while the two hydrophobic chains enhance the loading of complex **164b** through hydrophobic interaction. The resultant nanomicelles (**164a@164b**) efficiently generate $^1O_2$ (Φ_Δ = 0.13) and heat (η_T = 0.468) upon irradiation at 532 and 730 nm, respectively. In vivo and ex vivo luminescence imaging shows that the nanomicelles display long blood circulation ($t_{1/2}$ = 9.33 h) and efficient tumor accumulation in 4T1.2 tumor-bearing mice at 24 and 48 h postinjection. Additionally, photothermal imaging (PTI) conducted at 24 h after injection reveals that the nanomicelles induce a substantial temperature increase (16.8 °C) in the tumors upon exposure to NIR light. Remarkably, irradiation of the tumors with 532-nm and 730-nm light reduces the tumor volume by 83.2%.

Various organic and inorganic nanomaterials such as carbon-based (e.g., graphene and carbon nanotube) and metal-based nanomaterials (e.g., noble metal materials) have been developed as PTAs for PTT.[329] Tan, Mao, and co-workers have loaded a ruthenium(II) PEG complex (**165**) onto reduced graphene oxide (rGO) sheets for lysosome-targeted imaging and combined PDT and PTT.[330] The release of the complex from the rGO sheets is pH-dependent and accelerated under acidic conditions (pH = 5) due to the protonation/deprotonation of carboxyl groups on rGO sheets. Upon cellular uptake, the nanohybrid (**rGO@165**) is enriched in the acidic lysosomes, facilitating the release of the complex from the surface of rGO sheets. Sequential exposure of the treated cells to irradiation with an 808-nm laser and a 450-nm laser leads to the efficient generation of heat and $^1O_2$, respectively, inducing apoptosis through causing lysosomal damage. Remarkably, the combined PDT–PTT treatment results in more significant inhibition of tumor growth in A549 tumor-bearing mice than PDT or PTT treatment alone. Additionally, the nanohybrid can be used for PTI, offering opportunities for image-guided PDT–PTT and for real-time monitoring of the treatment outcomes. Chao and co-workers have functionalized single-walled carbon nanotubes (SWCNTs) with two-photon-active ruthenium(II) complexes (**166**) for bimodal PDT and PTT.[331] Upon irradiation with an 808-nm laser, **SWCNT@166a** and **SWCNT@166b** exhibit strong photothermal effects (η_T = 0.394 and 0.383, respectively), which trigger the release of the ruthenium(II) complexes from the SWCNTs. The released complexes can then sensitize $^1O_2$ generation due to their strong TPA ($\delta_{808\ nm}$ = 494 and 428 GM). The treatment enables efficient cancer cell death in both 2D and 3D cell cultures and significant tumor ablation in tumor-bearing mice upon exposure to a single dose of NIR-light irradiation. In vivo PTI shows that the temperature of the tumor tissue rapidly increases from 36.5 to 62.8 °C (**SWCNT@166a**) or 59.5 °C (**SWCNT@166b**) in 5 min upon irradiation.

Tan, Mao, and co-workers have utilized platinum polydopamine (PtPDA) nanoparticles to develop a multifunctional nanoplatform for remodeling the TME and for combined PDT and PTT.[332] The PtPDA nanoparticles can: 1) catalyze the decomposition of H_2O_2 to produce O_2 and 2) induce vasodilation by the photothermal effect to increase O_2 supply. These nanoparticles are modified with CD moieties at the surface for loading of a ruthenium(II)-based photosensitizer (**167**) through host–guest interaction. The complex can be released from the nanoparticles in response to the low pH and high H_2O_2 levels of the TME and upon photothermal heating. Once released, the complex can catalyze the photo-Fenton reaction and photosensitize $^1O_2$ generation. In vivo biodistribution studies show that the ruthenium(II)-loaded nanoparticles (**PtPDA-CD@167**) efficiently accumulate in the tumor tissue of 4T1 tumor-bearing mice following either intratumoral or intravenous injection (**Figure 15a**). Notably, these nanoparticles can function as a multimodal imaging probe for real-time monitoring of pathological changes in the tumor tissue via PTI, PAI, and computed tomography (CT) imaging (Figure 15b–d), offering opportunities for tumor diagnosis and image-guided PDT and PTT in vivo. Importantly, the nanoparticles can remodel the TME by alleviating tumor hypoxia and inhibiting angiogenesis, and induce significant tumor ablation upon sequential irradiation with a 450-nm and 808 nm laser without causing significant systemic toxicity (Figure 15e–i).

Transition metal complexes have also been developed as dual PDT and PTT agents by modulating their excited state deactivation pathways. Gao and co-workers have designed a series of dinuclear ruthenium(II) complexes (**168**) with large TPA cross-sections in the range of 800–900 nm for PDT and PTT using an 808-nm low-power laser.[333] These complexes feature: 1) the incorporation of a highly π-conjugated bridging ligand to impart low-lying triplet states for $^1O_2$ photosensitization, and 2) the introduction of rotatable substituents on the ancillary ligands to facilitate non-radiative relaxations for heat generation. Among these complexes, the amphiphilic complex **168c** shows balanced $^1O_2$ photosensitization (Φ_Δ = 0.035) and photothermal conversion (η_T = 0.173) upon photoexcitation at 808 nm. This complex displays high photocytotoxic activity toward A375 cells ($IC_{50,light}$ = 31.0 nM), enabling the effective suppression of tumor growth in A375 tumor-bearing mice (TIR = 90%) upon exposure to an 808-nm low-power laser (30 J cm^{-2}). Gao and co-workers have also designed a series of iridium(III) complexes appended with a morpholine or piperazine pendant (**169**) as dual PDT and PTT agents.[334] These complexes efficiently generate $^1O_2$ (Φ_Δ = 0.026–0.110) and heat (η_T = 0.17–0.18) upon photoexcitation at 808 nm. Among them, complex **169e** exhibits the highest cellular uptake and rapid accumulation in the mitochondria of A375 cells and induces cell death through caspase-mediated apoptosis upon irradiation. Importantly, the complex can substantially inhibit tumor growth in A375 tumor-bearing mice upon irradiation with an 808-nm low-power laser, with minimal hepato-/nephrotoxicity and efficient clearance from the bodies after the treatment. Ren, Gao, and co-workers have developed a series of bithiophene-functionalized ruthenium(II), osmium(II), and iridium(III) complexes (**170**) as single-molecular platforms for multimodal therapy.[335] All the complexes show strong TPA at 808 nm and remarkable $O_2^{\bullet-}$ and $^1O_2$ production and heat generation upon irradiation. Notably, complex **170g** is internalized into cells via macropinocytosis and localized in both the mitochondria and nucleus. The dual-organelle targeting capability of the complex enables inhibition of cancer cell proliferation through topoisomerase and RNA polymerase inhibition, alongside apoptosis and ferroptosis induced by photogenerated ROS and heat. As a result, complex **170g** displays high photocytotoxicity toward both A375, A549, and A549/DDP cells

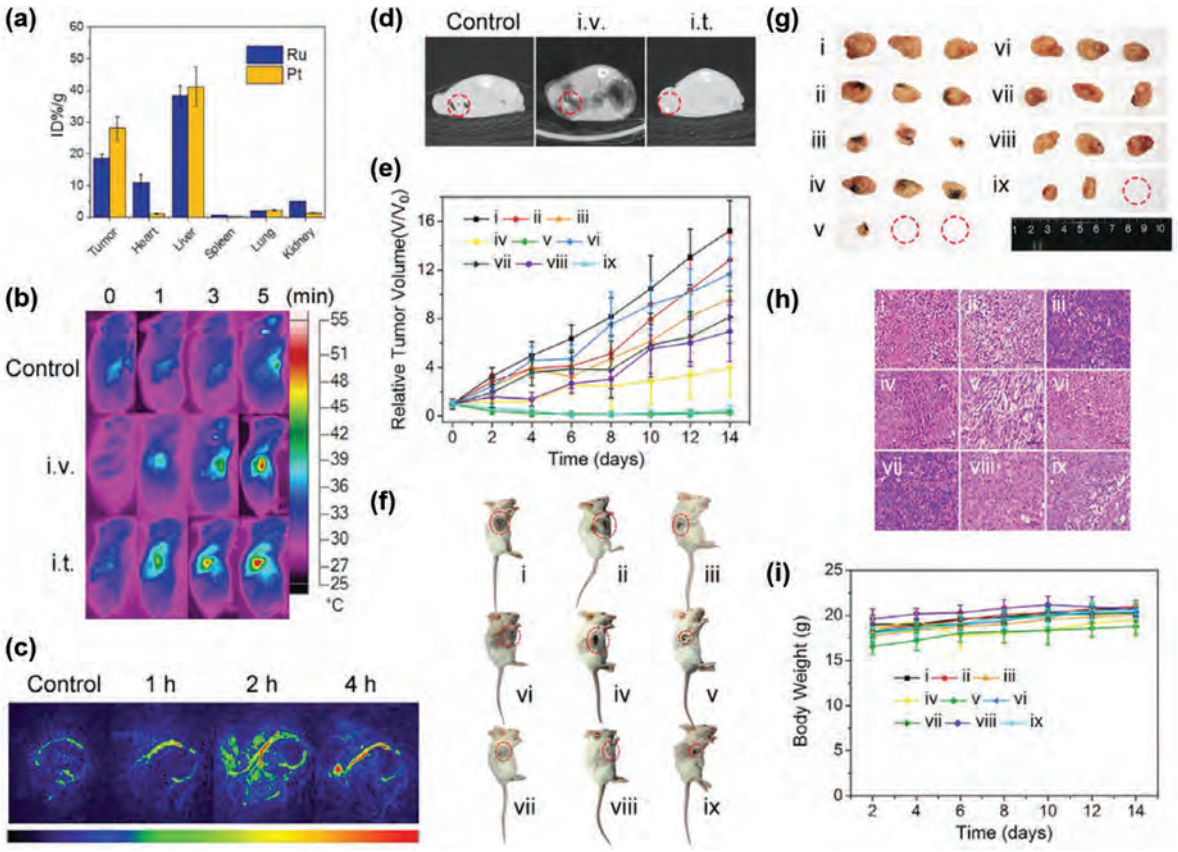

Figure 15. a) Ruthenium and platinum concentration in different organs of 4T1 tumor-bearing mice 24 h after intravenous injection of **PtPDA-CD@167** (1 mg mL^{-1}, 200 µL) ($n = 3$). b) In vivo thermal images of 4T1 tumor-bearing mice administrated with **PtPDA-CD@167** (1 mg mL^{-1}, 200 µL, 4 h) through intravenous (i.v.) or intratumoral (i.t.) injection and exposed to an 808-nm laser (1 W cm^{-2}) for 0, 1, 3, and 5 min. c) In vivo PA images of 4T1 tumor-bearing mice administrated with **PtPDA-CD@167** (1 mg mL^{-1}, 200 µL) through i.v. injection. The images were taken at 1, 2, and 4 h postinjection. d) In vivo CT images of 4T1 tumor-bearing mice administrated with **PtPDA-CD@167** (5 mg mL^{-1}, 100 µL) through i.v. or i.t. injection. The images were taken 2 h after i.v. injection and 30 min after i.t. injection. e) Tumor growth curves of 4T1 tumor-bearing mice under different treatments ($n = 5$). f) Representative photographs of 4T1 tumor-bearing mice after different treatments. The tumor sites are marked with red dashed circles. g) Representative photographs of tumors dissected from 4T1 tumor-bearing mice after different treatments. The red dashed circles represent tumors that completely disappear. h) H&E staining images of tumor tissues harvested from 4T1 tumor-bearing mice after different treatments. i) Body weight of 4T1 tumor-bearing mice under different treatments. Group i: control; ii: **PtPDA-CD@167** (i.t. injection); iii: **PtPDA-CD@167** (i.t. injection) + PDT; iv: **PtPDA-CD@167** (i.t. injection) + PTT; v: **PtPDA-CD@167** (i.t. injection) + PDT and PTT; vi: **PtPDA-CD@167** (i.v. injection); vii: **PtPDA-CD@167** (i.v. injection) + PDT; viii: **PtPDA-CD@167** (i.v. injection) + PTT; ix: **PtPDA-CD@167** (i.v. injection) + PDT and PTT. Control: saline; **PtPDA-CD@167**: 1 mg mL^{-1}, 200 µL; PDT: 450 nm, 12 W cm^{-2}, 5 min; PTT: 808 nm, 1 W cm^{-2}, 3 min. Reproduced with permission.[332] Copyright 2020 Wiley-VCH.

($IC_{50,light}$ = 152, 155, and 41.6 nM, respectively) upon irradiation with an 808-nm low-power laser. Treatment of mice bearing A375 or A549/DDP tumor xenografts with the complex and light leads to signification tumor regression with a TIR of up to 93% and a survival rate of up to 100%.

8.6. Discussion

The combination of PDT with other O_2-independent therapeutic approaches such as chemotherapy, targeted therapy, immunotherapy, PACT, and PTT has opened up opportunities to harness the strengths of individual treatments while mitigating their limitations, leading to additive or even synergistic therapeutic effects in cancer treatment. Furthermore, combination therapy can overcome treatment resistance due to the distinct mechanisms of action of various therapeutic modalities, reducing the likelihood of tumor recurrence and metastasis. While these combinational approaches show promise in combating cancer, other therapeutic modalities such as radiotherapy, chemodynamic therapy, sonodynamic therapy, gene therapy, and magnetic hyperthermia therapy that can also be used in conjunction with PDT to enhance therapeutic outcomes. In particular, gene therapy has emerged as a promising treatment option for various inherited and acquired human diseases.[336] Recent advancements in clustered regularly interspaced palindromic repeats (CRISPR)/CRISPR-associated protein 9 (Cas9) technology have offered a precise and efficient genome engineering tool that enables the permanent correction of deleterious mutations, removal of disease-causing genes, or addition of therapeutic genes to specific sites in the genome, offering new avenues for disease treatment.[337] The use of CRISPR/Cas9 systems to

target genes associated with, for example, HIF-1α and PD-L1 expression in cancer cells is anticipated to reshape the hypoxic and immunosuppressive TME, enhancing the effectiveness of PDT. Nanotechnology has played a crucial role in combination therapy as it offers a versatile platform for integrating various therapeutic agents in a personalized manner.[338] However, it is challenging to control the growth of nanoparticles during large-scale production. Batch-to-batch variations in drug concentration, pharmacokinetic profiles, and drug release among the particles can lead to inconsistent therapeutic outcomes. An alternative approach is to develop multimodal therapeutic agents based on single small molecules with well-defined structures, which will enable precise control over their physiochemical, pharmacokinetic, and pharmacodynamic properties and thus enhanced therapeutic effects.

9. Conclusion and Perspectives

Photofunctional transition metal complexes have gained significant attention as photosensitizers for PDT applications due to their unique photophysical and photochemical properties. While these complexes have shown great promise in treating superficial tumors in clinical settings, their use for treating deep-seated and large solid tumors faces significant challenges. One primary obstacle is the low O_2 concentration in the hypoxic TME, which hampers the production of ROS. Therefore, it is crucial to shift the PDT paradigm from the predominantly O_2-dependent Type II mechanism to the less O_2-dependent Type I mechanism and explore O_2-independent photoredox catalysis. Integrating transition metal complexes with nanomaterials can give rise to innovative PDT agents that are capable of remodeling the TME and alleviating hypoxia, enabling sustainable ROS generation. Additionally, combining PDT with other O_2-independent therapeutic modalities, such as chemotherapy, PACT, and PTT, can improve therapeutic outcomes. Another obstacle is the limited light penetration in deep biological tissues, which reduces the effectiveness of PDT in treating deep-seated tumors. To overcome this limitation, one solution is to enhance the one- and two-photon absorption of transition metal complexes in the NIR region. This approach would allow the complexes to harness long-wavelength light for excitation, enabling deeper tissue penetration. Furthermore, the inadequate accumulation of complexes at the tumor site poses a significant hurdle. To achieve selective tumor accumulation in vivo, transition metal complexes can be formulated into nanomaterials for passive targeting and conjugated to biomolecules such as sugars, vitamins, peptides, antibodies, and aptamers for active targeting. An alternative approach involves the construction of activatable transition metal complexes that display emission and ROS-photosensitization turn-on in response to specific tumor-associated stimuli such as pH, ROS/GSH, and enzyme activity, enhancing the precision of PDT and minimizing damage to normal tissues.

While these strategies can enhance the effectiveness of PDT in treating deep-seated or large solid tumors, challenges persist in the treatment of metastatic cancer due to the localized nature of PDT. Although PDT can trigger antitumor immune response, its effect is often weak and short-acting due to the immunosuppressive TME, rendering it insufficient to control tumor metastasis and recurrence. Thus, it is imperative to develop new strategies that can broaden the scope of PDT to encompass metastatic tumors. One promising approach involves the development of innovative photosensitizers capable of inducing ICD, which can remodel the immunosuppressive TME to elicit potent and durable antitumor immune response, inhibiting the growth of both primary and metastatic tumors. The development of transition metal complexes as ICD photoinducers is still in its infancy.[339] Since ROS-mediated ER stress plays a key role in ICD induction, developing transition metal complexes with dual cancer- and ER-targeting capabilities is instrumental in achieving focused ROS-mediated ER stress in cancer cells and efficient ICD induction. Another promising approach is to design self-illuminating systems that utilize chemiluminescent agents as an internal excitation source to activate transition metal complexes for ROS photosensitization. The use of chemiluminescent agents for excitation can overcome the limitations associated with external excitation sources in traditional PDT, allowing the effective destruction of cancer cells regardless of their location. Furthermore, the intrinsic stimuli-responsiveness of chemiluminescent agents can be leveraged to differentiate tumor and normal tissues by targeting specific cancer biomarkers. This area remains unexplored and presents an interesting avenue for future research.

Although transition metal complexes exhibit significant potential in the development of PDT agents, systemic studies on their structure–activity relationships are still limited compared to organic photosensitizers. The limited understanding of the structure–activity relationships governing these complexes hinders the rational design of transition metal complexes as more effective PDT agents. Given the high structural diversity and synthetic versatility of transition metal complexes, large libraries of complexes can be generated using a combinatorial approach, which would facilitate the elucidation of the structure–activity relationships of transition metal complexes and enable the high-throughput screening for promising leads. A combinatorial, semi-automated, and high-throughput approach has recently been utilized to construct a small library of iridium(III) complexes and to determine their structure–activity relationships with the aid of DFT calculations.[340] This method has led to the identification of a complex showing minimal dark cytotoxicity but potent photocytotoxic activity in the nanomolar concentration range, demonstrating significant potential as a PDT agent. Recent advancements in machine learning techniques are poised to provide cutting-edge computational tools that can aid in establishing the structure–activity relationships of transition metal complexes based on existing literature and experimental data, offering new insights to guide the design of novel complexes. The precise prediction of the photophysical, photochemical, and photobiological properties of transition metal complexes is expected to accelerate the development of effective PDT agents for clinical applications.

In conclusion, photofunctional transition metal complexes hold significant promise for PDT applications, offering exciting prospects for developing innovative cancer phototherapeutics. Further research and advancements in their design will overcome current challenges, improve their effectiveness in treating cancers, and facilitate their successful translation from bench to bedside.

Supporting Information

Supporting Information is available from the Wiley Online Library or from the author.

Acknowledgements

The authors thank the Hong Kong Research Grants Council (Project No. CityU 11301121, CityU 11317022, CityU 11309423, and C7075-21GF) and the Hong Kong Research Grants Council and National Natural Science Foundation of China (Project No. N_CityU104/21) for financial support. The authors also thank the funding support from "Laboratory for Synthetic Chemistry and Chemical Biology" under the Health@InnoHK Program launched by Innovation and Technology Commission, The Government of Hong Kong SAR, P. R. China.

Conflict of Interest

The authors declare no conflict of interest.

Keywords

photodynamic therapy, photosensitizer, theranostic, therapeutic, transition metal complex

Received: April 19, 2024
Revised: August 3, 2024
Published online: September 25, 2024

[1] F. Bray, M. Laversanne, H. Sung, J. Ferlay, R. L. Siegel, I. Soerjomataram, A. Jemal, *CA Cancer J. Clin.* **2024**, *74*, 229.
[2] S. Tohme, R. L. Simmons, A. Tsung, *Cancer Res.* **2017**, *77*, 1548.
[3] a) H. E. Barker, J. T. E. Paget, A. A. Khan, K. J. Harrington, *Nat. Rev. Cancer* **2015**, *15*, 409; b) C. Holohan, S. Van Schaeybroeck, D. B. Longley, P. G. Johnston, *Nat. Rev. Cancer* **2013**, *13*, 714.
[4] A. D. Waldman, J. M. Fritz, M. J. Lenardo, *Nat. Rev. Immunol.* **2020**, *20*, 651.
[5] D. E. J. G. J. Dolmans, D. Fukumura, R. K. Jain, *Nat. Rev. Cancer* **2003**, *3*, 380.
[6] A. E. O'Connor, W. M. Gallagher, A. T. Byrne, *Photochem. Photobiol.* **2009**, *85*, 1053.
[7] a) L. K. McKenzie, H. E. Bryant, J. A. Weinstein, *Coord. Chem. Rev.* **2019**, *379*, 2; b) C. Imberti, P. Zhang, H. Huang, P. J. Sadler, *Angew. Chem., Int. Ed.* **2020**, *59*, 61; c) Y. Wu, S. Li, Y. Chen, W. He, Z. Guo, *Chem. Sci.* **2022**, *13*, 5085; d) B. Kar, U. Das, N. Roy, P. Paira, *Coord. Chem. Rev.* **2023**, *474*, 214860; e) F. Wei, Z. Chen, X.-C. Shen, L. Ji, H. Chao, *Chem. Commun.* **2023**, *59*, 6956.
[8] K. Y. Zhang, Q. Yu, H. Wei, S. Liu, Q. Zhao, W. Huang, *Chem. Rev.* **2018**, *118*, 1770.
[9] S. Monro, K. L. Colón, H. Yin, J. Roque III, P. Konda, S. Gujar, R. P. Thummel, L. Lilge, C. G. Cameron, S. A. McFarland, *Chem. Rev.* **2019**, *119*, 797.
[10] Q. Yao, J. Fan, S. Long, X. Zhao, H. Li, J. Du, K. Shao, X. Peng, *Chem* **2022**, *8*, 197.
[11] P. R. Ogilby, *Chem. Soc. Rev.* **2010**, *39*, 3181.
[12] X. Zhang, Y. Hou, X. Xiao, X. Chen, M. Hu, X. Geng, Z. Wang, J. Zhao, *Coord. Chem. Rev.* **2020**, *417*, 213371.
[13] a) J. Fong, K. Kasimova, Y. Arenas, P. Kaspler, S. Lazic, A. Mandel, L. Lilge, *Photochem. Photobiol. Sci.* **2015**, *14*, 2014; b) Q. Chen, V. Ramu, Y. Aydar, A. Groenewoud, X.-Q. Zhou, M. J. Jager, H. Cole, C. G. Cameron, S. A. McFarland, S. Bonnet, B. E. Snaar-Jagalska, *Cancers* **2020**, *12*, 587; c) S. Chamberlain, H. D. Cole, J. Roque III, D. Bellnier, S. A. McFarland, G. Shafirstein, *Pharmaceuticals* **2020**, *13*, 137.
[14] a) A. Chettri, J. A. Roque III, K. R. A. Schneider, H. D. Cole, C. G. Cameron, S. A. McFarland, B. Dietzek, *ChemPhotoChem* **2021**, *5*, 421; b) A. Chettri, K. R. A. Schneider, H. D. Cole, J. A. Roque III, C. G. Cameron, S. A. McFarland, B. Dietzek, *J. Phys. Chem. A* **2021**, *125*, 6985.
[15] a) A. Chettri, H. D. Cole, J. A. Roque III, K. R. A. Schneider, T. Yang, C. G. Cameron, S. A. McFarland, B. Dietzek-Ivanšić, *J. Phys. Chem. A* **2022**, *126*, 1336; b) A. Chettri, T. Yang, H. D. Cole, G. Shi, C. G. Cameron, S. A. McFarland, B. Dietzek-Ivanšić, *Angew. Chem., Int. Ed.* **2023**, *62*, e202301452.
[16] a) T. Sainuddin, M. Pinto, H. Yin, M. Hetu, J. Colpitts, S. A. McFarland, *J. Inorg. Biochem.* **2016**, *158*, 45; b) J. A. Roque III, H. D. Cole, P. C. Barrett, L. M. Lifshits, R. O. Hodges, S. Kim, G. Deep, A. Francés-Monerris, M. E. Alberto, C. G. Cameron, S. A. McFarland, *J. Am. Chem. Soc.* **2022**, *144*, 8317; c) H. D. Cole, J. A. Roque III, G. Shi, L. M. Lifshits, E. Ramasamy, P. C. Barrett, R. O. Hodges, C. G. Cameron, S. A. McFarland, *J. Am. Chem. Soc.* **2022**, *144*, 9543; d) H. D. Cole, A. Vali, J. A. Roque III, G. Shi, G. Kaur, R. O. Hodges, A. Francés-Monerris, M. E. Alberto, C. G. Cameron, S. A. McFarland, *Inorg. Chem.* **2023**, *62*, 21181; e) H. D. Cole, A. Vali, J. A. Roque III, G. Shi, A. Talgatov, G. Kaur, A. Francés-Monerris, M. E. Alberto, C. G. Cameron, S. A. McFarland, *Inorg. Chem.* **2024**, *63*, 9735.
[17] W. Wang, L. Wang, Y. Zhang, Y. Shi, R. Zhang, L. Chen, Z. Shi, S. Yuan, X. Li, C. He, X. Li, *Inorg. Chem.* **2024**, *63*, 7792.
[18] a) S. Monro, J. Scott, A. Chouai, R. Lincoln, R. Zong, R. P. Thummel, S. A. McFarland, *Inorg. Chem.* **2010**, *49*, 2889; b) R. Lincoln, L. Kohler, S. Monro, H. Yin, M. Stephenson, R. Zong, A. Chouai, C. Dorsey, R. Hennigar, R. P. Thummel, S. A. McFarland, *J. Am. Chem. Soc.* **2013**, *135*, 17161.
[19] D. A. Smithen, S. Monro, M. Pinto, J. Roque III, R. M. Diaz-Rodriguez, H. Yin, C. G. Cameron, A. Thompson, S. A. McFarland, *Chem. Sci.* **2020**, *11*, 12047.
[20] C. Liu, L. Zhou, F. Wei, L. Li, S. Zhao, P. Gong, L. Cai, K. M.-C. Wong, *ACS Appl. Mater. Interfaces* **2019**, *11*, 8797.
[21] L. Zhou, F. Wei, J. Xiang, H. Li, C. Li, P. Zhang, C. Liu, P. Gong, L. Cai, K. M.-C. Wong, *Chem. Sci.* **2020**, *11*, 12212.
[22] F. Wei, F. Chen, S. Wu, M. Zha, J. Liu, K.-L. Wong, K. Li, K. M.-C. Wong, *Inorg. Chem.* **2024**, *63*, 5872.
[23] H. Yin, M. Stephenson, J. Gibson, E. Sampson, G. Shi, T. Sainuddin, S. Monro, S. A. McFarland, *Inorg. Chem.* **2014**, *53*, 4548.
[24] H. K. Saeed, P. J. Jarman, S. Archer, S. Sreedharan, I. Q. Saeed, L. K. Mckenzie, J. A. Weinstein, N. J. Buurma, C. G. W. Smythe, J. A. Thomas, *Angew. Chem., Int. Ed.* **2017**, *56*, 12628.
[25] G. Li, D. Zhu, X. Wang, Z. Su, M. R. Bryce, *Chem. Soc. Rev.* **2020**, *49*, 765.
[26] L. Zhang, Y. Li, W. Che, D. Zhu, G. Li, Z. Xie, N. Song, S. Liu, B. Z. Tang, X. Liu, Z. Su, M. R. Bryce, *Adv. Sci.* **2019**, *6*, 1802050.
[27] L. Li, L. Zhang, X. Tong, Y. Li, Z. Yang, D. Zhu, Z. Su, Z. Xie, *Dalton Trans.* **2020**, *49*, 15332.
[28] Z. Wang, L. Li, W. Wang, R. Wang, G. Li, H. Bian, D. Zhu, M. R. Bryce, *Dalton Trans.* **2023**, *52*, 1595.
[29] A. L. Harris, *Nat. Rev. Cancer* **2002**, *2*, 38.
[30] D. Chen, Q. Xu, W. Wang, J. Shao, W. Huang, X. Dong, *Small* **2021**, *17*, 2006742.
[31] Z. Lv, H. Wei, Q. Li, X. Su, S. Liu, K. Y. Zhang, W. Lv, Q. Zhao, X. Li, W. Huang, *Chem. Sci.* **2018**, *9*, 502.
[32] V. Novohradsky, A. Rovira, C. Hally, A. Galindo, G. Vigueras, A. Gandioso, M. Svitelova, R. Bresolí-Obach, H. Kostrhunova, L. Markova, J. Kasparkova, S. Nonell, J. Ruiz, V. Brabec, V. Marchán, *Angew. Chem., Int. Ed.* **2019**, *58*, 6311.

[33] V. Novohradsky, L. Markova, H. Kostrhunova, J. Kasparkova, J. Ruiz, V. Marchán, V. Brabec, *Chem. Eur. J.* **2021**, *27*, 8547.
[34] A. Rovira, E. Ortega-Forte, C. Hally, M. Jordà-Redondo, D. Abad-Montero, G. Vigueras, J. I. Martínez, M. Bosch, S. Nonell, J. Ruiz, V. Marchán, *J. Med. Chem.* **2023**, *66*, 7849.
[35] E. Ortega-Forte, A. Rovira, M. López-Corrales, A. Hernández-García, F. J. Ballester, E. Izquierdo-García, M. Jordà-Redondo, M. Bosch, S. Nonell, M. D. Santana, J. Ruiz, V. Marchán, G. Gasser, *Chem. Sci.* **2023**, *14*, 7170.
[36] F. Qi, H. Yuan, Y. Chen, X.-X. Peng, Y. Wu, W. He, Z. Guo, *CCS Chem.* **2023**, *5*, 1583.
[37] Q. Ren, H. Wang, D. Li, A. Dao, J. Luo, D. Wang, P. Zhang, H. Huang, *Adv. Healthcare Mater.* **2024**, *13*, 2304067.
[38] B. Elias, A. Kirsch-De Mesmaeker, *Coord. Chem. Rev.* **2006**, *250*, 1627.
[39] S. Estalayo-Adrián, K. Garnir, C. Moucheron, *Chem. Commun.* **2018**, *54*, 322.
[40] C. S. Burke, A. Byrne, T. E. Keyes, *J. Am. Chem. Soc.* **2018**, *140*, 6945.
[41] a) S. A. Archer, A. Raza, F. Dröge, C. Robertson, A. J. Auty, D. Chekulaev, J. A. Weinstein, T. Keane, A. J. H. M. Meijer, J. W. Haycock, S. MacNeil, J. A. Thomas, *Chem. Sci.* **2019**, *10*, 3502; b) A. Raza, S. A. Archer, S. D. Fairbanks, K. L. Smitten, S. W. Botchway, J. A. Thomas, S. MacNeil, J. W. Haycock, *J. Am. Chem. Soc.* **2020**, *142*, 4639.
[42] L. Holden, R. C. Curley, G. Avella, C. Long, T. E. Keyes, *Angew. Chem., Int. Ed.* **2024**, e202408581.
[43] R. Bevernaegie, B. Doix, E. Bastien, A. Diman, A. Decottignies, O. Feron, B. Elias, *J. Am. Chem. Soc.* **2019**, *141*, 18486.
[44] a) C. K. Prier, D. A. Rankic, D. W. C. MacMillan, *Chem. Rev.* **2013**, *113*, 5322; b) J. Twilton, C. Le, P. Zhang, M. H. Shaw, R. W. Evans, D. W. C. MacMillan, *Nat. Rev. Chem.* **2017**, *1*, 0052; c) A. Y. Chan, I. B. Perry, N. B. Bissonnette, B. F. Buksh, G. A. Edwards, L. I. Frye, O. L. Garry, M. N. Lavagnino, B. X. Li, Y. Liang, E. Mao, A. Millet, J. V. Oakley, N. L. Reed, H. A. Sakai, C. P. Seath, D. W. C. MacMillan, *Chem. Rev.* **2022**, *122*, 1485.
[45] a) J. B. Geri, J. V. Oakley, T. Reyes-Robles, T. Wang, S. J. McCarver, C. H. White, F. P. Rodriguez-Rivera, D. L. Parker Jr., E. C. Hett, O. O. Fadeyi, R. C. Oslund, D. W. C. MacMillan, *Science* **2020**, *367*, 1091; b) Z. Huang, Z. Liu, X. Xie, R. Zeng, Z. Chen, L. Kong, X. Fan, P. R. Chen, *J. Am. Chem. Soc.* **2021**, *143*, 18714; c) T. Reyes-Robles, A. K. Olow, T. J. Bechtel, S. A. Lesley, O. O. Fadeyi, R. C. Oslund, *ACS Chem. Biol.* **2022**, *17*, 2304; d) Z. Liu, X. Xie, Z. Huang, F. Lin, S. Liu, Z. Chen, S. Qin, X. Fan, P. R. Chen, *Chem* **2022**, *8*, 2179; e) C. F. Meyer, C. P. Seath, S. D. Knutson, W. Lu, J. D. Rabinowitz, D. W. C. MacMillan, *J. Am. Chem. Soc.* **2022**, *144*, 23633; f) N. E. S. Tay, K. A. Ryu, J. L. Weber, A. K. Olow, D. C. Cabanero, D. R. Reichman, R. C. Oslund, O. O. Fadeyi, T. Rovis, *Nat. Chem.* **2023**, *15*, 101; g) C. P. Seath, A. J. Burton, X. Sun, G. Lee, R. E. Kleiner, D. W. C. MacMillan, T. W. Muir, *Nature* **2023**, *616*, 574.
[46] Y. Zhang, S. Liu, F. Guo, S. Qin, N. Zhou, Z. Liu, X. Fan, P. R. Chen, *J. Am. Chem. Soc.* **2024**, *146*, 15186.
[47] S. W. Huth, J. V. Oakley, C. P. Seath, J. B. Geri, A. D. Trowbridge, D. L. Parker Jr., F. P. Rodriguez-Rivera, A. G. Schwaid, C. Ramil, K. A. Ryu, C. H. White, O. O. Fadeyi, R. C. Oslund, D. W. C. MacMillan, *J. Am. Chem. Soc.* **2023**, *145*, 16289.
[48] H. Huang, S. Banerjee, K. Qiu, P. Zhang, Q. Blacque, T. Malcomson, M. J. Paterson, G. J. Clarkson, M. Staniforth, V. G. Stavros, G. Gasser, H. Chao, P. J. Sadler, *Nat. Chem.* **2019**, *11*, 1041.
[49] A. Chiarugi, C. Dölle, R. Felici, M. Ziegler, *Nat. Rev. Cancer* **2012**, *12*, 741.
[50] Z. Fan, Y. Rong, T. Sadhukhan, S. Liang, W. Li, Z. Yuan, Z. Zhu, S. Guo, S. Ji, J. Wang, R. Kushwaha, S. Banerjee, K. Raghavachari, H. Huang, *Angew. Chem., Int. Ed.* **2022**, *61*, e202202098.
[51] Z. Fan, J. Xie, R. Kushwaha, S. Liang, W. Li, A. A. Mandal, L. Wei, S. Banerjee, H. Huang, *Chem. Asian J.* **2023**, *18*, e202300047.
[52] C. Huang, C. Liang, T. Sadhukhan, S. Banerjee, Z. Fan, T. Li, Z. Zhu, P. Zhang, K. Raghavachari, H. Huang, *Angew. Chem., Int. Ed.* **2021**, *60*, 9474.
[53] Z. Zhu, L. Wei, Y. Lai, O. W. L. Carter, S. Banerjee, P. J. Sadler, H. Huang, *Dalton Trans.* **2022**, *51*, 10875.
[54] Z. Fan, J. Xie, T. Sadhukhan, C. Liang, C. Huang, W. Li, T. Li, P. Zhang, S. Banerjee, K. Raghavachari, H. Huang, *Chem. Eur. J.* **2022**, *28*, e202103346.
[55] Y. Wan, L.-H. Fu, C. Li, J. Lin, P. Huang, *Adv. Mater.* **2021**, *33*, 2103978.
[56] B. Lu, L. Wang, H. Tang, D. Cao, *J. Mater. Chem. B* **2023**, *11*, 4600.
[57] M. Li, Y. Xu, Z. Pu, T. Xiong, H. Huang, S. Long, S. Son, L. Yu, N. Singh, Y. Tong, J. L. Sessler, X. Peng, J. S. Kim, *Proc. Natl. Acad. Sci. USA* **2022**, *119*, e2210504119.
[58] D. Kim, V. Q. Dang, T. S. Teets, *Chem. Sci.* **2024**, *15*, 77.
[59] J. Karges, F. Heinemann, M. Jakubaszek, F. Maschietto, C. Subecz, M. Dotou, R. Vinck, O. Blacque, M. Tharaud, B. Goud, E. Viñuelas Zahínos, B. Spingler, I. Ciofini, G. Gasser, *J. Am. Chem. Soc.* **2020**, *142*, 6578.
[60] J. Karges, M. Tharaud, G. Gasser, *J. Med. Chem.* **2021**, *64*, 4612.
[61] A. Mani, T. Feng, A. Gandioso, R. Vinck, A. Notaro, L. Gourdon, P. Burckel, B. Saubaméa, O. Blacque, K. Cariou, J.-E. Belgaied, H. Chao, G. Gasser, *Angew. Chem., Int. Ed.* **2023**, *62*, e202218347.
[62] J. Zhao, Y. Gao, R. Huang, C. Chi, Y. Sun, G. Xu, X.-H. Xia, S. Gou, *J. Am. Chem. Soc.* **2023**, *145*, 11633.
[63] P. Shi, W. Gong, J. Zhao, Y. Jiao, Y. Sun, L. Fang, S. Gou, *Chem. Commun.* **2024**, *60*, 7503.
[64] J. A. Roque III, P. C. Barrett, H. D. Cole, L. M. Lifshits, G. Shi, S. Monro, D. von Dohlen, S. Kim, N. Russo, G. Deep, C. G. Cameron, M. E. Alberto, S. A. McFarland, *Chem. Sci.* **2020**, *11*, 9784.
[65] a) D. Shah, M. Eroy, J. Fakhry, A. Moffat, K. Fritz, H. D. Cole, C. G. Cameron, S. A. McFarland, G. Obaid, *Pharmaceutics* **2022**, *14*, 2426; b) H. D. Cole, M. Eroy, J. A. Roque III, G. Shi, M. Guirguis, J. Fakhry, C. G. Cameron, G. Obaid, S. A. McFarland, *Photochem. Photobiol.* **2023**, *99*, 751.
[66] L. M. Lifshits, J. A. Roque III, P. Konda, S. Monro, H. D. Cole, D. von Dohlen, S. Kim, G. Deep, R. P. Thummel, C. G. Cameron, S. Gujar, S. A. McFarland, *Chem. Sci.* **2020**, *11*, 11740.
[67] P. Konda, J. A. Roque III, L. M. Lifshits, A. Alcos, E. Azzam, G. Shi, C. G. Cameron, S. A. McFarland, S. Gujar, *Am. J. Cancer Res.* **2022**, *12*, 210.
[68] G. Hong, A. L. Antaris, H. Dai, *Nat. Biomed. Eng.* **2017**, *1*, 0010.
[69] L. Qiao, J. Liu, Y. Han, F. Wei, X. Liao, C. Zhang, L. Xie, L. Ji, H. Chao, *Chem. Commun.* **2021**, *57*, 1790.
[70] C. Liu, Y. Jiang, J. Xiang, C. Xiang, H. Li, H. Li, F. Wei, J. Huang, R. Li, K. M.-C. Wong, P. Gong, *Dyes Pigm.* **2023**, *209*, 110900.
[71] J. Liu, X. Yang, S. Wu, P. Gong, F. Pan, P. Zhang, C.-S. Lee, C. Liu, K. M.-C. Wong, *J. Mater. Chem. B* **2024**, *12*, 3710.
[72] Q. Yang, H. Jin, Y. Gao, J. Lin, H. Yang, S. Yang, *ACS Appl. Mater. Interfaces* **2019**, *11*, 15417.
[73] A. Gandioso, E. Izquierdo-García, P. Mesdom, P. Arnoux, N. Demeubayeva, P. Burckel, B. Saubaméa, M. Bosch, C. Frochot, V. Marchán, G. Gasser, *Chem. Eur. J.* **2023**, *29*, e202301742.
[74] G. He, N. Xu, H. Ge, Y. Lu, R. Wang, H. Wang, J. Du, J. Fan, W. Sun, X. Peng, *ACS Appl. Mater. Interfaces* **2021**, *13*, 19572.
[75] C. Liu, K. Wang, X. Gong, A. J. Heeger, *Chem. Soc. Rev.* **2016**, *45*, 4825.

[76] Z. Zhang, Z. Wei, J. Guo, J. Lyu, B. Wang, G. Wang, C. Wang, L. Zhou, Z. Yuan, G. Xing, C. Wu, X. Zhang, *Nat. Commun.* **2024**, *15*, 170.
[77] N. M. Idris, M. K. G. Jayakumar, A. Bansal, Y. Zhang, *Chem. Soc. Rev.* **2015**, *44*, 1449.
[78] J. Zhao, S. Sun, X. Li, W. Zhang, S. Gou, *ACS Appl. Bio Mater.* **2020**, *3*, 252.
[79] S. Liu, Y. Pei, Y. Sun, Z. Wang, H. Chen, D. Zhu, M. R. Bryce, B. Z. Tang, Y. Chang, *Aggregate* **2024**, *5*, e547.
[80] M. Pawlicki, H. A. Collins, R. G. Denning, H. L. Anderson, *Angew. Chem., Int. Ed.* **2009**, *48*, 3244.
[81] a) H. M. Kim, B. R. Cho, *Chem. Rev.* **2015**, *115*, 5014; b) A. Soleimany, D. K. Aghmiouni, M. Amirikhah, M. A. Shokrgozar, S. Khoee, B. Sarmento, *Adv. Funct. Mater.* **2024**, 2408594.
[82] A. Karotki, M. Khurana, J. R. Lepock, B. C. Wilson, *Photochem. Photobiol.* **2006**, *82*, 443.
[83] Y. Chen, R. Guan, C. Zhang, J. Huang, L. Ji, H. Chao, *Coord. Chem. Rev.* **2016**, *310*, 16.
[84] P. Zhang, C. K. C. Chiu, H. Huang, Y. P. Y. Lam, A. Habtemariam, T. Malcomson, M. J. Paterson, G. J. Clarkson, P. B. O'Connor, H. Chao, P. J. Sadler, *Angew. Chem., Int. Ed.* **2017**, *56*, 14898.
[85] E. M. Bolitho, C. Sanchez-Cano, H. Huang, I. Hands-Portman, M. Spink, P. D. Quinn, M. Harkiolaki, P. J. Sadler, *J. Biol. Inorg. Chem.* **2020**, *25*, 295.
[86] L. Luo, T. Zhu, X. Lu, B. Li, Q. Zhang, D. Li, J. Wu, Y. Tian, S. Ma, X. Tian, *Dyes Pigm.* **2024**, *221*, 111773.
[87] D. Chen, T. Shao, H. Zhao, F. Chen, Z. Fang, Y. Tian, X. Tian, *Dyes Pigm.* **2023**, *215*, 111271.
[88] J. Karges, S. Kuang, F. Maschietto, O. Blacque, I. Ciofini, H. Chao, G. Gasser, *Nat. Commun.* **2020**, *11*, 3262.
[89] J. Karges, J. Li, L. Zeng, H. Chao, G. Gasser, *ACS Appl. Mater. Interfaces* **2020**, *12*, 54433.
[90] J. Karges, S. Kuang, Y. C. Ong, H. Chao, G. Gasser, *Chem. Eur. J.* **2021**, *27*, 362.
[91] R. Vinck, J. Karges, M. Tharaud, K. Cariou, G. Gasser, *Dalton Trans.* **2021**, *50*, 14629.
[92] X.-D. Bi, R. Yang, Y.-C. Zhou, D. Chen, G.-K. Li, Y.-X. Guo, M.-F. Wang, D. Liu, F. Gao, *Inorg. Chem.* **2020**, *59*, 14920.
[93] X.-L. Li, L.-Z. Zeng, R. Yang, X.-D. Bi, Y. Zhang, R.-B. Cui, X.-X. Wu, F. Gao, *Inorg. Chem.* **2023**, *62*, 16122.
[94] Z. Zhou, J. Li, T. W. Rees, H. Wang, X. Li, H. Chao, P. J. Stang, *Proc. Natl. Acad. Sci. USA* **2018**, *115*, 5664.
[95] Z. Zhu, J. Liu, J. Huang, T. W. Rees, Y. Wang, H. Wang, X. Li, H. Chao, P. J. Stang, *Proc. Natl. Acad. Sci. USA* **2019**, *116*, 20296.
[96] a) C. Li, Y. Wang, Y. Lu, J. Guo, C. Zhu, H. He, X. Duan, M. Pan, C. Su, *Chin. Chem. Lett.* **2020**, *31*, 1183; b) Y.-Y. Liu, H.-J. Yu, Y.-P. Wang, C.-J. Li, X.-F. Wang, C.-G. Ye, H.-L. Yao, M. Pan, C.-Y. Su, *Mater. Chem. Front.* **2022**, *6*, 948.
[97] Y. Shen, A. J. Shuhendler, D. Ye, J.-J. Xu, H.-Y. Chen, *Chem. Soc. Rev.* **2016**, *45*, 6725.
[98] a) A. Bansal, F. Yang, T. Xi, Y. Zhang, J. S. Ho, *Proc. Natl. Acad. Sci. USA* **2018**, *115*, 1469; b) K. Yamagishi, I. Kirino, I. Takahashi, H. Amano, S. Takeoka, Y. Morimoto, T. Fujie, *Nat. Biomed. Eng.* **2019**, *3*, 27; c) W. S. Kim, M. I. Khot, H.-M. Woo, S. Hong, D.-H. Baek, T. Maisey, B. Daniels, P. L. Coletta, B.-J. Yoon, D. G. Jayne, S. I. Park, *Nat. Commun.* **2022**, *13*, 2178.
[99] M. Yang, J. Huang, J. Fan, J. Du, K. Pu, X. Peng, *Chem. Soc. Rev.* **2020**, *49*, 6800.
[100] H. N. Kagalwala, R. T. Reeves, A. R. Lippert, *Curr. Opin. Chem. Biol.* **2022**, *68*, 102134.
[101] R. Wang, X. Li, J. Yoon, *ACS Appl. Mater. Interfaces* **2021**, *13*, 19543.
[102] A. I. Lamond, W. C. Earnshaw, *Science* **1998**, *280*, 547.
[103] L. H. Hurley, *Nat. Rev. Cancer* **2002**, *2*, 188.
[104] X. Tian, Y. Zhu, M. Zhang, L. Luo, J. Wu, H. Zhou, L. Guan, G. Battaglia, Y. Tian, *Chem. Commun.* **2017**, *53*, 3303.
[105] P. Zhang, H. Huang, S. Banerjee, G. J. Clarkson, C. Ge, C. Imberti, P. J. Sadler, *Angew. Chem., Int. Ed.* **2019**, *58*, 2350.
[106] X.-J. Chao, C.-H. Huang, M. Tang, Z.-Y. Yan, R. Huang, Y. Li, B.-Z. Zhu, *Nucleic Acids Res.* **2023**, *51*, 3041.
[107] A. W. McKinley, P. Lincoln, E. M. Tuite, *Coord. Chem. Rev.* **2011**, *255*, 2676.
[108] C. A. Puckett, J. K. Barton, *J. Am. Chem. Soc.* **2007**, *129*, 46.
[109] J. Nunnari, A. Suomalainen, *Cell* **2012**, *148*, 1145.
[110] D. R. Green, J. C. Reed, *Science* **1998**, *281*, 1309.
[111] S. Fulda, L. Galluzzi, G. Kroemer, *Nat. Rev. Drug Discov.* **2010**, *9*, 447.
[112] J. Zielonka, J. Joseph, A. Sikora, M. Hardy, O. Ouari, J. Vasquez-Vivar, G. Cheng, M. Lopez, B. Kalyanaraman, *Chem. Rev.* **2017**, *117*, 10043.
[113] J. Liu, Y. Chen, G. Li, P. Zhang, C. Jin, L. Zeng, L. Ji, H. Chao, *Biomaterials* **2015**, *56*, 140.
[114] W. Lv, Z. Zhang, K. Y. Zhang, H. Yang, S. Liu, A. Xu, S. Guo, Q. Zhao, W. Huang, *Angew. Chem., Int. Ed.* **2016**, *55*, 9947.
[115] H. Yuan, Z. Han, Y. Chen, F. Qi, H. Fang, Z. Guo, S. Zhang, W. He, *Angew. Chem., Int. Ed.* **2021**, *60*, 8174.
[116] S. Chakrabortty, B. K. Agrawalla, A. Stumper, N. M. Vegi, S. Fischer, C. Reichardt, M. Kögler, B. Dietzek, M. Feuring-Buske, C. Buske, S. Rau, T. Weil, *J. Am. Chem. Soc.* **2017**, *139*, 2512.
[117] N. Naskar, W. Liu, H. Qi, A. Stumper, S. Fischer, T. Diemant, R. J. Behm, U. Kaiser, S. Rau, T. Weil, S. Chakrabortty, *ACS Appl. Mater. Interfaces* **2022**, *14*, 48327.
[118] Y. Li, C.-P. Tan, W. Zhang, L. He, L.-N. Ji, Z.-W. Mao, *Biomaterials* **2015**, *39*, 95.
[119] S. P.-Y. Li, C. T.-S. Lau, M.-W. Louie, Y.-W. Lam, S. H. Cheng, K. K.-W. Lo, *Biomaterials* **2013**, *34*, 7519.
[120] S. Yi, Z. Lu, J. Zhang, J. Wang, Z. Xie, L. Hou, *ACS Appl. Mater. Interfaces* **2019**, *11*, 15276.
[121] X. Cai, K.-N. Wang, W. Ma, Y. Yang, G. Chen, H. Fu, C. Cui, Z. Yu, X. Wang, *J. Nanobiotechnol.* **2021**, *19*, 254.
[122] Y. Jiang, W. Zhu, Z. Xu, Z. Zhang, S. Tang, M. Fan, Z. Li, J. Zhang, C. Yang, W.-C. Law, K.-T. Yong, D. Wang, G. Xu, B. Z. Tang, *Chem. Eng. J.* **2022**, *448*, 137604.
[123] X. Yang, L. Cheng, Y. Zhao, H. Ma, H. Song, X. Yang, K.-N. Wang, Y. Zhang, *J. Colloid Interface Sci.* **2024**, *659*, 320.
[124] C. Lee, J. S. Nam, C. G. Lee, M. Park, C.-M. Yoo, H.-W. Rhee, J. K. Seo, T.-H. Kwon, *Nat. Commun.* **2021**, *12*, 26.
[125] X. Li, J. Wu, L. Wang, C. He, L. Chen, Y. Jiao, C. Duan, *Angew. Chem., Int. Ed.* **2020**, *59*, 6420.
[126] X. Li, Z. Wang, X. Hao, J. Zhang, X. Zhao, Y. Yao, W. Wei, R. Cai, C. He, C. Duan, Z. Guo, J. Zhao, X. Wang, *J. Am. Chem. Soc.* **2023**, *145*, 14766.
[127] Y.-Y. Ling, Z.-Y. Li, X. Mu, Y.-J. Kong, L. Hao, W.-J. Wang, Q.-H. Shen, Y.-B. Zhang, C.-P. Tan, *Eur. J. Med. Chem.* **2024**, *275*, 116638.
[128] F. J. Bock, S. W. G. Tait, *Nat. Rev. Mol. Cell Biol.* **2020**, *21*, 85.
[129] L. Wang, J. Karges, F. Wei, L. Xie, Z. Chen, G. Gasser, L. Ji, H. Chao, *Chem. Sci.* **2023**, *14*, 1461.
[130] T. Feng, Z. Tang, J. Karges, J. Shu, K. Xiong, C. Jin, Y. Chen, G. Gasser, L. Ji, H. Chao, *Chem. Sci.* **2024**, *15*, 6752.
[131] C. de Duve, R. Wattiaux, *Annu. Rev. Physiol.* **1966**, *28*, 435.
[132] P. Boya, G. Kroemer, *Oncogene* **2008**, *27*, 6434.
[133] S. Piao, R. K. Amaravadi, *Ann. N. Y. Acad. Sci.* **2016**, *1371*, 45.
[134] H. Huang, B. Yu, P. Zhang, J. Huang, Y. Chen, G. Gasser, L. Ji, H. Chao, *Angew. Chem., Int. Ed.* **2015**, *54*, 14049.
[135] E. Du, X. Hu, S. Roy, P. Wang, K. Deasy, T. Mochizuki, Y. Zhang, *Chem. Commun.* **2017**, *53*, 6033.
[136] Q. Wu, C. Yuan, J. Wang, G. Li, C. Zhu, L. Li, Z. Wang, Q. Lv, W. Mei, *JACS Au* **2024**, *4*, 1081.
[137] P. Zhang, Y. Wang, K. Qiu, Z. Zhao, R. Hu, C. He, Q. Zhang, H. Chao, *Chem. Commun.* **2017**, *53*, 12341.

[138] D. S. Schwarz, M. D. Blower, *Cell. Mol. Life Sci.* **2016**, *73*, 79.
[139] M. Schröder, R. J. Kaufman, *Mutat. Res.* **2005**, *569*, 29.
[140] D. V. Krysko, A. D. Garg, A. Kaczmarek, O. Krysko, P. Agostinis, P. Vandenabeele, *Nat. Rev. Cancer* **2012**, *12*, 860.
[141] J. S. Nam, M.-G. Kang, J. Kang, S.-Y. Park, S. J. C. Lee, H.-T. Kim, J. K. Seo, O.-H. Kwon, M. H. Lim, H.-W. Rhee, T.-H. Kwon, *J. Am. Chem. Soc.* **2016**, *138*, 10968.
[142] C. G. Lee, C. Lee, J. Lee, J. S. Nam, B.-S. Kim, T.-H. Kwon, *Angew. Chem., Int. Ed.* **2022**, *61*, e202210623.
[143] B. Yuan, J. Liu, R. Guan, C. Jin, L. Ji, H. Chao, *Dalton Trans.* **2019**, *48*, 6408.
[144] K. Qiu, J. Wang, C. Song, L. Wang, H. Zhu, H. Huang, J. Huang, H. Wang, L. Ji, H. Chao, *ACS Appl. Mater. Interfaces* **2017**, *9*, 18482.
[145] K.-N. Wang, L.-Y. Liu, G. Qi, X.-J. Chao, W. Ma, Z. Yu, Q. Pan, Z.-W. Mao, B. Liu, *Adv. Sci.* **2021**, *8*, 2004379.
[146] K. Qiu, Y. Wen, C. Ouyang, X. Liao, C. Liu, T. W. Rees, Q. Zhang, L. Ji, H. Chao, *Chem. Commun.* **2019**, *55*, 11235.
[147] D. Kalderon, B. L. Roberts, W. D. Richardson, A. E. Smith, *Cell* **1984**, *39*, 499.
[148] D. Singh, D. Rajput, S. Kanvah, *Chem. Commun.* **2022**, *58*, 2413.
[149] S. Munro, H. R. B. Pelham, *Cell* **1987**, *48*, 899.
[150] K. Y. Zhang, L. Song, T. Gu, H. Wang, C. Yang, H. Zhou, P. Gao, S. Liu, Q. Zhao, *Eur. J. Inorg. Chem.* **2020**, *2020*, 3996.
[151] F. Zhao, W. Wang, W. Wu, *Dalton Trans.* **2021**, *50*, 3536.
[152] a) Z.-Y. Pan, W.-W. Feng, Q.-Y. Liu, L. He, D.-H. Yao, Z.-D. He, *Dyes Pigm.* **2022**, *203*, 110387; b) J.-H. Zhu, S.-M. Yiu, B. Z. Tang, K. K.-W. Lo, *Inorg. Chem.* **2021**, *60*, 11672.
[153] W. Xu, M. M. S. Lee, J.-J. Nie, Z. Zhang, R. T. K. Kwok, J. W. Y. Lam, F.-J. Xu, D. Wang, B. Z. Tang, *Angew. Chem., Int. Ed.* **2020**, *59*, 9610.
[154] J. Fang, H. Nakamura, H. Maeda, *Adv. Drug Deliv. Rev.* **2011**, *63*, 136.
[155] Y. Barenholz, *J. Control. Release* **2012**, *160*, 117.
[156] E. Miele, G. P. Spinelli, E. Miele, F. Tomao, S. Tomao, *Int. J. Nanomedicine* **2009**, *4*, 99.
[157] Y. Deng, F. Huang, J. Zhang, J. Liu, B. Li, R. Ouyang, Y. Miao, Y. Sun, Y. Li, *Dyes Pigm.* **2020**, *182*, 108651.
[158] F. Wang, M. Lan, W.-P. To, K. Li, C.-N. Lok, P. Wang, C.-M. Che, *Chem. Commun.* **2016**, *52*, 13273.
[159] N. Soliman, L. K. McKenzie, J. Karges, E. Bertrand, M. Tharaud, M. Jakubaszek, V. Guérineau, B. Goud, M. Hollenstein, G. Gasser, C. M. Thomas, *Chem. Sci.* **2020**, *11*, 2657.
[160] J. P. M. António, A. Gandioso, F. Nemati, N. Soliman, R. Vinck, F. Sun, C. Robert, P. Burckel, D. Decaudin, C. M. Thomas, G. Gasser, *Chem. Sci.* **2023**, *14*, 362.
[161] X.-Q. Zhou, M. Xiao, V. Ramu, J. Hilgendorf, X. Li, P. Papadopoulou, M. A. Siegler, A. Kros, W. Sun, S. Bonnet, *J. Am. Chem. Soc.* **2020**, *142*, 10383.
[162] X.-Q. Zhou, P. Wang, V. Ramu, L. Zhang, S. Jiang, X. Li, S. Abyar, P. Papadopoulou, Y. Shao, L. Bretin, M. A. Siegler, F. Buda, A. Kros, J. Fan, X. Peng, W. Sun, S. Bonnet, *Nat. Chem.* **2023**, *15*, 980.
[163] J. D. Byrne, T. Betancourt, L. Brannon-Peppas, *Adv. Drug Deliv. Rev.* **2008**, *60*, 1615.
[164] C. Dumontet, J. M. Reichert, P. D. Senter, J. M. Lambert, A. Beck, *Nat. Rev. Drug Discov.* **2023**, *22*, 641.
[165] K. Zierler, *Am. J. Physiol.* **1999**, *276*, E409.
[166] M. Mueckler, *Eur. J. Biochem.* **1994**, *219*, 713.
[167] M. L. Macheda, S. Rogers, J. D. Best, *J. Cell. Physiol.* **2005**, *202*, 654.
[168] J. Liu, X. Liao, K. Xiong, S. Kuang, C. Jin, L. Ji, H. Chao, *Chem. Commun.* **2020**, *56*, 5839.
[169] V. Douard, R. P. Ferraris, *Am. J. Physiol. Endocrinol. Metab.* **2008**, *295*, E227.
[170] S. P. Zamora-León, D. W. Golde, I. I. Concha, C. I. Rivas, F. Delgado-López, J. Baselga, F. Nualart, J. C. Vera, *Proc. Natl. Acad. Sci. USA* **1996**, *93*, 1847.
[171] K. Y. Zhang, K. K.-S. Tso, M.-W. Louie, H.-W. Liu, K. K.-W. Lo, *Organometallics* **2013**, *32*, 5098.
[172] K. K.-W. Lo, W. H.-T. Law, J. C.-Y. Chan, H.-W. Liu, K. Y. Zhang, *Metallomics* **2013**, *5*, 808.
[173] R. J. McMahon, *Annu. Rev. Nutr.* **2002**, *22*, 221.
[174] W. X. Ren, J. Han, S. Uhm, Y. J. Jang, C. Kang, J.-H. Kim, J. S. Kim, *Chem. Commun.* **2015**, *51*, 10403.
[175] J. Li, L. Zeng, K. Xiong, T. W. Rees, C. Jin, W. Wu, Y. Chen, L. Ji, H. Chao, *Chem. Commun.* **2019**, *55*, 10972.
[176] D. Chen, H. Zhao, T. Shao, X. Lu, Z. Fang, H. Cao, Y. Tian, X. Tian, *J. Mater. Chem. B* **2022**, *10*, 5765.
[177] L. Wei, X. He, X. Shang, M. Kandawa-Shultz, G. Shao, Y. Wang, *Dyes Pigm.* **2023**, *219*, 111641.
[178] L. Wei, X. He, D. Zhao, M. Kandawa-Shultz, G. Shao, Y. Wang, *Eur. J. Med. Chem.* **2024**, *264*, 115985.
[179] L. Wei, X. He, C. Liu, M. Kandawa-Shultz, G. Shao, Y. Wang, *ACS Appl. Nano Mater.* **2024**, *7*, 1170.
[180] E. L. R. Stokstad, J. Koch, *Physiol. Rev.* **1967**, *47*, 83.
[181] A. C. Antony, *Annu. Rev. Nutr.* **1996**, *16*, 501.
[182] S. D. Weitman, R. H. Lark, L. R. Coney, D. W. Fort, V. Frasca, V. R. Zurawski Jr., B. A. Kamen, *Cancer Res.* **1992**, *52*, 3396.
[183] J. Sudimack, R. J. Lee, *Adv. Drug Deliv. Rev.* **2000**, *41*, 147.
[184] X. He, L. Wei, J. Chen, S. Ge, M. Kandawa-Shultz, G. Shao, Y. Wang, *Inorg. Chem. Front.* **2023**, *10*, 4780.
[185] R. O. Hynes, *Cell* **1992**, *69*, 11.
[186] J. S. Desgrosellier, D. A. Cheresh, *Nat. Rev. Cancer* **2010**, *10*, 9.
[187] Z. Zhao, K. Qiu, J. Liu, X. Hao, J. Wang, *Chem. Commun.* **2020**, *56*, 12542.
[188] Y. Yarden, M. X. Sliwkowski, *Nat. Rev. Mol. Cell Biol.* **2001**, *2*, 127.
[189] N. E. Hynes, H. A. Lane, *Nat. Rev. Cancer* **2005**, *5*, 341.
[190] L. Huang, P. K.-K. Leung, L. C.-C. Lee, G.-X. Xu, Y.-W. Lam, K. K.-W. Lo, *Chem. Commun.* **2022**, *58*, 10162.
[191] H. Wang, Y. Lai, D. Li, J. Karges, P. Zhang, H. Huang, *J. Med. Chem.* **2024**, *67*, 1336.
[192] J. R. Vane, Y. S. Bakhle, R. M. Botting, *Annu. Rev. Pharmacol. Toxicol.* **1998**, *38*, 97.
[193] K. Subbaramaiah, A. J. Dannenberg, *Trends Pharmacol. Sci.* **2003**, *24*, 96.
[194] C. Liu, J. Xiang, C. Xiang, H. Li, *Bioorg. Chem.* **2021**, *114*, 105142.
[195] C. T. Supuran, *Biochem. J.* **2016**, *473*, 2023.
[196] J. Chiche, K. Ilc, J. Laferrière, E. Trottier, F. Dayan, N. M. Mazure, M. C. Brahimi-Horn, J. Pouysségur, *Cancer Res.* **2009**, *69*, 358.
[197] C. T. Supuran, *Nat. Rev. Drug Discov.* **2008**, *7*, 168.
[198] X. Su, W.-J. Wang, Q. Cao, H. Zhang, B. Liu, Y. Ling, X. Zhou, Z.-W. Mao, *Angew. Chem., Int. Ed.* **2022**, *61*, e202115800.
[199] Y.-Y. Ling, Y.-J. Kong, L. Hao, Z.-Y. Pan, Z.-W. Mao, C.-P. Tan, *Inorg. Chem. Front.* **2023**, *10*, 3284.
[200] Y. Wang, P. Mesdom, K. Purkait, B. Saubaméa, P. Burckel, P. Arnoux, C. Frochot, K. Cariou, T. Rossel, G. Gasser, *Chem. Sci.* **2023**, *14*, 11749.
[201] S. Kelm, R. Schauer, *Int. Rev. Cytol.* **1997**, *175*, 137.
[202] M. M. Fuster, J. D. Esko, *Nat. Rev. Cancer* **2005**, *5*, 526.
[203] M. Lin, S. Zou, X. Liao, Y. Chen, D. Luo, L. Ji, H. Chao, *Chem. Commun.* **2021**, *57*, 4408.
[204] S. Zhou, C. Gravekamp, D. Bermudes, K. Liu, *Nat. Rev. Cancer* **2018**, *18*, 727.
[205] W. Lin, Y. Liu, J. Wang, Z. Zhao, K. Lu, H. Meng, R. Luoliu, X. He, J. Shen, Z.-W. Mao, W. Xia, *Angew. Chem., Int. Ed.* **2023**, *62*, e202310158.
[206] I. Dagogo-Jack, A. T. Shaw, *Nat. Rev. Clin. Oncol.* **2018**, *15*, 81.
[207] C. Agatemor, M. J. Buettner, R. Ariss, K. Muthiah, C. T. Saeui, K. J. Yarema, *Nat. Rev. Chem.* **2019**, *3*, 605.

[208] H. Wang, Y. Bo, Y. Liu, M. Xu, K. Cai, R. Wang, J. Cheng, *Biomaterials* **2019**, *218*, 119305.
[209] H. Wang, R. Wang, K. Cai, H. He, Y. Liu, J. Yen, Z. Wang, M. Xu, Y. Sun, X. Zhou, Q. Yin, L. Tang, I. T. Dobrucki, L. W. Dobrucki, E. J. Chaney, S. A. Boppart, T. M. Fan, S. Lezmi, X. Chen, L. Yin, J. Cheng, *Nat. Chem. Biol.* **2017**, *13*, 415.
[210] J.-W. Yoo, D. J. Irvine, D. E. Discher, S. Mitragotri, *Nat. Rev. Drug Discov.* **2011**, *10*, 521.
[211] R. Kalluri, V. S. LeBleu, *Science* **2020**, *367*, eaau6977.
[212] R. H. Fang, A. V. Kroll, W. Gao, L. Zhang, *Adv. Mater.* **2018**, *30*, 1706759.
[213] Z. Li, Z. Zhou, Y. Wang, J. Wang, L. Zhou, H.-B. Cheng, J. Yoon, *Coord. Chem. Rev.* **2023**, *493*, 215324.
[214] R. A. Gatenby, R. J. Gillies, *Nat. Rev. Cancer* **2004**, *4*, 891.
[215] B. A. Webb, M. Chimenti, M. P. Jacobson, D. L. Barber, *Nat. Rev. Cancer* **2011**, *11*, 671.
[216] L. He, Y. Li, C.-P. Tan, R.-R. Ye, M.-H. Chen, J.-J. Cao, L.-N. Ji, Z.-W. Mao, *Chem. Sci.* **2015**, *6*, 5409.
[217] P. Yang, S. Zhang, K. Wang, H. Qi, *Dalton Trans.* **2021**, *50*, 17338.
[218] D.-Y. Zhang, Y. Zheng, H. Zhang, L. He, C.-P. Tan, J.-H. Sun, W. Zhang, X. Peng, Q. Zhan, L.-N. Ji, Z.-W. Mao, *Nanoscale* **2017**, *9*, 18966.
[219] F.-X. Wang, M.-H. Chen, Y.-N. Lin, H. Zhang, C.-P. Tan, L.-N. Ji, Z.-W. Mao, *ACS Appl. Mater. Interfaces* **2017**, *9*, 42471.
[220] M. Gillard, L. Troian-Gautier, A. Decottignies, B. Elias, *J. Med. Chem.* **2024**, *67*, 2549.
[221] M. Valko, D. Leibfritz, J. Moncol, M. T. D. Cronin, M. Mazur, J. Telser, *Int. J. Biochem. Cell Biol.* **2007**, *39*, 44.
[222] G.-Y. Liou, P. Storz, *Free Radic. Res.* **2010**, *44*, 479.
[223] Y.-Y. Ling, W.-J. Wang, L. Hao, X.-W. Wu, J.-H. Liang, H. Zhang, Z.-W. Mao, C.-P. Tan, *Small* **2022**, *18*, 2203659.
[224] J. M. Estrela, A. Ortega, E. Obrador, *Crit. Rev. Clin. Lab. Sci.* **2006**, *43*, 143.
[225] G.-X. Xu, L. C.-C. Lee, C. W.-C. Kwok, P. K.-K. Leung, J.-H. Zhu, K. K.-W. Lo, *Eur. J. Inorg. Chem.* **2021**, *2021*, 3432.
[226] W. Zhang, W. Chen, F. Fu, M.-J. Li, *Dalton Trans.* **2024**, *53*, 5957.
[227] R. Tu, J. Liu, W. Chen, F. Fu, M.-J. Li, *Dalton Trans.* **2023**, *52*, 13137.
[228] T. Huang, Q. Yu, S. Liu, K. Y. Zhang, W. Huang, Q. Zhao, *ChemBioChem* **2019**, *20*, 576.
[229] L. Zeng, S. Kuang, G. Li, C. Jin, L. Ji, H. Chao, *Chem. Commun.* **2017**, *53*, 1977.
[230] W. Ying, *Antioxid. Redox Signal.* **2008**, *10*, 179.
[231] W. Xiao, R.-S. Wang, D. E. Handy, J. Loscalzo, *Antioxid. Redox Signal.* **2018**, *28*, 251.
[232] S. Shamjith, M. M. Joseph, V. P. Murali, G. S. Remya, J. B. Nair, C. H. Suresh, K. K. Maiti, *Biosens. Bioelectron.* **2022**, *204*, 114087.
[233] R. Wang, *Physiol. Rev.* **2012**, *92*, 791.
[234] C. Szabo, *Nat. Rev. Drug Discov.* **2016**, *15*, 185.
[235] S. Shamjith, V. P. Murali, M. M. Joesph, T. S. Fathima, R. Chandana, R. O. Jayarajan, K. K. Maiti, *ACS Appl. Mater. Interfaces* **2024**, *16*, 27114.
[236] J. Zhang, X. Chai, X.-P. He, H.-J. Kim, J. Yoon, H. Tian, *Chem. Soc. Rev.* **2019**, *48*, 683.
[237] H.-W. Liu, L. Chen, C. Xu, Z. Li, H. Zhang, X.-B. Zhang, W. Tan, *Chem. Soc. Rev.* **2018**, *47*, 7140.
[238] E. I. Solomon, U. M. Sundaram, T. E. Machonkin, *Chem. Rev.* **1996**, *96*, 2563.
[239] V. Gray-Schopfer, C. Wellbrock, R. Marais, *Nature* **2007**, *445*, 851.
[240] Y. Liu, H. Zhao, L. Li, B. Yang, Y. Yue, M. Li, X. Shi, B. Zhang, L. Wang, C. Qi, Y. Liu, S. Ren, K. Zhang, J. Yoon, *Sens. Actuators, B* **2023**, *374*, 132836.
[241] R. B. P. Elmes, *Chem. Commun.* **2016**, *52*, 8935.
[242] C. P. Guise, A. M. Mowday, A. Ashoorzadeh, R. Yuan, W.-H. Lin, D.-H. Wu, J. B. Smaill, A. V. Patterson, K. Ding, *Chin. J. Cancer* **2014**, *33*, 80.
[243] S. Kuang, L. Sun, X. Zhang, X. Liao, T. W. Rees, L. Zeng, Y. Chen, X. Zhang, L. Ji, H. Chao, *Angew. Chem., Int. Ed.* **2020**, *59*, 20697.
[244] G. Thomas, *Nat. Rev. Mol. Cell Biol.* **2002**, *3*, 753.
[245] L. Huang, L. C.-C. Lee, J. Shum, G.-X. Xu, K. K.-W. Lo, *Chem. Commun.* **2024**, *60*, 6186.
[246] E. M. Sletten, C. R. Bertozzi, *Angew. Chem., Int. Ed.* **2009**, *48*, 6974.
[247] L. Taiariol, C. Chaix, C. Farre, E. Moreau, *Chem. Rev.* **2022**, *122*, 340.
[248] L. Li, Z. Zhang, *Molecules* **2016**, *21*, 1393.
[249] E. M. Sletten, C. R. Bertozzi, *Acc. Chem. Res.* **2011**, *44*, 666.
[250] D. A. Bilodeau, K. D. Margison, M. Serhan, J. P. Pezacki, *Chem. Rev.* **2021**, *121*, 6699.
[251] K. Porte, M. Riomet, C. Figliola, D. Audisio, F. Taran, *Chem. Rev.* **2021**, *121*, 6718.
[252] B. L. Oliveira, Z. Guo, G. J. L. Bernardes, *Chem. Soc. Rev.* **2017**, *46*, 4895.
[253] L. K. B. Tam, D. K. P. Ng, *Mater. Chem. Front.* **2023**, *7*, 3184.
[254] P. K.-K. Leung, K. K.-W. Lo, *Chem. Commun.* **2020**, *56*, 6074.
[255] P. K.-K. Leung, L. C.-C. Lee, H. H.-Y. Yeung, K.-W. Io, K. K.-W. Lo, *Chem. Commun.* **2021**, *57*, 4914.
[256] A. M.-H. Yip, C. K.-H. Lai, K. S.-M. Yiu, K. K.-W. Lo, *Angew. Chem., Int. Ed.* **2022**, *61*, e202116078.
[257] J. Shum, L. C.-C. Lee, M. W.-L. Chiang, Y.-W. Lam, K. K.-W. Lo, *Angew. Chem., Int. Ed.* **2023**, *62*, e202303931.
[258] G.-X. Xu, L. C.-C. Lee, P. K.-K. Leung, E. C.-L. Mak, J. Shum, K. Y. Zhang, Q. Zhao, K. K.-W. Lo, *Chem. Sci.* **2023**, *14*, 13508.
[259] Y.-L. Ma, S. Yan, X.-J. Xu, H. Cao, R. Wang, *Chin. Chem. Lett.* **2024**, *35*, 108645.
[260] M. Binnewies, E. W. Roberts, K. Kersten, V. Chan, D. F. Fearon, M. Merad, L. M. Coussens, D. I. Gabrilovich, S. Ostrand-Rosenberg, C. C. Hedrick, R. H. Vonderheide, M. J. Pittet, R. K. Jain, W. Zou, T. K. Howcroft, E. C. Woodhouse, R. A. Weinberg, M. F. Krummel, *Nat. Med.* **2018**, *24*, 541.
[261] T. P. Szatrowski, C. F. Nathan, *Cancer Res.* **1991**, *51*, 794.
[262] C. Liang, X. Zhang, M. Yang, W. Wang, P. Chen, X. Dong, *ACS Materials Lett.* **2020**, *2*, 1268.
[263] A. L. Linsebigler, G. Lu, J. T. Yates Jr., *Chem. Rev.* **1995**, *95*, 735.
[264] J.-Y. Zhou, W.-J. Wang, C.-Y. Zhang, Y.-Y. Ling, X.-J. Hong, Q. Su, W.-G. Li, Z.-W. Mao, B. Cheng, C.-P. Tan, T. Wu, *Biomaterials* **2022**, *289*, 121757.
[265] W.-J. Ong, L.-L. Tan, Y. H. Ng, S.-T. Yong, S.-P. Chai, *Chem. Rev.* **2016**, *116*, 7159.
[266] R.-Q. Li, C. Zhang, B.-R. Xie, W.-Y. Yu, W.-X. Qiu, H. Cheng, X.-Z. Zhang, *Biomaterials* **2019**, *194*, 84.
[267] F. Wei, S. Kuang, T. W. Rees, X. Liao, J. Liu, D. Luo, J. Wang, X. Zhang, L. Ji, H. Chao, *Biomaterials* **2021**, *276*, 121064.
[268] F. Wei, J. Karges, S. Gao, L. Wang, X. Zhang, X.-C. Shen, L. Ji, H. Chao, *Nano Today* **2024**, *54*, 102066.
[269] F. Wei, J. Karges, J. Shen, L. Xie, K. Xiong, X. Zhang, L. Ji, H. Chao, *Nano Today* **2022**, *44*, 101509.
[270] F. Wei, J. Liang, Z. Tan, S. Tang, H. Xu, H. Liang, X.-C. Shen, H. Chao, *Chem. Eng. J.* **2024**, *485*, 150154.
[271] Y. Xiong, C. Xiao, Z. Li, X. Yang, *Chem. Soc. Rev.* **2021**, *50*, 6013.
[272] L. Ke, F. Wei, X. Liao, T. W. Rees, S. Kuang, Z. Liu, Y. Chen, L. Ji, H. Chao, *Nanoscale* **2021**, *13*, 7590.
[273] L. Ke, F. Wei, L. Xie, J. Karges, Y. Chen, L. Ji, H. Chao, *Angew. Chem., Int. Ed.* **2022**, *61*, e202205429.
[274] T. Feng, Z. Tang, J. Karges, J. Shen, C. Jin, Y. Chen, Y. Pan, Y. He, L. Ji, H. Chao, *Biomaterials* **2023**, *301*, 122212.
[275] X. Liao, J. Shen, W. Wu, S. Kuang, M. Lin, J. Karges, Z. Tang, H. Chao, *Inorg. Chem. Front.* **2021**, *8*, 5045.

[276] S. Gao, F. Wei, J. Karges, Y. Zhao, L. Ji, H. Chao, *Inorg. Chem. Front.* **2023**, *10*, 2716.
[277] J. Winkler, A. Abisoye-Ogunniyan, K. J. Metcalf, Z. Werb, *Nat. Commun.* **2020**, *11*, 5120.
[278] D. O'Sullivan, D. E. Sanin, E. J. Pearce, E. L. Pearce, *Nat. Rev. Immunol.* **2019**, *19*, 324.
[279] M. Platten, E. A. A. Nollen, U. F. Röhrig, F. Fallarino, C. A. Opitz, *Nat. Rev. Drug Discov.* **2019**, *18*, 379.
[280] R. B. Mokhtari, T. S. Homayouni, N. Baluch, E. Morgatskaya, S. Kumar, B. Das, H. Yeger, *Oncotarget* **2017**, *8*, 38022.
[281] G.-G. Yang, L. Hao, Q. Cao, H. Zhang, J. Yang, L.-N. Ji, Z.-W. Mao, *ACS Appl. Mater. Interfaces* **2018**, *10*, 28301.
[282] H. Xiang, H. Chen, H. P. Tham, S. Z. F. Phua, J.-G. Liu, Y. Zhao, *ACS Appl. Mater. Interfaces* **2017**, *9*, 27553.
[283] J. Guo, Y. Lin, S. He, Y. Chen, F. Li, R. Ruan, G. Pan, H. Nan, J. Song, J. Zhang, *Chin. Chem. Lett.* **2024**, *35*, 109537.
[284] J. Liu, A. W. Prentice, G. J. Clarkson, J. M. Woolley, V. G. Stavros, M. J. Paterson, P. J. Sadler, *Adv. Mater.* **2023**, *35*, 2210363.
[285] J. Karges, T. Yempala, M. Tharaud, D. Gibson, G. Gasser, *Angew. Chem., Int. Ed.* **2020**, *59*, 7069.
[286] B. Vogelstein, N. Papadopoulos, V. E. Velculescu, S. Zhou, L. A. Diaz Jr., K. W. Kinzler, *Science* **2013**, *339*, 1546.
[287] L. Zhong, Y. Li, L. Xiong, W. Wang, M. Wu, T. Yuan, W. Yang, C. Tian, Z. Miao, T. Wang, S. Yang, *Signal Transduct. Target. Ther.* **2021**, *6*, 201.
[288] J. Zhao, X. Zhang, L. Fang, C. Gao, C. Xu, S. Gou, *Small* **2020**, *16*, 2000363.
[289] W. Abuduwaili, X. Wang, A.-T. Huang, J.-L. Sun, R.-C. Xu, G.-C. Zhang, Z.-Y. Liu, F. Wang, C.-F. Zhu, T.-T. Liu, L. Dong, J.-M. Zhu, S.-Q. Weng, Y. Li, X.-Z. Shen, *ACS Appl. Mater. Interfaces* **2022**, *14*, 37356.
[290] G. Chen, X. Wang, Z. He, X. Li, Z. Yang, Y. Zhang, Y. Li, L. Zheng, Y. Miao, D. Zhang, *Molecules* **2023**, *28*, 4397.
[291] A. Ribas, J. D. Wolchok, *Science* **2018**, *359*, 1350.
[292] C. H. June, R. S. O'Connor, O. U. Kawalekar, S. Ghassemi, M. C. Milone, *Science* **2018**, *359*, 1361.
[293] M. J. Lin, J. Svensson-Arvelund, G. S. Lubitz, A. Marabelle, I. Melero, B. D. Brown, J. D. Brody, *Nat. Cancer* **2022**, *3*, 911.
[294] L. Zheng, Y. Fan, X. Wang, Z. Yang, Y. Zhang, T. Liu, M. Chen, S. Kang, S. Guo, Z. Shi, Y. Wang, K. Zheng, S. Cai, B. Dai, S. Zhuang, Y. Li, D. Zhang, *Adv. Funct. Mater.* **2023**, *33*, 2200811.
[295] J.-Y. Zhou, Q.-H. Shen, X.-J. Hong, W.-Y. Zhang, Q. Su, W.-G. Li, B. Cheng, C.-P. Tan, T. Wu, *Chem. Eng. J.* **2023**, *474*, 145516.
[296] N. J. Farrer, L. Salassa, P. J. Sadler, *Dalton Trans.* **2009**, 10690.
[297] S. Bonnet, *J. Am. Chem. Soc.* **2023**, *145*, 23397.
[298] a) T. N. Singh, C. Turro, *Inorg. Chem.* **2004**, *43*, 7260; b) B. S. Howerton, D. K. Heidary, E. C. Glazer, *J. Am. Chem. Soc.* **2012**, *134*, 8324.
[299] B. A. Albani, B. Peña, N. A. Leed, N. A. B. G. de Paula, C. Pavani, M. S. Baptista, K. R. Dunbar, C. Turro, *J. Am. Chem. Soc.* **2014**, *136*, 17095.
[300] L. Zhang, P. Wang, X.-Q. Zhou, L. Bretin, X. Zeng, Y. Husiev, E. A. Polanco, G. Zhao, L. S. Wijaya, T. Biver, S. E. Le Dévédec, W. Sun, S. Bonnet, *J. Am. Chem. Soc.* **2023**, *145*, 14963.
[301] W. Sun, S. Li, B. Häupler, J. Liu, S. Jin, W. Steffen, U. S. Schubert, H.-J. Butt, X.-J. Liang, S. Wu, *Adv. Mater.* **2017**, *29*, 1603702.
[302] X. Zeng, Y. Wang, J. Han, W. Sun, H.-J. Butt, X.-J. Liang, S. Wu, *Adv. Mater.* **2020**, *32*, 2004766.
[303] B. Zhang, Z. Xu, W. Zhou, Z. Liu, J. Zhao, S. Gou, *Chem. Sci.* **2021**, *12*, 11810.
[304] M. Yang, H. Zhao, Z. Zhang, Q. Yuan, Q. Feng, X. Duan, S. Wang, Y. Tang, *Chem. Sci.* **2021**, *12*, 11515.
[305] J. D. Knoll, B. A. Albani, C. B. Durr, C. Turro, *J. Phys. Chem. A* **2014**, *118*, 10603.
[306] V. H. S. van Rixel, V. Ramu, A. B. Auyeung, N. Beztsinna, D. Y. Leger, L. N. Lameijer, S. T. Hilt, S. E. Le Dévédec, T. Yildiz, T. Betancourt, M. B. Gildner, T. W. Hudnall, V. Sol, B. Liagre, A. Kornienko, S. Bonnet, *J. Am. Chem. Soc.* **2019**, *141*, 18444.
[307] L. N. Lameijer, D. Ernst, S. L. Hopkins, M. S. Meijer, S. H. C. Askes, S. E. Le Dévédec, S. Bonnet, *Angew. Chem., Int. Ed.* **2017**, *56*, 11549.
[308] K. Arora, M. Herroon, M. H. Al-Afyouni, N. P. Toupin, T. N. Rohrabaugh Jr., L. M. Loftus, I. Podgorski, C. Turro, J. J. Kodanko, *J. Am. Chem. Soc.* **2018**, *140*, 14367.
[309] N. Toupin, S. J. Steinke, S. Nadella, A. Li, T. N. Rohrabaugh Jr., E. R. Samuels, C. Turro, I. F. Sevrioukova, J. J. Kodanko, *J. Am. Chem. Soc.* **2021**, *143*, 9191.
[310] W. Sun, M. Parowatkin, W. Steffen, H.-J. Butt, V. Mailänder, S. Wu, *Adv. Healthcare Mater.* **2016**, *5*, 467.
[311] G. He, M. He, R. Wang, X. Li, H. Hu, D. Wang, Z. Wang, Y. Lu, N. Xu, J. Du, J. Fan, X. Peng, W. Sun, *Angew. Chem., Int. Ed.* **2023**, *62*, e202218768.
[312] X. Zeng, Y. Wang, Y.-S. Huang, J. Han, W. Sun, H.-J. Butt, X.-J. Liang, S. Wu, *Small* **2022**, *18*, 2205461.
[313] M. He, G. He, P. Wang, S. Jiang, Z. Jiao, D. Xi, P. Miao, X. Leng, Z. Wei, Y. Li, Y. Yang, R. Wang, J. Du, J. Fan, W. Sun, X. Peng, *Adv. Sci.* **2021**, *8*, 2103334.
[314] H. Shi, C. Imberti, P. J. Sadler, *Inorg. Chem. Front.* **2019**, *6*, 1623.
[315] H. Shi, O. W. L. Carter, F. Ponte, C. Imberti, M. A. Gomez-Gonzalez, F. Cacho-Nerin, P. D. Quinn, J. E. Parker, E. Sicilia, H. Huang, P. J. Sadler, *Angew. Chem., Int. Ed.* **2024**, *63*, e202400476.
[316] D. J. Norman, A. Gambardella, A. R. Mount, A. F. Murray, M. Bradley, *Angew. Chem., Int. Ed.* **2019**, *58*, 14189.
[317] K. K.-S. Tso, K.-K. Leung, H.-W. Liu, K. K.-W. Lo, *Chem. Commun.* **2016**, *52*, 4557.
[318] a) H. Luo, B. Cao, A. S. C. Chan, R. W.-Y. Sun, T. Zou, *Angew. Chem., Int. Ed.* **2020**, *59*, 11046; b) J. Jiang, B. Cao, Y. Chen, H. Luo, J. Xue, X. Xiong, T. Zou, *Angew. Chem., Int. Ed.* **2022**, *61*, e202201103.
[319] S. Kuang, F. Wei, J. Karges, L. Ke, K. Xiong, X. Liao, G. Gasser, L. Ji, H. Chao, *J. Am. Chem. Soc.* **2022**, *144*, 4091.
[320] Y. Luo, B. Cao, M. Zhong, M. Liu, X. Xiong, T. Zou, *Angew. Chem., Int. Ed.* **2022**, *61*, e202212689.
[321] X. Li, J. F. Lovell, J. Yoon, X. Chen, *Nat. Rev. Clin. Oncol.* **2020**, *17*, 657.
[322] H. S. Jung, P. Verwilst, A. Sharma, J. Shin, J. L. Sessler, J. S. Kim, *Chem. Soc. Rev.* **2018**, *47*, 2280.
[323] B. Liu, J. Jiao, W. Xu, M. Zhang, P. Cui, Z. Guo, Y. Deng, H. Chen, W. Sun, *Adv. Mater.* **2021**, *33*, 2100795.
[324] M. Li, Y. Xu, M. Zhao, F. Li, W. Feng, T. Feng, S. Liu, Q. Zhao, *Inorg. Chem.* **2020**, *59*, 17826.
[325] Y. Xu, M. Zhao, Y. Zhou, J. Wang, M. Li, F. Li, W. Lv, S. Liu, Q. Zhao, *Small Struct.* **2021**, *2*, 2100094.
[326] J. Zhao, K. Yan, G. Xu, X. Liu, Q. Zhao, C. Xu, S. Gou, *Adv. Funct. Mater.* **2021**, *31*, 2008325.
[327] Z. Wang, C. Li, S. Huang, X. Ma, Y. Sun, J. Zhao, S. Gou, *Mater. Today Nano* **2022**, *18*, 100220.
[328] Y. Deng, X. Wang, Y. Liu, Y. Xu, J. Zhang, F. Huang, B. Li, Y. Miao, Y. Sun, Y. Li, *Acta Biomater.* **2021**, *119*, 323.
[329] Y. Liu, P. Bhattarai, Z. Dai, X. Chen, *Chem. Soc. Rev.* **2019**, *48*, 2053.
[330] D.-Y. Zhang, Y. Zheng, C.-P. Tan, J.-H. Sun, W. Zhang, L.-N. Ji, Z.-W. Mao, *ACS Appl. Mater. Interfaces* **2017**, *9*, 6761.
[331] P. Zhang, H. Huang, J. Huang, H. Chen, J. Wang, K. Qiu, D. Zhao, L. Ji, H. Chao, *ACS Appl. Mater. Interfaces* **2015**, *7*, 23278.
[332] J.-H. Liang, Y. Zheng, X.-W. Wu, C.-P. Tan, L.-N. Ji, Z.-W. Mao, *Adv. Sci.* **2020**, *7*, 1901992.
[333] M.-F. Wang, R. Yang, S.-J. Tang, Y.-A. Deng, G.-K. Li, D. Zhang, D. Chen, X. Ren, F. Gao, *Angew. Chem., Int. Ed.* **2022**, *61*, e202208721.

[334] S.-J. Tang, Q.-F. Li, M.-F. Wang, R. Yang, L.-Z. Zeng, X.-L. Li, R.-D. Wang, H. Zhang, X. Ren, D. Zhang, F. Gao, *Adv. Healthcare Mater.* **2023**, *12*, 2301227.
[335] X.-L. Li, M.-F. Wang, L.-Z. Zeng, G.-K. Li, R.-Y. Zhao, F.-D. Liu, Y. Li, Y.-F. Yan, Q. Liu, Z. Li, H. Zhang, X. Ren, F. Gao, *Angew. Chem., Int. Ed.* **2024**, *63*, e202402028.
[336] C. E. Dunbar, K. A. High, J. K. Joung, D. B. Kohn, K. Ozawa, M. Sadelain, *Science* **2018**, *359*, eaan4672.
[337] J. A. Doudna, E. Charpentier, *Science* **2014**, *346*, 1258096.
[338] W. Fan, B. Yung, P. Huang, X. Chen, *Chem. Rev.* **2017**, *117*, 13566.
[339] K. Xiong, F. Wei, Y. Chen, L. Ji, H. Chao, *Small Methods* **2023**, *7*, 2201403.
[340] T. Kench, A. Rahardjo, G. G. Terrones, A. Bellamkonda, T. E. Maher, M. Storch, H. J. Kulik, R. Vilar, *Angew. Chem., Int. Ed.* **2024**, *63*, e202401808.

Lawrence Cho-Cheung Lee obtained his B.Sc. and Ph.D. degrees at City University of Hong Kong in 2014 and 2020, respectively. He is currently working as a Postdoctoral Fellow under the supervision of Prof. Kenneth Lo. His research interests focus on the design of photofunctional transition metal complexes as biological reagents for bioconjugation, bioimaging, and (photo)therapeutic applications.

Kenneth Kam-Wing Lo obtained his B.Sc. and Ph.D. degrees at The University of Hong Kong in 1993 and 1997, respectively. He then worked as a Croucher Foundation Postdoctoral Research Fellow in the Inorganic Chemistry Laboratory of the University of Oxford. In 1999, he joined the Department of Biology and Chemistry (currently Department of Chemistry) of City University of Hong Kong as an Assistant Professor and has been a Chair Professor since 2023. His research interest is the utilization of luminescent inorganic and organometallic transition metal complexes as biomolecular probes, cellular imaging reagents, and photocytotoxic agents.

